

## ELemental abundances of Planets and brown dwarfs Imaged around Stars (ELPIS):

### II. The Jupiter-like Inhomogeneous Atmosphere of the First Directly Imaged Planetary-Mass Companion 2MASS 1207 b

ZHOUIJIAN ZHANG (张周健) <sup>1,2,\*</sup>, PAUL MOLLIERE <sup>3</sup>, JONATHAN J. FORTNEY <sup>1</sup> AND MARK S. MARLEY <sup>4</sup>

<sup>1</sup>*Department of Astronomy & Astrophysics, University of California, Santa Cruz, CA 95064, USA*

<sup>2</sup>*Department of Physics & Astronomy, University of Rochester, Rochester, NY 14627, USA*

<sup>3</sup>*Max-Planck-Institut für Astronomie, Königstuhl 17, 69117 Heidelberg, Germany*

<sup>4</sup>*Lunar & Planetary Laboratory, University of Arizona, Tucson, AZ 85721, USA*

Submitted to AJ (Accepted: May 31, 2025)

#### ABSTRACT

2MASS 1207 b, the first directly imaged planetary-mass companion, has been instrumental in advancing our understanding of exoplanets and brown dwarfs over the past 20 years. We have performed extensive atmospheric retrieval analyses of 2MASS 1207 b’s JWST/NIRSpec spectrum using `petitRADTRANS` and a new atmospheric inhomogeneity framework, which characterizes homogeneous atmospheres, patchy clouds, cloud-free hot spots, or the combination of patchy clouds and spots. Among 24 retrieval runs with various assumptions, the most statistically preferred model corresponds to the patchy cloud scheme, with  $T_{\text{eff}} = 1174^{+4}_{-3}$  K,  $\log(g) = 3.62^{+0.03}_{-0.02}$  dex, and  $R = 1.399^{+0.008}_{-0.010} R_{\text{Jup}}$ , along with near-solar atmospheric compositions of  $[M/H] = -0.05 \pm 0.03$  dex and  $C/O = 0.440 \pm 0.012$ . This model suggests  $\sim 9\%$  of 2MASS 1207 b’s atmosphere is covered by thin iron and silicate clouds, producing L-dwarf-like spectra, while the remaining 91% consists of thick iron and silicate clouds, emitting blackbody-like spectra. These thin-cloud patches and thick-cloud regions resemble Jupiter’s belts and zones, respectively, and this scenario is consistently supported by other retrieval runs incorporating inhomogeneous atmospheres. We demonstrate that the weak CO absorption of 2MASS 1207 b can be explained by the veiling effects of patchy thick clouds; the absence of  $3.3 \mu\text{m}$   $\text{CH}_4$  absorption is attributed to its hot thermal structure, which naturally leads to a CO-dominant,  $\text{CH}_4$ -deficient atmosphere. The retrieved atmospheric models also match the observed variability amplitudes of 2MASS 1207 b. Our analysis reveals that the inferred atmospheric properties show significant scatter in less statistically preferred retrieval runs but converge to consistent values among the preferred ones. This underscores the importance of exploring diverse assumptions in retrievals to avoid biased interpretations of atmospheric properties and formation pathways.

#### 1. INTRODUCTION

We are entering a new era in the atmospheric studies of exoplanets and brown dwarfs, marked by a rapidly growing number of spectroscopic analyses driven by unprecedented observational capabilities and continuous advancements in atmospheric modeling. For directly imaged exoplanets and brown dwarfs, thermal emission spectroscopy provides crucial insights into their atmospheric thermal structures, elemental abundances, surface gravities, radii, kinematics, spin rates, formation epoch, and atmospheric processes, such as cloud formation, vertical mixing, and planetesimal accretion (e.g., Chauvin et al. 2004; Marois et al. 2008, 2010; Currie et al. 2011; Macintosh et al. 2015; Mollière et al. 2020;

Wang et al. 2020; Zhang et al. 2021a; Wang et al. 2021, 2022; Ward-Duong et al. 2021; Xuan et al. 2022; Hinkley et al. 2023; Miles et al. 2023; Balmer et al. 2024; de Regt et al. 2024; González Picos et al. 2024; Hsu et al. 2024a; Inglis et al. 2024; Kothari et al. 2024; Landman et al. 2024; Mukherjee et al. 2024; Nasedkin et al. 2024b; Palma-Bifani et al. 2024; Petrus et al. 2024; Zhang et al. 2023, 2025). In particular, measurements of these objects’ atmospheric compositions — including metallicity ( $[M/H]$ ), carbon-to-oxygen ratio ( $C/O$ ), and isotopologue ratios — offer invaluable opportunities to compare these properties with those observed in the solar system and irradiated exoplanets (e.g., Thorngren & Fortney 2019; Welbanks et al. 2019; Zhang et al. 2021a; Barrado et al. 2023; Gandhi et al. 2023; Hoch et al. 2023; Xuan et al. 2024; Rowland et al. 2024; Teske 2024). Such

\* NASA Sagan Fellow

comparisons enable population-level investigations into the origins and evolution of self-luminous worlds.

Traditionally, the spectroscopic characterization of self-luminous exoplanets and brown dwarfs has relied on forward model grids, which have been foundational to the field (see reviews by Allard et al. 1997; Burrows et al. 2001; Marley & Robinson 2015; Fortney 2018; Zhang 2020; Currie et al. 2023). These pre-computed models use a limited number of free parameters to predict emergent spectra and thermal evolution properties under a set of assumptions, such as one-dimensional radiative-convective equilibrium, chemical (dis)equilibrium, and the presence and composition of clouds. By comparing observed spectrophotometry with synthetic atmospheric model spectra, these models provide self-consistent constraints on atmospheric properties. However, systematic offsets between observations and model predictions often arise, revealing the limitations of certain assumptions and motivating the development of next-generation forward models (e.g., Zhang et al. 2021c,d; Hurt et al. 2024; Petrus et al. 2024).

Over the past decade, the atmospheric retrieval technique has emerged as a major alternative for characterizing exoplanet and brown dwarf atmospheres (e.g., Madhusudhan & Seager 2009; Lee et al. 2012, 2013; Line et al. 2013, 2015; Mollière et al. 2019; MacDonald & Batalha 2023). Unlike forward model grids, retrievals offer greater flexibility by treating atmospheric processes as free parameters rather than fixed assumptions, enabling constraints on a broader range of fundamental properties through a data-driven approach with significantly reduced data-model offsets. To date, retrievals have been applied to the near-infrared spectra of over ten directly imaged exoplanets (e.g., GRAVITY Collaboration et al. 2020; Brown-Sevilla et al. 2023; Mollière et al. 2020; Wang et al. 2020; Zhang et al. 2021a; Wang 2023; Zhang et al. 2023; Balmer et al. 2024; Inglis et al. 2024; Nasedkin et al. 2024b) and over sixty brown dwarfs (most of which are near the T/Y transition; e.g., Line et al. 2017; Zalesky et al. 2019, 2022; Gonzales et al. 2021; Xuan et al. 2022, 2024; de Regt et al. 2024; González Picos et al. 2024; Phillips et al. 2024; Hsu et al. 2024b) across various spectral resolutions. Most retrieval studies, however, assume one-dimensional, homogeneous atmospheres — a simplification that may be inadequate for some planetary-mass objects and brown dwarfs with detected atmospheric variabilities (e.g., Artigau et al. 2009; Radigan et al. 2014; Apai et al. 2017; Vos et al. 2022; Zhou et al. 2022; Biller et al. 2024; McCarthy et al. 2024). Such variability suggests top-of-atmosphere inhomogeneities, potentially caused by patchy clouds (e.g., Ackerman & Marley 2001; Burgasser et al. 2002; Marley et al. 2010; Apai et al. 2013) and hot spots (e.g., Robinson & Marley 2014; Zhang & Showman 2014; Showman

et al. 2019; Tan & Showman 2021), underscoring the need for more sophisticated atmospheric models.

Significant progress in retrieving inhomogeneous atmospheres has been demonstrated by Vos et al. (2023), who analyzed the 1–15  $\mu\text{m}$  spectra of two highly variable early-T brown dwarfs. To account for patchy clouds, Vos et al. (2023) employed a model combining two one-dimensional atmospheric columns with identical temperature-pressure (T-P) profiles but differing cloud properties. Their analysis suggested the presence of patchy forsterite clouds, which appear to be consistent with some of the observed photometric variability amplitudes of these brown dwarfs. This approach of combining two atmospheric columns has also been utilized in previous spectroscopic studies of variable brown dwarfs using self-consistent forward model grids (e.g., Marley et al. 2010; Morley et al. 2014; Lew et al. 2016).

Here, we present a new generalized retrieval framework for characterizing inhomogeneous atmospheres of self-luminous exoplanets and brown dwarfs influenced by patchy clouds, hot spots, or a combination of both. We apply this framework to the JWST/NIRSpec spectrum of 2MASS J12073346–3932539 b (a.k.a. 2MASS 1207 b or TWA 27B; Chauvin et al. 2004), the first directly imaged planetary-mass companion, discovered 20 years ago. Orbiting a young M8 brown dwarf 2MASS 1207 A, 2MASS 1207 b has an L6 spectral type (Manjavacas et al. 2024) with a variable atmosphere (Zhou et al. 2016) and has been instrumental in advancing our understanding of self-luminous exoplanet and brown dwarf atmospheres.

The primary goal of this work is to characterize the potential inhomogeneous atmosphere of 2MASS 1207 b in the context of its detected photometric variabilities and to determine its atmospheric compositions as part of the Planets and brown dwarfs Imaged around Stars (ELPIS) program (Zhang et al. 2023). We begin by reviewing the known properties of the 2MASS 1207 A+b system (Section 2), followed by a description of the archival JWST/NIRSpec spectrum of the target 2MASS 1207 b (Section 3). We use thermal evolution models to contextualize the atmospheric properties of 2MASS 1207 b (Section 4), and then perform retrieval analyses to explore various atmospheric scenarios: homogeneous atmospheres, patchy clouds, cloud-free hot spots, and a combination of patchy clouds and hot spots (Sections 5 and 6). Our analysis suggests that 2MASS 1207 b has near-solar atmospheric [M/H] and C/O ratios, along with a Jupiter-like, inhomogeneous atmosphere, with thin-cloud patches covering 9% of its atmosphere and thick-cloud regions covering 91%. We discuss the implications of these results in Section 7 and provide a summary in Section 8.

## 2. A BRIEF REVIEW OF 2MASS 1207 A+b

In celebration of the 20th anniversary of the discovery of 2MASS 1207 A+b, we review the known properties of this remarkable system.

### 2.1. 2MASS 1207 A

2MASS 1207 A (M8) was first identified as a candidate member of the TW Hya association (TWA,  $10 \pm 2$  Myr; Luhman 2023) by Gizis (2002). The TWA membership of this object is supported by its youth, as suggested by the strong Balmer-series emission (e.g., Gizis 2002; Gizis & Bharat 2004; Mohanty et al. 2003, 2005; Scholz et al. 2005; Barado Y Navascués 2006), He I emission ( $\lambda\lambda 4471, \lambda\lambda 5876, \lambda\lambda 6678, \lambda\lambda 7065$ ; e.g., Gizis 2002; Mohanty et al. 2003, 2005), Li I  $\lambda\lambda 6708$  absorption (e.g., Mohanty et al. 2003; Scholz et al. 2005), weak alkali and FeH absorption (e.g., Mohanty et al. 2003; Looper et al. 2007; Allers & Liu 2013), strong VO absorption (e.g., Looper et al. 2007; Allers & Liu 2013), and a triangular-shaped  $H$ -band spectrum (e.g., Looper et al. 2007). The parallax, proper motion, and radial velocity measurements have since placed 2MASS 1207 A as a confirmed kinematic member of TWA (e.g., Mamajek 2005; Gizis et al. 2007; Biller & Close 2007; Ducourant et al. 2008; Malo et al. 2013; Donaldson et al. 2016).

The ongoing accretion of 2MASS 1207 A was suggested by multiple follow-up observations since its discovery. Its UV spectra resemble those of classical T Tauri stars, exhibiting numerous  $H_2$  fluorescence lines and ion emission lines (e.g., Gizis et al. 2005; France et al. 2010). Optical emission lines of Balmer series, He I, Ca II H and K, Ca II infrared triplet, and O I have been consistently detected (e.g., Gizis 2002; Mohanty et al. 2003, 2005; Scholz et al. 2005; Scholz & Jayawardhana 2006; Stelzer et al. 2007; Herczeg et al. 2009; Venuti et al. 2019). The strongly variable shape and strength of  $H\alpha$  suggest that the accretion rate of 2MASS 1207 A varies by more than one order of magnitude over months to years (e.g., Mohanty et al. 2005; Scholz et al. 2005; Scholz & Jayawardhana 2006; Stelzer et al. 2007; though see Herczeg et al. 2009). No strong emission has been detected in the near-infrared wavelengths to date (e.g., Venuti et al. 2019; Manjavacas et al. 2024). The emission lines of 2MASS 1207 A likely result from its accretion and star-disk interactions, rather than potential chromospheric activities, especially given the absence of its X-ray (Gizis & Bharat 2004) and radio (Osten & Jayawardhana 2006) emission. Additionally, Reiners et al. (2009) placed a  $3\sigma$  upper limit of 1 kilogauss (with a maximum-likelihood value of 0) for the magnetic field of 2MASS 1207 A; this constraint is consistent with the weak magnetic field strength required to drive the observed accretion of this brown dwarf (Stelzer et al. 2007).

Our understanding of 2MASS 1207 A's circumstellar disk has greatly benefited from infrared and submillimeter obser-

vations. The infrared excess of this brown dwarf was only mildly detected in  $L'$  band ( $3.8 \mu\text{m}$ ) and Spitzer/IRAC [3.6] band (Jayawardhana et al. 2003; Riaz et al. 2006), significantly detected at longer wavelengths up to  $\sim 70 \mu\text{m}$  (Sterzik et al. 2004; Riaz et al. 2006; Riaz & Gizis 2008; Harvey et al. 2012; Manjavacas et al. 2024), and not detected at  $160 \mu\text{m}$ ,  $250 \mu\text{m}$ ,  $350 \mu\text{m}$ ,  $500 \mu\text{m}$ , and  $850 \mu\text{m}$  (based on Spitzer, Herschel, and JCMT; Harvey et al. 2012; Riaz et al. 2012a,b; Riaz & Gizis 2012; Mohanty et al. 2013). The JWST/NIRSpec spectroscopy of this object also revealed the infrared excess at wavelengths beyond  $2.5 \mu\text{m}$  (Manjavacas et al. 2024). Dust continuum emission at  $0.89 \text{ mm}$  and the CO emission from 2MASS 1207 A's disk were observed by ALMA (Ricci et al. 2017).

Previous modeling efforts of 2MASS 1207 A's spectrophotometry suggested that its circumstellar disk does not have an inner hole (e.g., Morrow et al. 2008) and has an outer radius of  $\sim 10\text{--}50 \text{ au}$  (e.g., Riaz & Gizis 2012; Ricci et al. 2017); this compact disk was likely tidally truncated by its planetary-mass companion, 2MASS 1207 b (e.g., Riaz & Gizis 2012; Mohanty et al. 2013; Ricci et al. 2017). The disk inclination might be as high as  $55^\circ\text{--}75^\circ$  (e.g., Sterzik et al. 2004; Riaz & Gizis 2007, 2012; Skemer et al. 2011), which aligns with A's variable accretion emission lines (e.g., Scholz et al. 2005; Scholz & Jayawardhana 2006) and the spectroastrometry of the observed bipolar and collimated outflows (e.g., Mohanty et al. 2005; Whelan et al. 2007, 2012). A slightly lower disk inclination ( $35^{+20}_{-15}^\circ$ ) was derived by Ricci et al. (2017) based on ALMA observations, but as noted by these authors, such a low disk inclination would lead to an excessively high dynamical mass measurement for 2MASS 1207 A. The dust grains inside the disk may have grown to sizes larger than a few micrometers (Sterzik et al. 2004; Morrow et al. 2008; Riaz & Gizis 2008). The estimated dust reservoir surrounding 2MASS 1207 A's is  $\sim 0.1 M_\oplus$  (e.g., Mohanty et al. 2013; Ricci et al. 2017).

### 2.2. 2MASS 1207 b

The planetary-mass companion, 2MASS 1207 b (L6), was first discovered by Chauvin et al. (2004) through high-contrast adaptive optics imaging, with its physical association to 2MASS 1207 A confirmed by Chauvin et al. (2005) and Song et al. (2006). Based on evolution models and 2MASS 1207 b's near-infrared absolute magnitudes, Chauvin et al. (2004) and Chauvin et al. (2005) estimated that this object has an effective temperature of  $T_{\text{eff}} = 1200 \pm 200 \text{ K}$ , a mass of  $M = 5 \pm 2 M_{\text{Jup}}$ , a bolometric luminosity of  $\log(L/L_\odot) \approx -4.28 \text{ dex}$ , and a radius of  $R \approx 1.5 R_{\text{Jup}}$ . As the first directly imaged planetary-mass companion, 2MASS 1207 b has received numerous follow-up observations focusing on its thermal emission spectrophotometry (e.g., Chauvin et al. 2004; Song et al. 2006; Mohanty

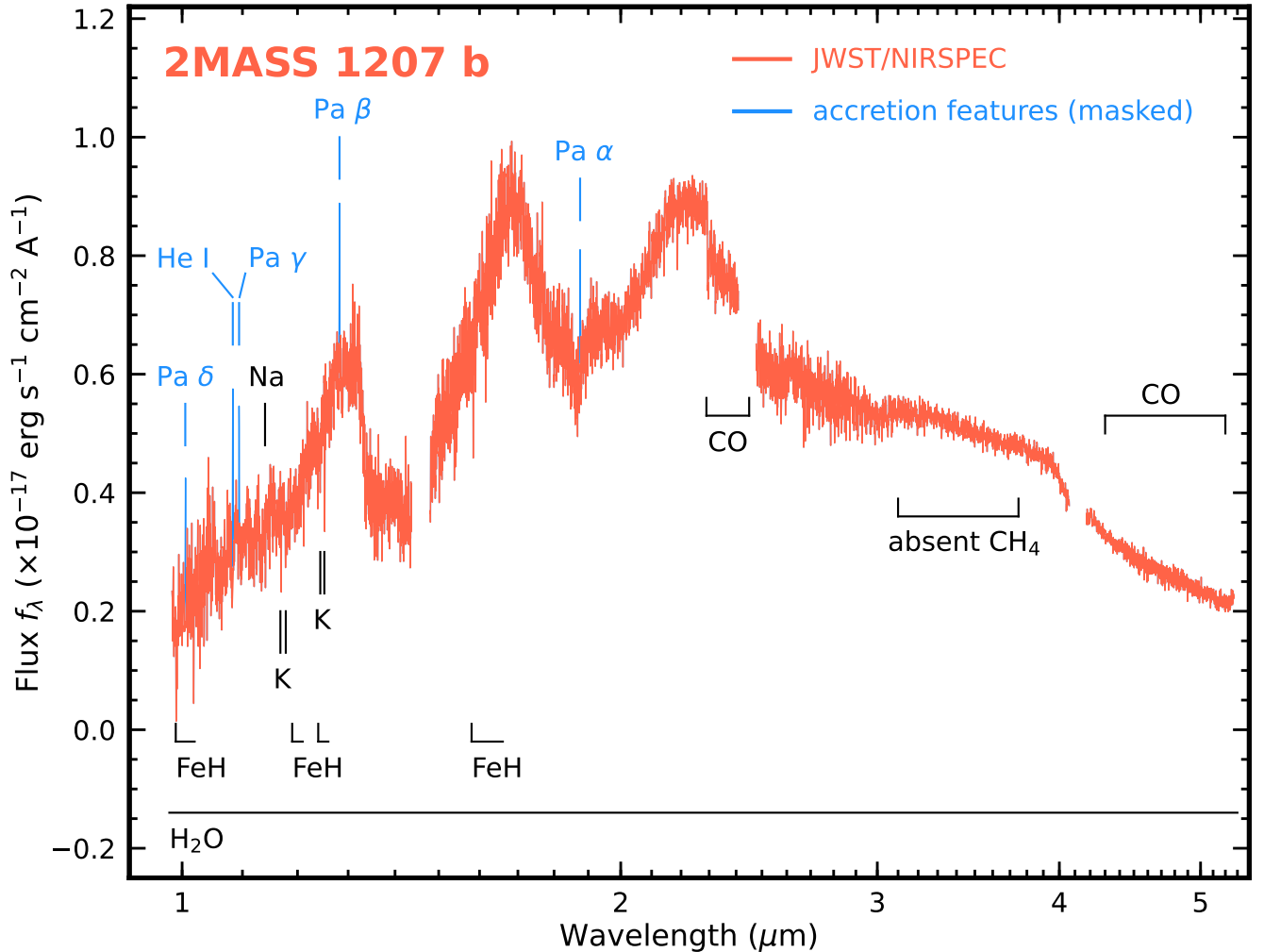


**Figure 1.** The archival JWST/NIRSpec spectrum (red) of 2MASS 1207 b, with the x-axis shown in log scale. Key atomic and molecular features are labeled. Several prominent accretion emission lines, identified by [Luhman et al. \(2023\)](#) and with detection significance values above  $3.5\sigma$  ([Marleau et al. 2024](#)), are highlighted in blue and are masked in our subsequent retrieval analysis.

et al. 2007; Patience et al. 2010; Skemer et al. 2011, 2014; Zhou et al. 2016, 2019; Luhman et al. 2023; Manjavacas et al. 2024).

Spectroscopic studies of 2MASS 1207 b have profoundly advanced our understanding of the atmospheres of young exoplanets and brown dwarfs over the past two decades. Pioneering characterization efforts for 2MASS 1207 b encountered discrepancies among this companion’s age, bolometric luminosity, and effective temperature. By comparing this object’s near-infrared spectra with the available atmospheric models at the time, [Mohanty et al. \(2007\)](#) inferred an effective temperature of  $T_{\text{eff}} \approx 1600$  K (also see [Patience et al. 2012](#)). However, based on thermal evolution models and the system’s young age, this high  $T_{\text{eff}}$  implied a bolometric luminosity  $10\times$  brighter than what was measured from photometry ([Mamajek 2005](#)). To explain the measured underluminosity, [Mohanty et al. \(2007\)](#) thoroughly examined

several scenarios and suggested a testable hypothesis that 2MASS 1207 b could be occulted by its potential gray edge-on disk. Around the same time, [Mamajek & Meyer \(2007\)](#) proposed a novel alternative hypothesis that the companion might be an afterglow of a recent collision between two protoplanets and have a small radius and a hot temperature.

Breakthroughs of the underluminosity problem for 2MASS 1207 b were achieved by [Skemer et al. \(2011\)](#) and [Barman et al. \(2011a\)](#), as sparked by the characterization of other newly discovered exoplanets and brown dwarfs at the time, such as HR 8799 bcde, HN Peg B, and HD 203030 B (e.g., [Metchev & Hillenbrand 2006](#); [Luhman et al. 2007](#); [Marois et al. 2008, 2010](#); [Bowler et al. 2010](#); [Barman et al. 2011b](#); [Currie et al. 2011](#); [Madhusudhan et al. 2011](#)). By modeling the spectral energy distribution (SED) of 2MASS 1207 b, [Skemer et al. \(2011\)](#) concluded that this companion is likely not influenced by an edge-on

disk or an outer spherical dust shell. Instead, introducing thick clouds with disequilibrium chemistry processes into atmospheric models would lower the effective temperature to  $T_{\text{eff}} \approx 1000$  K (e.g., Barman et al. 2011a; Skemer et al. 2011, 2014), resolving the underluminosity problem. Clouds and disequilibrium chemistry are now known as key processes in the atmospheres of exoplanets and brown dwarfs.

Inhomogeneities in the atmosphere of 2MASS1207b were indicated by time-series spectroscopic monitoring. Over an 8.7 hour baseline, Zhou et al. (2016) detected variability amplitudes of  $1.36\% \pm 0.23\%$  and  $0.78\% \pm 0.22\%$  at wavelengths near  $1.25 \mu\text{m}$  and  $1.54 \mu\text{m}$ , respectively, with a period of  $10.7^{+1.2}_{-0.6}$  hr.

Accretion emission lines, such as He I and Paschen series, were recently revealed in 2MASS 1207 b’s JWST/NIRSpec spectrum (Luhman et al. 2023; Manjavacas et al. 2024; Marleau et al. 2024). The strengths of these lines suggest a mass accretion rate of several  $\times 10^{-9} M_{\text{Jup}} \text{yr}^{-1}$ , with an estimated uncertainty of about an order of magnitude (Marleau et al. 2024; Aoyama et al. 2024). These emission lines are suggested to originate from magnetospheric accretion rather than from active accretion through a potential circumplanetary disk (Marleau et al. 2024; Aoyama et al. 2024). The presence of such a disk remains unconfirmed at the time of writing. Indeed, the W2 photometry ( $4.6 \mu\text{m}$ ) of 2MASS 1207 b does not show strong excess, suggesting that the disk emission, if any, contributes to its SED beyond  $5 \mu\text{m}$  (Luhman et al. 2023). The mass of 2MASS 1207 b’s dust disk is likely below  $1 M_{\text{moon}}$  based on ALMA observations (Ricci et al. 2017).

### 2.3. The 2MASS 1207 A+b Ecosystem

The mass ratio between 2MASS 1207 b and 2MASS 1207 A ( $M_b/M_A \approx 0.2$ ; e.g., Chauvin et al. 2005) suggests that this system is more analogous to stellar binaries than to typical planetary systems discovered by transits or radial velocity methods (see also Figure 1 of Zhang et al. 2025). Any additional companions with masses  $> 2 M_{\text{Jup}}$  and orbital separation  $> 75$  au were ruled out by Zhou et al. (2019). For 2MASS 1207 b to have formed via disk instability, an unusually high initial disk mass for 2MASS 1207 A would be required (e.g., Gizis et al. 2005). Furthermore, the core accretion mechanism would likely be inefficient in assembling 2MASS 1207 b’s mass at its current orbit ( $\approx 50$  au) within its young age (e.g., Lodato et al. 2005). However, outward migration could alleviate some of the tension regarding the formation timescale (e.g., Martin et al. 2007). Consequently, it is widely theorized that 2MASS 1207 A+b formed via gravitational instability during the collapse of a molecular cloud (e.g., Lodato et al. 2005; Gizis et al. 2005; Chauvin et al. 2005; Boss 2006; Stamatellos & Whitworth 2009). This scenario is further supported by the fact that the

mass of 2MASS 1207 b is close to the estimated lowest mass threshold for star formation products (e.g., Zuckerman & Song 2009; Kirkpatrick et al. 2021; Miret-Roig et al. 2022; Pearson & McCaughrean 2023; Bouy et al. 2025).

The wide separation and relatively low total mass of the 2MASS 1207 A+b system suggest that it may not be stable over the long term (e.g., Mugrauer & Neuhauser 2005; Burgasser & McElwain 2006). Existing relative astrometry data of A and b only cover 0.06% of the system’s full orbit (given their long orbital period of  $\approx 1800$  yr; Blunt et al. 2017), implying that the dynamical mass of 2MASS 1207 b will remain uncertain for the foreseeable future.

## 3. ARCHIVAL JWST/NIRSPEC SPECTROSCOPY OF 2MASS 1207 b

We collected archival JWST/NIRSpec spectra of 2MASS 1207 b from Luhman et al. (2023) and Manjavacas et al. (2024), which cover  $0.98\text{--}5.26 \mu\text{m}$  with moderate spectral resolution ( $R \sim 2700$ ; Figure 1). These data were taken using the G140H/F100LP, G235H/F170LP, and G395H/F290LP gratings, yielding an average signal-to-noise ratio (S/N) of 36, 70, 130, 240, and 128 per pixel near  $1.3 \mu\text{m}$ ,  $1.7 \mu\text{m}$ ,  $2.2 \mu\text{m}$ ,  $3.7 \mu\text{m}$ , and  $4.6 \mu\text{m}$ , respectively.

For the subsequent retrieval analysis, we masked a few accretion emission lines with detection significance values exceeding  $3.5\sigma$  (Figure 1), as identified by Marleau et al. (2024). This includes Pa  $\alpha$  ( $1.874\text{--}1.8765 \mu\text{m}$ ), Pa  $\beta$  ( $1.2812\text{--}1.2836 \mu\text{m}$ ), Pa  $\gamma$  ( $1.0935\text{--}1.0948 \mu\text{m}$ ), Pa  $\delta$  ( $1.004\text{--}1.0058 \mu\text{m}$ ), and the He I triplet ( $1.0824\text{--}1.0842 \mu\text{m}$ ). Additionally, 2MASS 1207 b does not exhibit excess emission in the W2 band ( $4.6 \mu\text{m}$ ), suggesting that its potential circumstellar disk does not significantly contribute to the JWST/NIRSpec spectroscopy (e.g., Luhman et al. 2023; see also Section 2.2).

## 4. CONTEXTUALIZING THE PROPERTIES OF 2MASS 1207 b VIA EVOLUTION MODELS

We first derive the bolometric luminosity ( $L_{\text{bol}}$ ) of 2MASS 1207 b (Section 4.1) by using its NIRSpec spectrum and a new bolometric correction approach we developed for self-luminous exoplanets, brown dwarfs, and low-mass stars (Appendix A). By combining the  $L_{\text{bol}}$  and the age of 2MASS 1207 b, we use multiple thermal evolution models to derive its fundamental physical properties (Section 4.2), including effective temperatures ( $T_{\text{eff}}$ ), radii ( $R$ ), surface gravities ( $\log(g)$ ),<sup>1</sup> and masses ( $M$ ). These evolution-based con-

<sup>1</sup> Throughout this manuscript, we use “ $\log()$ ” and “ $\ln()$ ” for 10-based and natural logarithm, respectively. Also, the surface gravity,  $g$ , is in cgs units of  $\text{cm s}^{-2}$ .

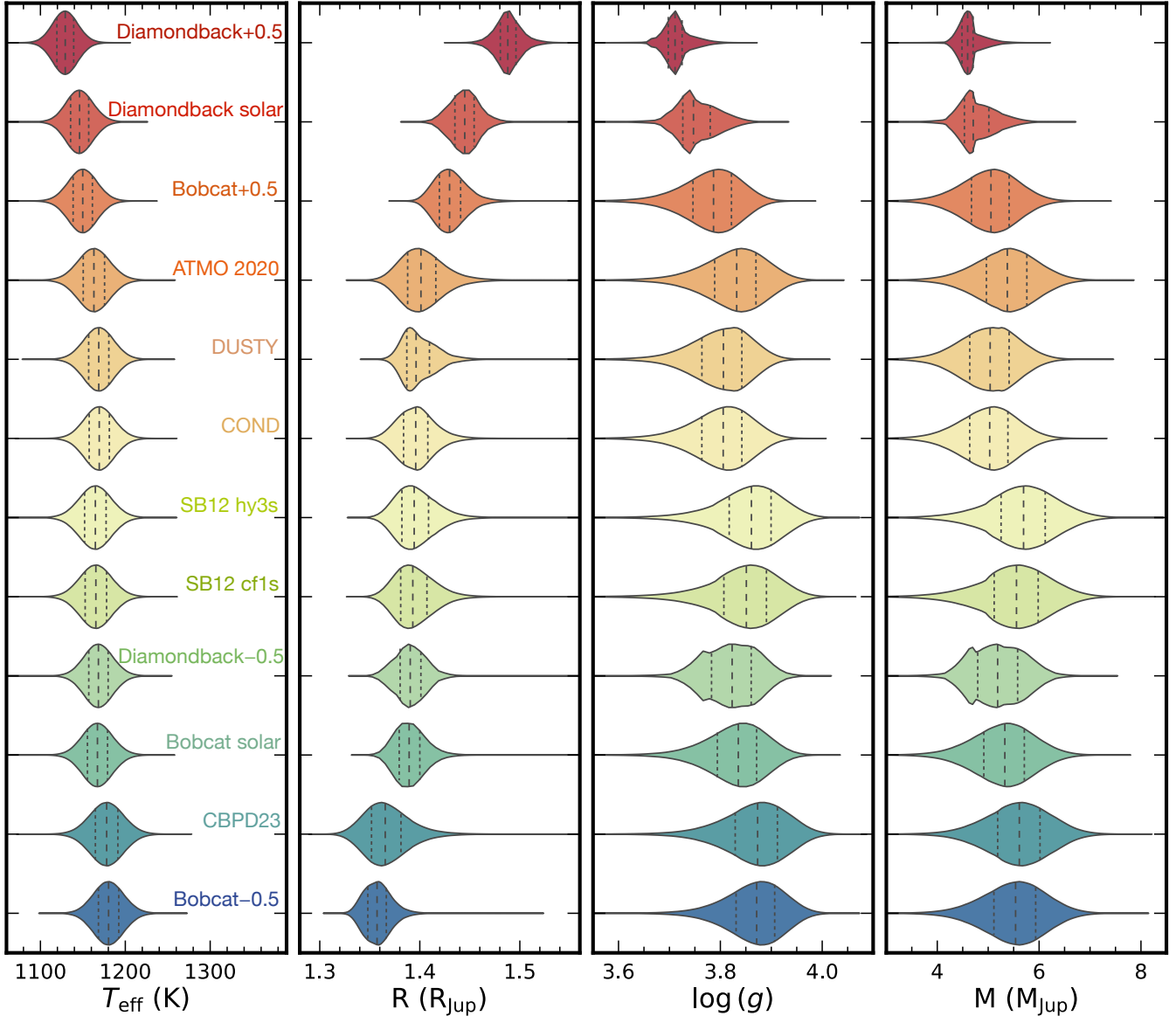


**Figure 2.** Violin plot for the physical properties of 2MASS 1207 b inferred from its bolometric luminosity, age, and various evolution models (sorted by radii). The vertical dashed line inside each violin indicates the median value of the parameter, while the dotted lines represent the first and third quartiles of the distribution. Model labels and the parameter confidence intervals are summarized in Table 1.

straints provide crucial context and physics-driven priors for our subsequent atmospheric retrieval analysis (see also Section 5.1 of Zhang et al. 2023 and references therein).

#### 4.1. Bolometric Luminosity

We derive the bolometric luminosity of 2MASS 1207 b using its JWST/NIRSpec spectrum and the bolometric correction approach designed to mitigate modeling systematics, as described in Appendix A. This method combines multiple grids of atmospheric models to estimate a spectroscopy-based bolometric correction term,  $\text{specBC}_{\lambda\lambda}$ , which converts the integrated spectral luminosity over a specific wavelength range  $\lambda\lambda$  into the bolometric luminosity.

For 2MASS 1207 b, we integrate its NIRSpec spectrum over the wavelength range  $\lambda\lambda = 1 - 5 \mu\text{m}$ . First, we estimate  $\text{specBC}_{1-5\mu\text{m}}$  for 2MASS 1207 b across a customized parameter space of  $T_{\text{eff}} = 1000 - 1400 \text{ K}$  and  $\log(g) < 5 \text{ dex}$ . By combining the bolometric correction terms from all model spectra within this parameter space, we find  $\text{specBC}_{1-5\mu\text{m}} = 0.101 \pm 0.018 \text{ dex}$  based on the Sonora Diamondback grid and  $0.112 \pm 0.025 \text{ dex}$  based on the Exo-REM grid. Other atmospheric model grids explored in Appendix A are excluded either because their assumptions do not align with the cloudy atmospheres of 2MASS 1207 b (ATMO2020) or because their parameter spaces do not en-

**Table 1.** Evolution-based properties of 2MASS 1207 b based on  $\log(L_{\text{bol}}/L_{\odot}) = -4.467 \pm 0.026$  dex and an age of  $10 \pm 2$  Myr

Label <sup>a</sup>	Evolution Model	$T_{\text{eff}}$ (K)	$R$ ( $R_{\text{Jup}}$ )	$\log g$ (dex)	$M$ ( $M_{\text{Jup}}$ )
ATMO2020	Phillips et al. (2020): cloudless and $[M/H]=0$	$1163^{+18}_{-18}$	$1.401^{+0.023}_{-0.019}$	$3.83^{+0.05}_{-0.07}$	$5.4^{+0.6}_{-0.6}$
Bobcat-0.5	Marley et al. (2021): cloudless and $[M/H]=-0.5$	$1180^{+17}_{-17}$	$1.357^{+0.014}_{-0.013}$	$3.87^{+0.05}_{-0.06}$	$5.5^{+0.6}_{-0.6}$
Bobcat solar	Marley et al. (2021): cloudless and $[M/H]=0$	$1167^{+17}_{-17}$	$1.389^{+0.016}_{-0.014}$	$3.84^{+0.05}_{-0.06}$	$5.3^{+0.6}_{-0.6}$
Bobcat+0.5	Marley et al. (2021): cloudless and $[M/H]=+0.5$	$1149^{+16}_{-16}$	$1.430^{+0.017}_{-0.015}$	$3.79^{+0.05}_{-0.06}$	$5.1^{+0.5}_{-0.6}$
CBPD23	Chabrier et al. (2023): cloudless and $[M/H]=0$	$1178^{+19}_{-19}$	$1.365^{+0.024}_{-0.020}$	$3.87^{+0.06}_{-0.07}$	$5.6^{+0.6}_{-0.6}$
COND	Baraffe et al. (2003): cloudless and $[M/H]=0$	$1169^{+17}_{-17}$	$1.396^{+0.018}_{-0.018}$	$3.81^{+0.05}_{-0.06}$	$5.0^{+0.5}_{-0.6}$
Diamondback-0.5	Morley et al. (2024): hybrid and $[M/H]=-0.5$	$1168^{+16}_{-16}$	$1.390^{+0.016}_{-0.015}$	$3.82^{+0.05}_{-0.06}$	$5.2^{+0.6}_{-0.5}$
Diamondback solar	Morley et al. (2024): hybrid and $[M/H]=0$	$1146^{+15}_{-15}$	$1.445^{+0.014}_{-0.015}$	$3.75^{+0.05}_{-0.03}$	$4.7^{+0.5}_{-0.3}$
Diamondback+0.5	Morley et al. (2024): hybrid and $[M/H]=+0.5$	$1129^{+14}_{-14}$	$1.488^{+0.012}_{-0.011}$	$3.71^{+0.03}_{-0.02}$	$4.6^{+0.2}_{-0.2}$
DUSTY	Chabrier et al. (2000): cloudy and $[M/H]=0$	$1168^{+17}_{-17}$	$1.395^{+0.020}_{-0.013}$	$3.81^{+0.05}_{-0.06}$	$5.0^{+0.5}_{-0.6}$
SB12 cf1s	Spiegel & Burrows (2012): cloudless and $[M/H]=0$	$1165^{+18}_{-18}$	$1.393^{+0.021}_{-0.017}$	$3.85^{+0.06}_{-0.07}$	$5.6^{+0.6}_{-0.7}$
SB12 hy3s	Spiegel & Burrows (2012): hybrid and $[M/H]=+0.5$	$1164^{+18}_{-18}$	$1.394^{+0.022}_{-0.018}$	$3.86^{+0.06}_{-0.07}$	$5.7^{+0.6}_{-0.7}$
<b>Adopted<sup>b</sup></b>		$1163^{+23}_{-21}$	$1.40^{+0.03}_{-0.04}$	$3.82^{+0.09}_{-0.07}$	$5.2^{+0.6}_{-0.7}$

<sup>a</sup>Labels of the evolution model shown in 2.

<sup>b</sup>The adopted parameters are determined from the concatenated chains of all these thermal evolution models (Section 4.2).

compass the properties of 2MASS 1207 b (BT-Settl and SPHINX). To ensure conservative uncertainty estimates, we adopt  $\text{specBC}_{1-5\mu\text{m}} = 0.112 \pm 0.025$  dex from Exo-REM.

Assuming 2MASS 1207 b shares the same distance as 2MASS 1207 A,  $d = 64.47 \pm 0.47$  pc (Bailer-Jones et al. 2021), we derive a bolometric luminosity of  $\log(L_{\text{bol}}/L_{\odot}) = -4.467 \pm 0.026$  dex for 2MASS 1207 b. This estimate is consistent with that reported by Luhman et al. (2023) but includes more conservative uncertainty estimates and mitigated modeling systematics.

#### 4.2. Evolution-based Physical Properties

We determine the physical properties of 2MASS 1207 b using the following hot-start thermal evolution models:

- ATMO2020 models with solar metallicity (Phillips et al. 2020).
- CBPD23 models with solar metallicity (Chabrier et al. 2023).
- COND models with solar metallicity (Baraffe et al. 2003).
- DUSTY models with solar metallicity (Chabrier et al. 2000).
- Sonora Bobcat models with  $[M/H] = -0.5, 0, +0.5$  dex (Marley et al. 2021).
- Sonora Diamondback hybrid models with  $[M/H] = -0.5, 0, +0.5$  dex (Morley et al. 2024). These

models transition from cloudy ( $f_{\text{sed}} = 2$ ) to cloudless atmospheres at  $T_{\text{eff}} = 1300$  K.

- Models from (Spiegel & Burrows 2012), including cloudless atmospheres with solar metallicity (SB12 cf1s) and cloudy atmospheres with  $3\times$  solar metallicity (SB12 hy3s).

We infer the properties of 2MASS 1207 b in a Monte Carlo fashion. We draw  $10^6$  random bolometric luminosities from a normal distribution  $\mathcal{N}(\mu = -4.467 \text{ dex}, \sigma = 0.026 \text{ dex})$ , and the same number of random ages from a normal distribution  $\mathcal{N}(\mu = 10 \text{ Myr}, \sigma = 2 \text{ Myr})$  truncated at zero (Luhman 2023). Evolution models are interpolated linearly for  $\log(g)$  and  $\log(L_{\text{bol}}/L_{\odot})$  and logarithmically for  $T_{\text{eff}}$ ,  $R$ ,  $M$ , and age.

Figures 2 and Table 1 summarize the inferred properties of 2MASS 1207 b. The consistency across different evolution models allows us to concatenate the chains of each parameter derived by all models and compute their confidence intervals. We find that 2MASS 1207 b has  $T_{\text{eff}} = 1163^{+21}_{-23}$  K,  $\log(g) = 3.82^{+0.07}_{-0.09}$  dex,  $R = 1.40^{+0.04}_{-0.03}$   $R_{\text{Jup}}$ , and  $M = 5.2^{+0.7}_{-0.6}$   $M_{\text{Jup}}$ .

The  $3\sigma$  confidence intervals across all evolution models span  $1.30\text{--}1.55$   $R_{\text{Jup}}$  in  $R$ ,  $3.54\text{--}4.02$  dex in  $\log(g)$ , and  $3.0\text{--}7.5$   $M_{\text{Jup}}$  in  $M$ . These evolution-based ranges will serve as uniform parameter priors in some of our subsequent retrieval runs (Section 5).

## 5. ATMOSPHERIC RETRIEVAL FRAMEWORK

We perform atmospheric retrievals for the JWST/NIRSpec spectrum of 2MASS 1207 b using `petitRADTRANS` (Mollière et al. 2019; Nasedkin et al. 2024a). The thermal structure, chemistry, and cloud models employed in the retrievals are described in Sections 5.1–5.3.

In Section 5.4, we introduce an “atmospheric inhomogeneity” framework, which models the potentially inhomogeneous atmospheres of exoplanets, brown dwarfs, and low-mass stars. This framework uses multiple atmospheric columns, each with distinct cloud properties and/or temperature-pressure (T-P) profiles. Unless otherwise specified, each atmospheric column adheres to the same modeling setup described in Sections 5.1–5.3.

### 5.1. Temperature Model Coupled with Radiative-Convective Equilibrium

Our temperature model builds on the parameterization of Zhang et al. (2023). The atmosphere is divided into 10 pressure layers, spaced logarithmically from  $10^3$  to  $10^{-6}$  bar (Figure 3). The thermal structure is characterized by 11 parameters, (1) the temperature gradient at each of the 10 layers,  $(d\ln T/d\ln P)_i$ , where  $i = 1, 2, \dots, 10$ , and (2) the reference temperature,  $T_{\text{ref}}$ , at a pre-defined pressure  $P_{\text{ref}}$ .<sup>2</sup> With  $T_{\text{ref}}$  and the quadratically interpolated  $(d\ln T/d\ln P)_i$ , we construct the T-P profile over a finer grid of 1000 levels (for cloudy models) or 100 levels (for cloudless models) that are evenly spaced in  $\log P$ . The temperature at each pressure grid level (indexed by  $j$ ) is computed as:

$$\begin{aligned} T_{j^*} &= \exp \left[ \ln T_{\text{ref}} + (\ln P_{j^*} - \ln P_{\text{ref}}) \times \left( \frac{d\ln T}{d\ln P} \right)_{\text{ref}} \right], \\ &\quad \text{if } P_{\text{ref}} \notin \{10^3, 10^2, \dots, 10^{-6} \text{ bar}\} \\ T_{j\pm 1} &= \exp \left[ \ln T_j + (\ln P_{j\pm 1} - \ln P_j) \times \left( \frac{d\ln T}{d\ln P} \right)_j \right] \end{aligned} \quad (1)$$

Here, a larger  $j$  corresponds to a higher altitude or lower pressure, and  $j^*$  refers to the closest pressure grid level to the reference pressure if  $P_{\text{ref}}$  is not a direct pressure grid level.

As demonstrated by Zhang et al. (2023), modeling the thermal structure via temperature gradients (Equation 1) enables the incorporation of radiative-convective equilibrium (RCE) as parameterized priors for the T-P profiles. These priors can be derived from the temperature gradients of pre-computed atmospheric model grids, typically generated under RCE assumptions. Specifically, for a given atmospheric model grid, the T-P profile of each model spectrum is used to compute

the corresponding temperature gradient as a function of pressure, i.e.,  $(d\ln T/d\ln P)_{\text{RCE}}$ . Stacking the temperature gradient profiles of individual grid points offers insights into the distribution of  $(d\ln T/d\ln P)_{\text{RCE}}$  across pressure layers. These distributions help define the priors for the gradients in our temperature model. Using RCE priors mitigates the degeneracies between cloud properties and T-P profiles, preventing retrievals from converging on cloudless solutions for cloudy atmospheres, thus providing stronger constraints on cloud properties (see Sections 6.2 and 8.3 of Zhang et al. 2023). Additionally, while these priors naturally favour the T-P profiles with similar shapes of the RCE forward models, they do not fix the temperature gradients during the retrievals and thereby flexibly allow the T-P profiles to deviate from the RCE as in the scenarios proposed by Tremblin et al. (2016).

For the retrievals of 2MASS 1207 b, we set RCE priors for  $(d\ln T/d\ln P)$  following Section 6.2 of Zhang et al. (2023). We use the Sonora Diamondback models with  $T_{\text{eff}} \in [900, 1500]$  K,  $\log(g) \in [3.5, 4.5]$  dex,  $[M/H] \in [-0.5, +0.5]$  dex, and  $f_{\text{sed}} \in [1, 4]$ . This leads to a total of 252 grid points. The majority of these models extend from  $10^{-3}$  bar to  $10^2$  bar, so we adopt Gaussian priors for the  $(d\ln T/d\ln P)_i$  in this pressure range. Some Gaussian priors are further narrowed at a few pressure layers (Table 2) based on the skewed distributions of  $(d\ln T/d\ln P)_{\text{RCE}}$  from the Sonora Diamondback models. We use broad uniform priors for pressure layers with  $P < 10^{-3}$  bar or  $P > 10^2$  bar. These uniform priors are designed such that the potential upper-atmosphere thermal inversion (i.e.,  $d\ln T/d\ln P < 0$ ) is allowed.

## 5.2. Chemistry Model

### 5.2.1. Opacities

The atomic and molecular line species included in our retrievals are Na (Allard et al. 2019), K (Allard et al. 2016), H<sub>2</sub>O (Polyansky et al. 2018), CH<sub>4</sub> (Hargreaves et al. 2020), CO (Rothman et al. 2010), CO<sub>2</sub> (Yurchenko et al. 2020), NH<sub>3</sub> (Coles et al. 2019), PH<sub>3</sub> (Sousa-Silva et al. 2015), H<sub>2</sub>S (Az-zam et al. 2016), FeH (Dulick et al. 2003; Bernath 2020), VO (McKemmish et al. 2016), and TiO (McKemmish et al. 2019). We also account for Rayleigh scattering by H<sub>2</sub> (Dalgarno & Williams 1962) and He (Chan & Dalgarno 1965), and include the collision-induced absorption by H<sub>2</sub>–H<sub>2</sub> and H<sub>2</sub>–He (Borysow et al. 1988, 1989; Borysow & Frommhold 1989; Borysow et al. 2001; Borysow 2002; Richard et al. 2012).

### 5.2.2. An Expanded Grid of Chemical Equilibrium Abundances

`petitRADTRANS` includes a pre-computed grid of chemical-equilibrium abundances for key opacity sources as functions of  $[M/H]$  and C/O (Mollière et al. 2015, 2017, 2019). This grid provides a convenient proxy for atmospheric

<sup>2</sup> If a user-defined  $P_{\text{ref}}$  is not one of the 10 layers, its corresponding temperature gradient  $(d\ln T/d\ln P)_{\text{ref}}$  is computed using quadratic interpolation of  $(d\ln T/d\ln P)_i$ .

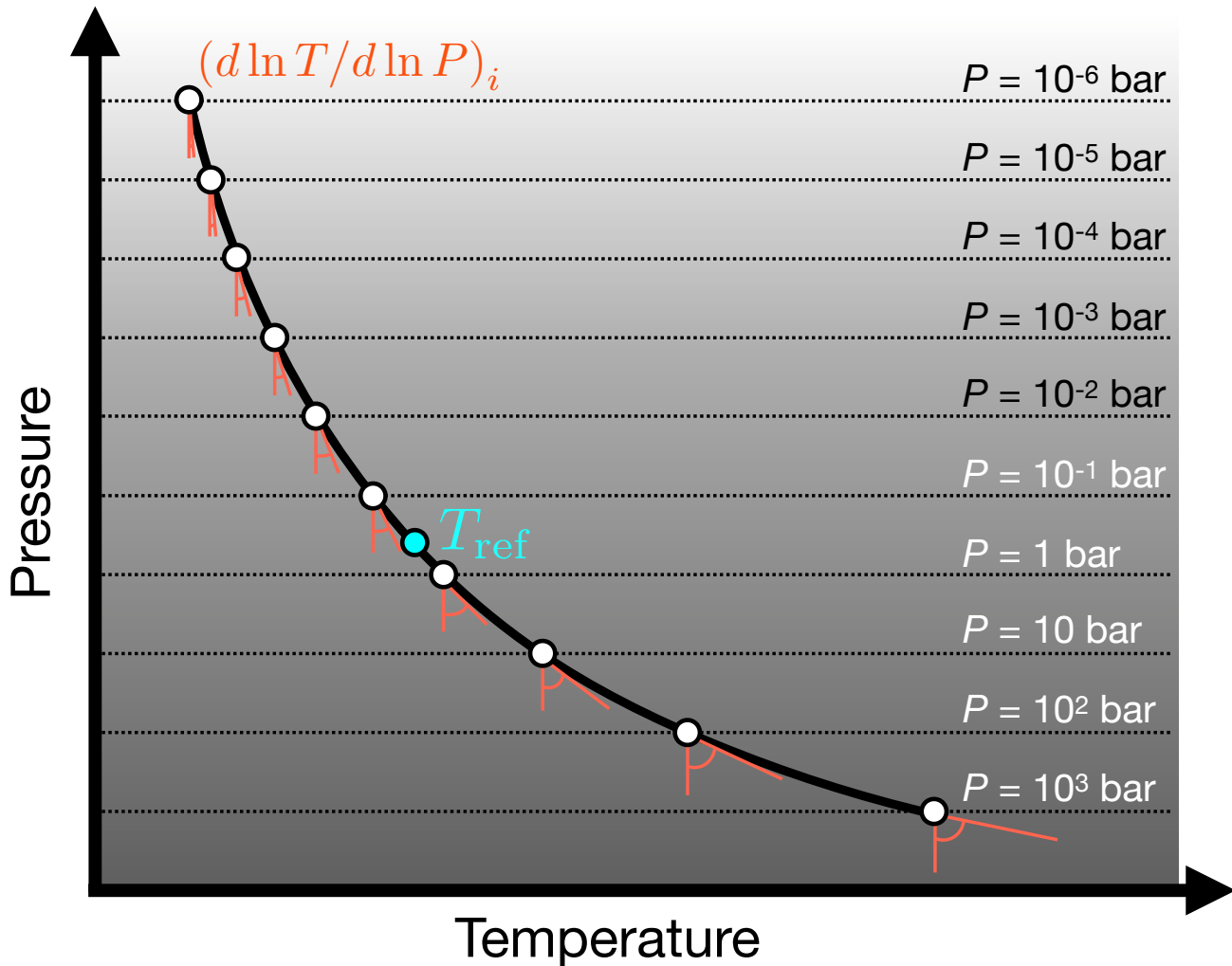


Figure 3. Sketch of the temperature model described in Section 5.1.

equilibrium chemistry in retrievals and has been widely used (e.g., Mollière et al. 2020; Kammerer et al. 2021; Xuan et al. 2022; Brown-Sevilla et al. 2023; Zhang et al. 2023; Balmer et al. 2024; Inglis et al. 2024; Hsu et al. 2024b; Nasedkin et al. 2024b).

In this work, we expand the `petitRADTRANS` chemical equilibrium abundance grid over an even broader parameter space and include more opacity sources. This new grid is computed using `easyCHEM`<sup>3</sup> (Mollière et al. 2017; Lei & Mollière 2024). Our grid spans [40 K, 6000 K] in temperature ( $T$ ), [ $10^{-8}$  bar,  $10^3$  bar] in pressure ( $P$ ), [−2 dex, +3 dex] in [M/H], and [0.1, 1.6] in C/O, with 120, 100, 40, and 20 grid points, respectively. These grid points are evenly spaced logarithmically for  $T$  and  $P$  and linearly for [M/H] and C/O. Compared to the grid from Mollière et al. (2019), this new grid extends to higher temperatures and includes ad-

ditional species, such as AlH,  $C_2$ , CN, OH, Al, Ca, Fe, Mg, Si, and Ti. This grid is available via the Zenodo repository, <https://doi.org/10.5281/zenodo.15654694>.

### 5.2.3. Chemical Abundance Profiles

Our retrievals assume chemical equilibrium and account for disequilibrium effects of carbon chemistry. We compute abundance profiles of atomic and molecular species based on equilibrium chemistry for a given [M/H] and C/O (Section 5.2.2). An additional free parameter, the carbon-chemistry quench pressure ( $P_{\text{quench}}$ ), accounts for disequilibrium chemistry. At pressures smaller than  $P_{\text{quench}}$ , the abundances of  $H_2O$ , CO, and  $CH_4$  are reset to their values at  $P_{\text{quench}}$  (e.g., Zahnle & Marley 2014).

### 5.3. Cloud Model

Our cloud model is based on the prescriptions by Ackerman & Marley (2001). The free parameters include (1)  $\sigma_g$ , the standard deviation of the log-normal cloud particle size

<sup>3</sup> <https://easychem.readthedocs.io/en/latest/>

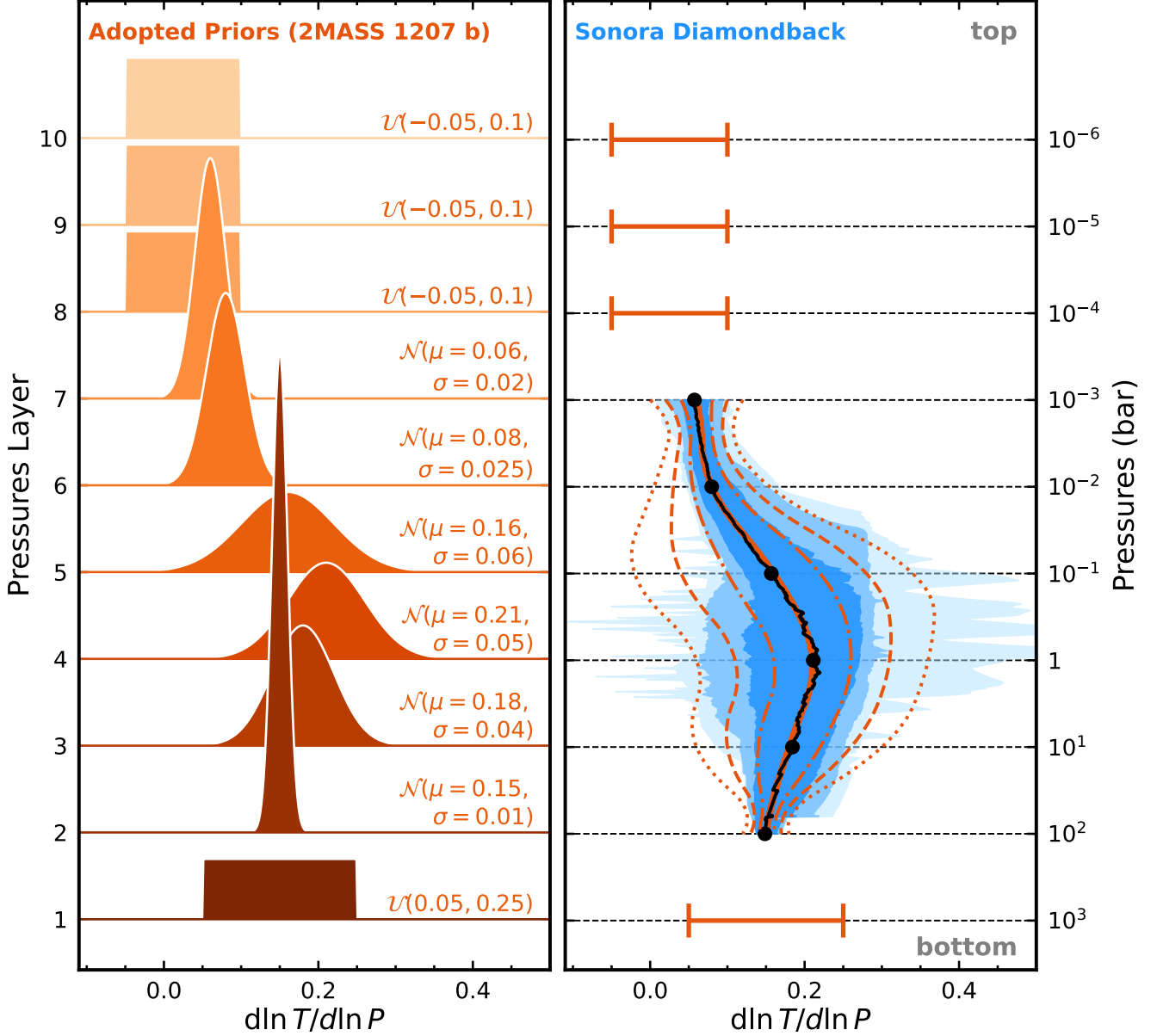


**Figure 4.** *Left:* Our adopted priors for the temperature gradient, ( $d \ln T / d \ln P$ ), at each of the 10 pressure layers evenly spaced in  $\log P$  from  $10^3$  bar (layer 1) to  $10^{-6}$  bar (layer 10). *Right:* The  $1\sigma/2\sigma/3\sigma$  (from dark to light blues) confidence intervals of the  $(d \ln T / d \ln P)_{\text{RCE}}$  profiles computed from the Sonora Diamondback models. The black solid line represents the median  $(d \ln T / d \ln P)_{\text{RCE}}$  profile, with black circles corresponding to the temperature gradient values at the 10 pre-defined layers. For pressures between  $10^2$  bar and  $10^{-3}$  bar, we use orange lines to highlight the median values (solid), as well as the  $1\sigma$  (dash-dotted),  $2\sigma$  (dashed), and  $3\sigma$  boundaries (dotted) of our adopted Gaussian priors. For pressure layers with  $P < 10^{-3}$  bar or  $P > 10^2$  bar, the adopted uniform prior is indicated by horizontal error bars.

distribution; (2)  $K_{zz}$ , the eddy diffusion coefficient; (3)  $f_{\text{sed}}$ , the condensate sedimentation efficiency; and (4)  $X_0^{(c)}$ , the cloud mass fraction at the cloud base pressure. When multiple cloud species or multiple atmospheric columns (under the inhomogeneous scenario; Section 5.4) are modeled, we assume that  $\sigma_g$  and  $K_{zz}$  are shared by all cloud species within a given column. However,  $f_{\text{sed}}$  and  $X_0^{(c)}$  are allowed to vary

between different cloud species within the same column or for the same cloud species across different columns.

The base pressure for each cloud species is computed by comparing the T-P profile to its condensation curve derived from equilibrium chemistry. However, in some retrieval runs, the cloud base pressure for a given cloud species,  $P_{\text{base}}^{(c)}$ , is treated as a free parameter.

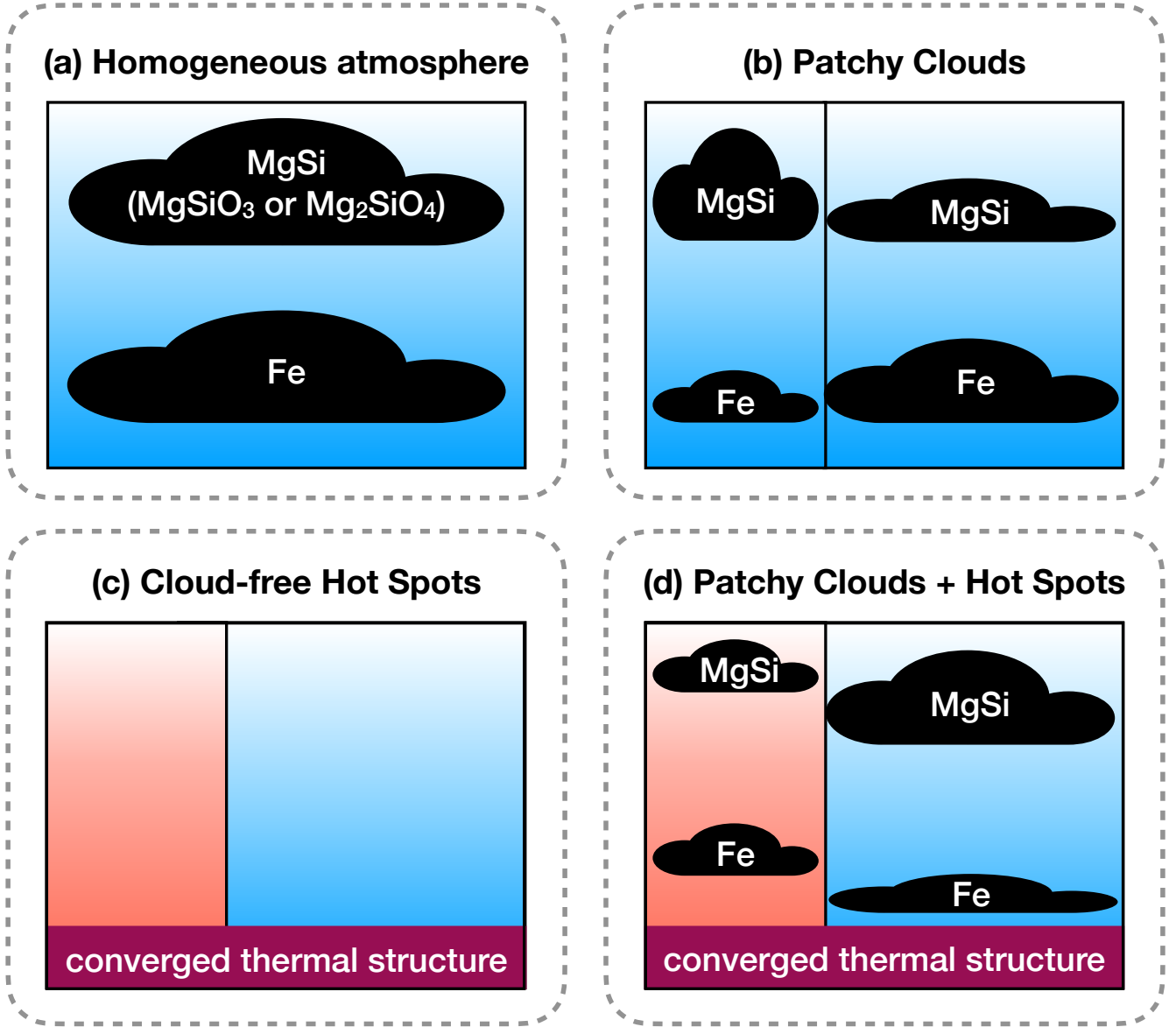


**Figure 5.** Four schemes in our atmospheric inhomogeneity framework (Section 5.4).

Our retrievals are performed using both cloud-free and cloudy scenarios. For the cloudy setups, we test various combinations of cloud species, including amorphous silicates<sup>4</sup> of forsterite ( $\text{Mg}_2\text{SiO}_4$ ) and enstatite ( $\text{MgSiO}_3$ ) stoichiometry (Jäger et al. 2003) and iron (Fe; Pollack et al. 1994) with Mie scattering particle shapes. Additionally, in some cloudy retrieval runs, we incorporate a gray cloud layer with a varying pressure  $P_{\text{gray}}$ ; the opacity for deeper pressure layers with

$P > P_{\text{gray}}$ ,  $\kappa_{\text{gray}}$ , is introduced as a free parameter, assumed to remain constant as a function of pressures.

#### 5.4. Atmospheric Inhomogeneity Framework

Traditional atmospheric retrieval analyses often assume one-dimensional, homogeneous atmospheres (Section 1). However, this simplification may not suffice for certain exoplanets and brown dwarfs exhibiting top-of-atmosphere inhomogeneities indicated by variability monitoring. Patchy clouds and hot spots have been suggested as two primary mechanisms driving such variabilities, highlighting the need for more sophisticated atmospheric models to accurately retrieve the properties of variable objects, such as 2MASS 1207 b.

<sup>4</sup> We focus on  $\text{Mg}_2\text{SiO}_4$  and  $\text{MgSiO}_3$  clouds in this work but note that the upcoming MIRI spectra will better constrain the specific type of silicate clouds in 2MASS 1207 b's atmosphere (GTO program 1270), as well as its potential circumsecondary disk.

To address this, we introduce a new retrieval framework comprising four schemes (Figure 5), designed to characterize both homogeneous and inhomogeneous atmospheres of exoplanets, brown dwarfs, and low-mass stars.<sup>5</sup>

#### 5.4.1. Scheme (a): homogeneous Atmosphere

This scheme represents the most widely used retrieval approach for brown dwarfs and directly imaged exoplanets (e.g., Line et al. 2015, 2017; Burningham et al. 2017; Gonzales et al. 2020; Mollière et al. 2020; Zhang et al. 2021a; Xuan et al. 2022; Zhang et al. 2023; Lew et al. 2024). In this work, we explore scenarios of (1) a cloud-free atmosphere, (2) a combination of Fe and MgSiO<sub>3</sub> clouds, and (3) a combination of Fe and Mg<sub>2</sub>SiO<sub>4</sub> clouds. The T-P profile is modeled using the temperature gradients at ten pressure layers (as described in Section 5.1) and a reference pressure of 0.1 bar, i.e.,  $T_{\text{ref}} = T_{0.1 \text{ bar}}$ .

#### 5.4.2. Scheme (b): patchy clouds

Patchy clouds, or spatial inhomogeneities in cloud cover and thickness, are observed in the atmospheres of Earth, Jupiter, and Saturn and are suggested for self-luminous exoplanets and brown dwarfs (e.g., Ackerman & Marley 2001; Burgasser et al. 2002; Marley et al. 2010; Apai et al. 2013). In this scheme, we model patchy clouds by combining two atmospheric columns that share the same T-P profile but differ in cloud properties (see also Marley et al. 2010; Morley et al. 2014; Lew et al. 2016; Vos et al. 2023). For each column, we use the setup from the scheme (a) and explore combinations of Fe and MgSiO<sub>3</sub> clouds or Fe and Mg<sub>2</sub>SiO<sub>4</sub> clouds. The same cloud species are used for both columns, but their properties —  $\sigma_g$ ,  $K_{zz}$ ,  $f_{\text{sed}}$ , and  $X_0^{(c)}$  — are allowed to vary (even for the same species).

The emergent spectrum is computed as:

$$F_\lambda = \xi_{\text{thin}} \times F_{\lambda, \text{thin}} + (1 - \xi_{\text{thin}}) \times F_{\lambda, \text{thick}} \quad (2)$$

Here,  $F_{\lambda, \text{thin}}$  represents the spectrum from the atmospheric column with less cloud content (thin clouds), and  $F_{\lambda, \text{thick}}$  represents the spectrum from the column with thicker clouds. The free parameter  $\xi_{\text{thin}}$  describes the fraction of the thin-cloud column (i.e., column 1).

This scheme accommodates an extreme scenario, such as cloud decks with completely depleted cloud holes, and an intermediate case, such as a combination of thin and thick clouds.

<sup>5</sup> We note that our retrieval framework can also be flexibly adapted to model the blended spectra of unresolved binaries or multiple systems.

#### 5.4.3. Scheme (c): cloud-free hot spots

Inhomogeneities in atmospheric thermal structures, or hot spots, may also explain the observed variabilities of exoplanets and brown dwarfs (e.g., Zhang & Showman 2014; Robinson & Marley 2014; Tan & Showman 2019; Apai et al. 2017; Showman et al. 2019; Tan & Showman 2021; Lee et al. 2023). These temperature variations may be induced by dynamic processes such as moist convection, cloud radiative feedback, thermal perturbations, or planetary-scale waves (see also Zhang 2020). Although clouds are often invoked in relevant dynamic modeling efforts, certain processes, such as thermocompositional diabatic convection, are theorized to occur in the atmospheres without any clouds (Tremblin et al. 2016, 2019, 2020).

We simplify this scenario by combining two cloud-free atmospheric columns with non-identical T-P profiles. Each T-P profile is modeled following Section 5.1, but unlike schemes (a) and (b), we use a reference pressure of 10 bar, i.e.,  $T_{\text{ref}} = T_{10 \text{ bar}}$ . To ensure that the thermal structures of the two atmospheric columns converge in the deep atmosphere or interior, we require both two T-P profiles to share the same  $T_{10 \text{ bar}}$  and temperature gradients at 10 bar, 10<sup>2</sup> bar, and 10<sup>3</sup> bar. The choice of a 10 bar reference pressure aligns with the typical location of surface boundary conditions used when coupling atmospheric models with thermal evolution models (e.g., Saumon et al. 1996; Burrows et al. 1997; Saumon & Marley 2008). For the upper atmospheres with  $P < 10$  bar, we allow the two T-P profiles to have different temperature gradients and temperatures, reflecting variations in the balance between radiative cooling and dynamical timescales in these two columns.

The emergent spectrum is computed as:

$$F_\lambda = \xi_{\text{thin}} \times F_{\lambda, \text{hot}} + (1 - \xi_{\text{thin}}) \times F_{\lambda, \text{cold}} \quad (3)$$

Here,  $F_{\lambda, \text{hot}}$  and  $F_{\lambda, \text{cold}}$  represent the spectra from the hotter and colder regions, respectively. We keep the notation  $\xi_{\text{thin}}$  in Equation 2 to describe the surface fraction of hot spots.

#### 5.4.4. Scheme (d): the combination of patchy clouds and hot spots.

This scheme combines schemes (b) and (c), enabling the coexistence of patchy clouds and temperature variations within the atmosphere. We configure the cloud properties following scheme (b) and model the T-P profiles following scheme (c).

### 5.5. Nested Sampling and Free Parameters

Our retrievals are performed using nested sampling algorithm MultiNest (Feroz & Hobson 2008; Feroz et al. 2009, 2019) via its Python wrapper PyMultiNest (Buchner et al. 2014). This algorithm has been extensively applied in various fields, including cosmology (e.g., Planck

**Table 2.** Free Parameters of Retrievals

Parameter	Prior	Description
Temperature Model (Sections 5.1)		
$T_{0.1}$	$\mathcal{U}(500 \text{ K}, 4000 \text{ K})$	Temperature at $P = 0.1$ bar in schemes (a–b) (Section 5.4)
$T_{10}$	$\mathcal{U}(500 \text{ K}, 7000 \text{ K})$	Temperature at $P = 10$ bar in schemes (c–d) (Section 5.4)
$(d \ln T / d \ln P)_1$	$\mathcal{U}(0.05, 0.25)$	Temperature gradient at $P = 10^3$ bar.
$(d \ln T / d \ln P)_2$	$\mathcal{N}(\mu = 0.15, \sigma = 0.01)$ , within $[-2\sigma, +2\sigma]$	Temperature gradient at $P = 10^2$ bar.
$(d \ln T / d \ln P)_3$	$\mathcal{N}(\mu = 0.18, \sigma = 0.04)$ , within $[-2\sigma, +2\sigma]$	Temperature gradient at $P = 10^1$ bar.
$(d \ln T / d \ln P)_4$	$\mathcal{N}(\mu = 0.21, \sigma = 0.05)$ , within $[-2\sigma, +2\sigma]$	Temperature gradient at $P = 10^0$ bar.
$(d \ln T / d \ln P)_5$	$\mathcal{N}(\mu = 0.16, \sigma = 0.06)$ , within $[-1\sigma, +2\sigma]$	Temperature gradient at $P = 10^{-1}$ bar.
$(d \ln T / d \ln P)_6$	$\mathcal{N}(\mu = 0.08, \sigma = 0.025)$ , within $[-1\sigma, +2\sigma]$	Temperature gradient at $P = 10^{-2}$ bar.
$(d \ln T / d \ln P)_7$	$\mathcal{N}(\mu = 0.06, \sigma = 0.02)$ , within $[-2\sigma, +2\sigma]$	Temperature gradient at $P = 10^{-3}$ bar.
$(d \ln T / d \ln P)_8$	$\mathcal{U}(-0.05, 0.10)$	Temperature gradient at $P = 10^{-4}$ bar.
$(d \ln T / d \ln P)_9$	$\mathcal{U}(-0.05, 0.10)$	Temperature gradient at $P = 10^{-5}$ bar.
$(d \ln T / d \ln P)_{10}$	$\mathcal{U}(-0.05, 0.10)$	Temperature gradient at $P = 10^{-6}$ bar.
Chemistry Model (Section 5.2)		
[M/H]	$\mathcal{U}(-1 \text{ dex}, 2 \text{ dex})$	Atmospheric metallicity.
C/O	$\mathcal{U}(0.1, 1.6)$	Atmospheric carbon-to-oxygen ratio.
$\log(P_{\text{quench}})$	$\mathcal{U}(-6 \text{ dex}, 3 \text{ dex})$	Quench pressure of $\text{H}_2\text{O}$ , $\text{CH}_4$ , and $\text{CO}$ (unit: bar).
Cloud Model (Section 5.3) <sup>a</sup>		
$\sigma_g$	$\mathcal{U}(1.02, 3)$	Width of the log-normal cloud particle size distribution.
$\log(K_{zz})$	$\mathcal{U}(5 \text{ dex}, 13 \text{ dex})$	Vertical eddy diffusion coefficient of clouds.
$f_{\text{sed}}$	$\mathcal{U}(0, 10)$	Sedimentation efficiency of a given cloud species. <sup>b</sup>
$\log(X_0^{(c)})$	$\mathcal{U}(-10, 0)$	Mass fraction of a given cloud species at its base pressure. <sup>b</sup>
$\log(P_{\text{base}}^{(c)})$	$\mathcal{U}(-6, 3)$	Base pressure of a given cloud species (unit: bar). <sup>b</sup>
$\log(P_{\text{gray}})$	$\mathcal{U}(-6, -1)$	Pressure of the gray cloud layer (unit: bar).
$\log(\kappa_{\text{gray}})$	$\mathcal{U}(-6, 9)$	Opacity below the gray cloud layer (unit: $\text{cm}^2/\text{g}$ ).
Atmospheric Inhomogeneity (Section 5.4)		
$\xi_{\text{thin}}$	$\mathcal{U}(0, 1)$	Fraction of one atmospheric column in schemes (b–d) (Section 5.4).
Other Parameters (Section 5.5) <sup>c</sup>		
$\log(g)$	$\mathcal{U}(2.5 \text{ dex}, 5.5 \text{ dex})$ or $\mathcal{U}(3.54 \text{ dex}, 4.02 \text{ dex})$	Surface gravity (unit: $\text{cm}/\text{s}^2$ ). A narrower prior constrained by thermal evolution (Section 4.2)
$R$	$\mathcal{U}(0.5 R_{\text{Jup}}, 2.5 R_{\text{Jup}})$ or $\mathcal{U}(1.30 R_{\text{Jup}}, 1.55 R_{\text{Jup}})$	Radius. A narrower prior constrained by thermal evolution (Section 4.2)
$\log(b_{\text{chunk}})$	$\mathcal{U}(\log(\min(\sigma_{\text{chunk}})), \log(10^3 \times \max(\sigma_{\text{chunk}})))$	Additive flux error of each wavelength chunk of JWST/NIRSPEC.

<sup>a</sup>For most of our retrieval runs, the base pressure of a given cloud species is self-consistently computed following equilibrium chemistry, but several retrieval runs treat the cloud base pressures,  $\log(P_{\text{base}}^{(c)})$ , as free parameters.

<sup>b</sup>The cloud species in our retrievals include Fe,  $\text{MgSiO}_3$ , and  $\text{Mg}_2\text{SiO}_4$ . The  $f_{\text{sed}}$ ,  $\log(X_0^{(c)})$ , and  $\log(P_{\text{base}}^{(c)})$  values vary across different cloud species within the same atmospheric column or the same cloud species from different columns (Section 5.3).

<sup>c</sup>Some of our retrieval runs adopt the physically motivated narrower priors for  $\log(g)$ , radius, and mass as determined by thermal evolution models (Section 4.2). When the evolution-based priors for  $\log(g)$  and  $R$  are used in retrievals, we assume a uniform prior for  $M$  of  $\mathcal{U}(3.0 M_{\text{Jup}}, 7.5 M_{\text{Jup}})$ .

Collaboration et al. 2014), particle physics (e.g., Trotta et al. 2008), and X-ray astronomy (e.g., Buchner et al. 2014), and is among the most widely used tools for atmospheric retrieval analyses of exoplanets and brown dwarfs (see a list of retrieval packages summarized by MacDonald & Batalha 2023). Recently, Dittmann (2024) suggested that combining PyMultiNest with complementary algorithms, such as the Markov-chain Monte Carlo (e.g., Foreman-Mackey et al. 2013), could help address potential limitations of individual techniques and improve the robustness of parameter inference. This practice remains rare in the field considering the computational demands, particularly when multiple retrieval runs are required, but it represents an important direction for future studies. For the scope of this work, we focus on using PyMultiNest and set 2000 live points and a constant sampling efficiency of 0.05. The spectral resolution of the JWST/NIRSpec spectrum is downgraded from  $R \sim 2700$  to  $R = 1000$  to manage the computational cost of the multiple retrieval runs conducted in this work, especially since the cloud scattering included in our retrieval runs are numerically expensive.

In addition to the parameters described in previous sections, we introduce a hyper-parameter,  $\log(b)$ , for each of the four segments of the JWST/NIRSpec spectrum, separated by the wavelength gaps of the G140H, G235H, and G395H gratings. These hyper-parameters are added to the measured flux uncertainties in quadrature when evaluating the log-likelihood, addressing (1) any underestimation of flux uncertainties in the observed NIRSpec spectra and (2) systematic differences between models and data. The surface gravity ( $\log(g)$ ) and radius ( $R$ ) of 2MASS 1207 b are also constrained by our retrievals. The free parameters and priors in our analysis are summarized in Table 2.

## 6. RETRIEVING THE JWST/NIRSPEC SPECTRUM OF 2MASS 1207 b

We have performed multiple retrieval analyses on the JWST/NIRSpec spectrum of 2MASS 1207 b using an extensive array of setups. These setups explore the effects of variations in the following properties:

- Atmospheric inhomogeneity. We investigate all four atmospheric schemes described in Section 5.4 and Figure 5, including homogeneous atmospheres, patchy clouds, cloud-free hot spots, and the combination of patchy clouds and hot spots.
- Priors for surface gravity, radius, and mass. Both broad and narrow priors are explored for these parameters (Table 2), with the narrow priors informed by thermal

evolution models using the bolometric luminosity and age of 2MASS 1207 b (Section 4).

- Cloud composition. We consider several combinations of cloud species, including (1)  $\text{Mg}_2\text{SiO}_4$  and Fe clouds, (2)  $\text{Mg}_2\text{SiO}_4$ , Fe, and gray clouds, (3)  $\text{MgSiO}_3$  and Fe clouds, (4)  $\text{MgSiO}_3$ , Fe, and gray clouds, and (5) cloud-free atmospheres. For inhomogeneous atmospheres, we assume the same cloud composition for both atmospheric columns, but the cloud properties are allowed to vary between columns. When included, gray clouds are confined to the second atmospheric column.
- Cloud base pressure. Most of our retrievals compute cloud base pressures assuming chemical equilibrium. However, we treat the base pressures of magnesium silicate clouds and/or iron clouds as additional free parameters in certain retrieval runs.

We have conducted 24 retrieval runs with variations in the setups described above. These runs incorporate chemical equilibrium and quench pressures for carbon chemistry ( $\text{CO}$ ,  $\text{CH}_4$ ,  $\text{H}_2\text{O}$ ) and are labeled as QEQ throughout this work. We further derive the posterior distribution of bolometric luminosities for each retrieval run by integrating the spectra computed from the retrieved parameters. Using the Stefan-Boltzmann law, we calculate the posterior distributions of effective temperatures based on  $L_{\text{bol}}$  and the retrieved  $R$ . Median values and confidence intervals of key retrieved parameters are summarized in Tables 3–4.

To evaluate the performance of each retrieval run, we calculate the Bayesian Information Criterion (BIC; Schwarz 1978; Liddle 2007):

$$\text{BIC} \equiv -2 \ln \mathcal{L}_{\text{max}} + k \ln N \quad (4)$$

where  $N$  is the number of NIRSpec wavelength elements,  $k$  is the number of free parameters, and  $\mathcal{L}_{\text{max}}$  is the maximum likelihood. The retrieval run with the lowest BIC value is considered the most preferred model for explaining the observations. The significance of this preference over another run is assessed by the difference in their BIC values, i.e.,  $\Delta\text{BIC}$ . According to Kass & Raftery (1995), such preference is absent if  $0 < \Delta\text{BIC} < 2$ , indicated if  $2 < \Delta\text{BIC} < 6$ , strongly indicated if  $6 < \Delta\text{BIC} < 10$ , and very strongly indicated if  $\Delta\text{BIC} > 10$ .

In our analysis, the lowest BIC corresponds to a patchy cloud scenario with inhomogeneous forsterite and iron clouds, identified as the scheme (b) in our atmospheric inhomogeneity framework (Section 5.4). This run outperforms other runs with  $\Delta\text{BIC}$  values ranging from 4 to nearly 5000, making it the most favored model for interpreting the JWST NIRSpec spectrum of 2MASS 1207 b. Throughout this manuscript, we refer to this most preferred model as QEQ-1

**Table 3.** Retrieved properties of 2MASS 1207 b (Quenching + Equilibrium Chemistry): Fundamental Parameters

Label <sup>a</sup>	$\Delta\text{BIC}^b$	Atmospheric Setup				$T_{\text{eff}}$ (K)	$\log(g)$ (dex)	$R$ ( $R_{\text{Jup}}$ )	[M/H] (dex)	C/O	$\log(P_{\text{quench}})$ (bar)
		Column 1	Column 2	Cloud Base <sup>c</sup>	Priors <sup>d</sup>						
Scheme (b): Patchy Clouds (Figure 5)											
QE-Q-1	0	Forsterite <sup>(1)</sup> +Iron <sup>(1)</sup>	Forsterite <sup>(2)</sup> +Iron <sup>(2)</sup>	CEQ	Evo.	1174 <sup>+4</sup> <sub>-3</sub>	3.62 <sup>+0.03</sup> <sub>-0.02</sub>	1.399 <sup>+0.008</sup> <sub>-0.010</sub>	-0.05 <sup>+0.03</sup> <sub>-0.03</sub>	0.440 <sup>+0.012</sup> <sub>-0.012</sub>	-3.3 <sup>+1.2</sup> <sub>-1.2</sub>
QE-Q-2	4	Forsterite <sup>(1)</sup> +Iron <sup>(1)</sup>	Forsterite <sup>(2)</sup> +Iron <sup>(2)</sup>	Flex. MgSi	Evo.	1136 <sup>+6</sup> <sub>-6</sub>	3.58 <sup>+0.03</sup> <sub>-0.02</sub>	1.492 <sup>+0.018</sup> <sub>-0.016</sub>	-0.12 <sup>+0.04</sup> <sub>-0.04</sub>	0.459 <sup>+0.014</sup> <sub>-0.016</sub>	-3.7 <sup>+1.2</sup> <sub>-1.2</sub>
QE-Q-3	42	Enstatite <sup>(1)</sup> +Iron <sup>(1)</sup>	Enstatite <sup>(2)</sup> +Iron <sup>(2)</sup>	CEQ	Evo.	1199 <sup>+5</sup> <sub>-5</sub>	3.65 <sup>+0.02</sup> <sub>-0.02</sub>	1.334 <sup>+0.012</sup> <sub>-0.012</sub>	-0.01 <sup>+0.03</sup> <sub>-0.03</sub>	0.451 <sup>+0.011</sup> <sub>-0.012</sub>	-3.7 <sup>+1.2</sup> <sub>-1.2</sub>
QE-Q-4	89	Forsterite <sup>(1)</sup> +Iron <sup>(1)</sup>	Forsterite <sup>(2)</sup> +Iron <sup>(2)</sup> +Gray	CEQ	Evo.	1203 <sup>+3</sup> <sub>-3</sub>	3.67 <sup>+0.04</sup> <sub>-0.02</sub>	1.322 <sup>+0.008</sup> <sub>-0.007</sub>	0.09 <sup>+0.03</sup> <sub>-0.03</sub>	0.486 <sup>+0.013</sup> <sub>-0.013</sub>	-3.8 <sup>+1.1</sup> <sub>-1.1</sub>
QE-Q-5	92	Enstatite <sup>(1)</sup> +Iron <sup>(1)</sup>	Enstatite <sup>(2)</sup> +Iron <sup>(2)</sup> +Gray	CEQ	Evo.	1206 <sup>+2</sup> <sub>-2</sub>	3.67 <sup>+0.03</sup> <sub>-0.02</sub>	1.315 <sup>+0.005</sup> <sub>-0.005</sub>	0.10 <sup>+0.03</sup> <sub>-0.03</sub>	0.506 <sup>+0.011</sup> <sub>-0.011</sub>	-3.8 <sup>+1.1</sup> <sub>-1.1</sub>
QE-Q-10	333	Enstatite <sup>(1)</sup> +Iron <sup>(1)</sup>	Enstatite <sup>(2)</sup> +Iron <sup>(2)</sup>	Flex. MgSi	Evo.	1192 <sup>+3</sup> <sub>-3</sub>	3.63 <sup>+0.01</sup> <sub>-0.01</sub>	1.353 <sup>+0.007</sup> <sub>-0.007</sub>	0.15 <sup>+0.02</sup> <sub>-0.03</sub>	0.358 <sup>+0.012</sup> <sub>-0.014</sub>	-3.5 <sup>+1.0</sup> <sub>-1.0</sub>
Scheme (d): Patchy Clouds + Hot Spots (Figure 5)											
QE-Q-6	109	Enstatite <sup>(1)</sup> +Iron <sup>(1)</sup>	Enstatite <sup>(2)</sup> +Iron <sup>(2)</sup>	CEQ	Broad	1221 <sup>+6</sup> <sub>-7</sub>	3.40 <sup>+0.07</sup> <sub>-0.07</sub>	1.286 <sup>+0.014</sup> <sub>-0.014</sub>	0.02 <sup>+0.03</sup> <sub>-0.03</sub>	0.522 <sup>+0.014</sup> <sub>-0.012</sub>	-3.9 <sup>+1.0</sup> <sub>-1.0</sub>
QE-Q-7	123	Forsterite <sup>(1)</sup> +Iron <sup>(1)</sup>	Forsterite <sup>(2)</sup> +Iron <sup>(2)</sup>	CEQ	Broad	1235 <sup>+6</sup> <sub>-6</sub>	3.62 <sup>+0.08</sup> <sub>-0.06</sub>	1.256 <sup>+0.012</sup> <sub>-0.012</sub>	0.05 <sup>+0.03</sup> <sub>-0.02</sub>	0.468 <sup>+0.013</sup> <sub>-0.015</sub>	-3.8 <sup>+1.1</sup> <sub>-1.1</sub>
QE-Q-8	165	Forsterite <sup>(1)</sup> +Iron <sup>(1)</sup>	Forsterite <sup>(2)</sup> +Iron <sup>(2)</sup> +Gray	CEQ	Broad	1392 <sup>+3</sup> <sub>-2</sub>	3.34 <sup>+0.06</sup> <sub>-0.05</sub>	0.987 <sup>+0.003</sup> <sub>-0.004</sub>	0.07 <sup>+0.03</sup> <sub>-0.03</sub>	0.531 <sup>+0.010</sup> <sub>-0.013</sub>	-4.1 <sup>+0.9</sup> <sub>-0.9</sub>
QE-Q-9	169	Forsterite <sup>(1)</sup> +Iron <sup>(1)</sup>	Forsterite <sup>(2)</sup> +Iron <sup>(2)</sup> +Gray	CEQ	Evo.	1209 <sup>+1</sup> <sub>-1</sub>	3.70 <sup>+0.04</sup> <sub>-0.03</sub>	1.309 <sup>+0.002</sup> <sub>-0.003</sub>	0.18 <sup>+0.02</sup> <sub>-0.02</sub>	0.522 <sup>+0.009</sup> <sub>-0.009</sub>	-3.4 <sup>+0.8</sup> <sub>-0.9</sub>
QE-Q-11	532	Enstatite <sup>(1)</sup> +Iron <sup>(1)</sup>	Enstatite <sup>(2)</sup> +Iron <sup>(2)</sup>	CEQ	Evo.	1191 <sup>+1</sup> <sub>-1</sub>	3.61 <sup>+0.01</sup> <sub>-0.00</sub>	1.364 <sup>+0.003</sup> <sub>-0.003</sub>	0.34 <sup>+0.02</sup> <sub>-0.02</sub>	0.322 <sup>+0.008</sup> <sub>-0.008</sub>	-3.5 <sup>+1.2</sup> <sub>-1.2</sub>
QE-Q-12	586	Enstatite <sup>(1)</sup> +Iron <sup>(1)</sup>	Enstatite <sup>(2)</sup> +Iron <sup>(2)</sup> +Gray	CEQ	Broad	1381 <sup>+1</sup> <sub>-1</sub>	2.54 <sup>+0.02</sup> <sub>-0.02</sub>	1.002 <sup>+0.002</sup> <sub>-0.002</sub>	-0.20 <sup>+0.02</sup> <sub>-0.03</sub>	0.483 <sup>+0.010</sup> <sub>-0.010</sub>	-3.8 <sup>+0.8</sup> <sub>-0.8</sub>
QE-Q-13	589	Forsterite <sup>(1)</sup> +Iron <sup>(1)</sup>	Forsterite <sup>(2)</sup> +Iron <sup>(2)</sup>	CEQ	Evo.	1186 <sup>+2</sup> <sub>-2</sub>	3.60 <sup>+0.01</sup> <sub>-0.01</sub>	1.374 <sup>+0.006</sup> <sub>-0.006</sub>	-0.17 <sup>+0.03</sup> <sub>-0.02</sub>	0.199 <sup>+0.010</sup> <sub>-0.010</sub>	-3.6 <sup>+1.5</sup> <sub>-1.3</sub>
QE-Q-18	907	Enstatite <sup>(1)</sup> +Iron <sup>(1)</sup>	Enstatite <sup>(2)</sup> +Iron <sup>(2)</sup> +Gray	CEQ	Evo.	1143 <sup>+4</sup> <sub>-4</sub>	3.58 <sup>+0.02</sup> <sub>-0.02</sub>	1.469 <sup>+0.011</sup> <sub>-0.011</sub>	0.86 <sup>+0.03</sup> <sub>-0.03</sub>	0.115 <sup>+0.010</sup> <sub>-0.007</sub>	-3.4 <sup>+1.2</sup> <sub>-1.2</sub>
Scheme (a): Homogeneous Atmosphere (Figure 5)											
QE-Q-14	610	Forsterite <sup>(1)</sup> +Iron <sup>(1)</sup>	N/A	CEQ	Broad	1239 <sup>+2</sup> <sub>-2</sub>	2.51 <sup>+0.01</sup> <sub>-0.01</sub>	1.248 <sup>+0.004</sup> <sub>-0.003</sub>	0.13 <sup>+0.02</sup> <sub>-0.02</sub>	0.593 <sup>+0.010</sup> <sub>-0.010</sub>	2.0 <sup>+0.0</sup> <sub>-0.0</sub>
QE-Q-15	622	Enstatite <sup>(1)</sup> +Iron <sup>(1)</sup>	N/A	Flex. Both	Evo.	1122 <sup>+2</sup> <sub>-2</sub>	3.57 <sup>+0.02</sup> <sub>-0.02</sub>	1.530 <sup>+0.005</sup> <sub>-0.005</sub>	0.94 <sup>+0.02</sup> <sub>-0.02</sub>	0.848 <sup>+0.004</sup> <sub>-0.004</sub>	1.9 <sup>+0.0</sup> <sub>-0.0</sub>
QE-Q-16	693	Enstatite <sup>(1)</sup> +Iron <sup>(1)</sup>	N/A	CEQ	Broad	1215 <sup>+1</sup> <sub>-1</sub>	2.50 <sup>+0.00</sup> <sub>-0.00</sub>	1.295 <sup>+0.003</sup> <sub>-0.003</sub>	0.33 <sup>+0.03</sup> <sub>-0.03</sub>	0.660 <sup>+0.002</sup> <sub>-0.002</sub>	1.6 <sup>+0.1</sup> <sub>-0.1</sub>
QE-Q-17	753	Forsterite <sup>(1)</sup> +Iron <sup>(1)</sup>	N/A	Flex. Both	Evo.	1136 <sup>+2</sup> <sub>-2</sub>	3.58 <sup>+0.02</sup> <sub>-0.02</sub>	1.488 <sup>+0.005</sup> <sub>-0.005</sub>	0.83 <sup>+0.02</sup> <sub>-0.01</sub>	0.837 <sup>+0.003</sup> <sub>-0.003</sub>	1.7 <sup>+0.0</sup> <sub>-0.0</sub>
QE-Q-19	963	Forsterite <sup>(1)</sup> +Iron <sup>(1)</sup>	N/A	CEQ	Evo.	1214 <sup>+1</sup> <sub>-1</sub>	3.65 <sup>+0.01</sup> <sub>-0.00</sub>	1.302 <sup>+0.002</sup> <sub>-0.002</sub>	0.22 <sup>+0.04</sup> <sub>-0.04</sub>	0.169 <sup>+0.031</sup> <sub>-0.026</sub>	-0.4 <sup>+0.5</sup> <sub>-3.6</sub>
QE-Q-20	984	Enstatite <sup>(1)</sup> +Iron <sup>(1)</sup>	N/A	CEQ	Evo.	1214 <sup>+1</sup> <sub>-1</sub>	3.65 <sup>+0.01</sup> <sub>-0.00</sub>	1.302 <sup>+0.002</sup> <sub>-0.001</sub>	0.19 <sup>+0.04</sup> <sub>-0.04</sub>	0.154 <sup>+0.015</sup> <sub>-0.018</sub>	-2.5 <sup>+2.3</sup> <sub>-2.0</sub>
QE-Q-22	2468	Cloud-free	N/A	CEQ	Broad	1302 <sup>+1</sup> <sub>-2</sub>	2.50 <sup>+0.00</sup> <sub>-0.00</sub>	1.111 <sup>+0.003</sup> <sub>-0.003</sub>	0.85 <sup>+0.03</sup> <sub>-0.03</sub>	0.101 <sup>+0.001</sup> <sub>-0.001</sub>	-0.4 <sup>+0.1</sup> <sub>-0.1</sub>
QE-Q-24	4753	Cloud-free	N/A	CEQ	Evo.	1210 <sup>+1</sup> <sub>-1</sub>	3.64 <sup>+0.00</sup> <sub>-0.00</sub>	1.300 <sup>+0.000</sup> <sub>-0.000</sub>	1.98 <sup>+0.01</sup> <sub>-0.01</sub>	0.100 <sup>+0.001</sup> <sub>-0.000</sub>	0.6 <sup>+0.1</sup> <sub>-0.2</sub>
Scheme (c): Hot Spots (Figure 5)											
QE-Q-21	1601	Cloud-free	Cloud-free	CEQ	Broad	1152 <sup>+3</sup> <sub>-3</sub>	2.50 <sup>+0.00</sup> <sub>-0.00</sub>	1.462 <sup>+0.007</sup> <sub>-0.007</sub>	1.80 <sup>+0.03</sup> <sub>-0.04</sub>	0.101 <sup>+0.001</sup> <sub>-0.001</sub>	-0.2 <sup>+0.1</sup> <sub>-0.1</sub>
QE-Q-23	3766	Cloud-free	Cloud-free	CEQ	Evo.	1141 <sup>+4</sup> <sub>-5</sub>	3.54 <sup>+0.00</sup> <sub>-0.00</sub>	1.479 <sup>+0.014</sup> <sub>-0.010</sub>	1.74 <sup>+0.03</sup> <sub>-0.02</sub>	0.100 <sup>+0.000</sup> <sub>-0.000</sub>	-3.0 <sup>+0.8</sup> <sub>-1.2</sub>

<sup>a</sup>Label numbers indicate the BIC ranks of retrieval runs. “QE-Q-1” corresponds to the most preferred setup among all retrieval runs that incorporate quenching and equilibrium chemistry.

<sup>b</sup>The  $\Delta\text{BIC}$  is computed by comparing the BIC of each retrieval run with that of QE-Q-1.

<sup>c</sup>“CEQ” indicates that the base pressures all cloud species are self-consistently computed based on chemical equilibrium; “Flex. MgSi” indicates that the base pressures of iron clouds are computed based on chemical equilibrium, while those of the magnesium silicate clouds are free parameters; “Flex. Both” indicates that the base pressures of all cloud species are free parameters.

<sup>d</sup>“Broad” indicates that broad priors are adopted for  $\log(g)$ ,  $R$ , and  $M$ ; “Evo.” indicates that the evolution-based priors for these parameters are adopted.

**Table 4.** Retrieved properties of 2MASS 1207 b (Quenching + Equilibrium Chemistry): Cloud Parameters

Label	$\Delta\text{BIC}$	Column 1 (Thin-cloud patches or hot spots) <sup>a</sup>					Column 2 (Thick-cloud regions or cold spots) <sup>a</sup>					
		$f_{\text{sed,MgSi}}$	$\log(X_{0,\text{MgSi}})$ (dex)	$f_{\text{sed,Fe}}$	$\log(X_{0,\text{Fe}})$ (dex)	$\xi_{\text{thin}}^a$	$f_{\text{sed,MgSi}}$	$\log(X_{0,\text{MgSi}})$ (dex)	$f_{\text{sed,Fe}}$	$\log(X_{0,\text{Fe}})$ (dex)	$\log(P_{\text{gray}})$ (dex)	$\log(\kappa_{\text{gray}})$ (dex)
Scheme (b): Patchy Clouds (Figure 5)												
QEQ-1	0	$4.54^{+2.45}_{-2.34}$	$-7.77^{+1.10}_{-1.06}$	$4.53^{+0.74}_{-0.55}$	$-4.53^{+0.11}_{-0.07}$	$8.8^{+0.2}_{-0.2} \%$	$1.20^{+0.07}_{-0.06}$	$-0.67^{+0.13}_{-0.12}$	$5.59^{+2.19}_{-2.26}$	$-4.84^{+2.38}_{-2.45}$	N/A	N/A
QEQ-2	4	$4.82^{+2.61}_{-2.55}$	$-6.58^{+2.27}_{-1.93}$	$3.14^{+0.49}_{-0.40}$	$-4.67^{+0.07}_{-0.07}$	$9.5^{+0.3}_{-0.4} \%$	$5.24^{+2.48}_{-2.54}$	$-5.11^{+2.50}_{-2.52}$	$1.48^{+0.06}_{-0.08}$	$-0.22^{+0.12}_{-0.16}$	N/A	N/A
QEQ-3	42	$4.71^{+2.58}_{-2.36}$	$-7.68^{+1.17}_{-1.19}$	$2.39^{+0.31}_{-0.26}$	$-4.23^{+0.05}_{-0.05}$	$9.1^{+0.2}_{-0.2} \%$	$1.50^{+0.09}_{-0.07}$	$-0.20^{+0.10}_{-0.12}$	$5.59^{+2.25}_{-2.38}$	$-5.00^{+2.43}_{-2.53}$	N/A	N/A
QEQ-4	89	$4.80^{+2.56}_{-2.52}$	$-7.69^{+1.23}_{-1.20}$	$1.79^{+0.52}_{-0.42}$	$-4.25^{+0.10}_{-0.09}$	$11.0^{+0.2}_{-0.3} \%$	$5.40^{+2.47}_{-2.62}$	$-5.16^{+2.59}_{-2.57}$	$5.07^{+2.52}_{-2.48}$	$-5.03^{+2.53}_{-2.53}$	$-5.5^{+0.3}_{-0.3}$	$0.90^{+0.05}_{-0.05}$
QEQ-5	92	$5.02^{+2.42}_{-2.42}$	$-7.40^{+1.31}_{-1.27}$	$1.32^{+0.26}_{-0.30}$	$-4.32^{+0.06}_{-0.08}$	$11.4^{+0.2}_{-0.2} \%$	$4.82^{+2.42}_{-2.32}$	$-4.85^{+2.33}_{-2.40}$	$5.14^{+2.37}_{-2.34}$	$-4.96^{+2.36}_{-2.39}$	$-5.3^{+0.3}_{-0.3}$	$0.88^{+0.06}_{-0.05}$
QEQ-10	333	$2.76^{+0.72}_{-0.57}$	$-2.85^{+0.23}_{-0.20}$	$9.93^{+0.03}_{-0.04}$	$-0.45^{+0.13}_{-0.15}$	$12.4^{+0.3}_{-0.3} \%$	$5.12^{+2.09}_{-2.17}$	$-4.42^{+2.15}_{-2.30}$	$1.52^{+0.03}_{-0.03}$	$-0.13^{+0.06}_{-0.09}$	N/A	N/A
Scheme (d): Patchy Clouds + Hot Spots (Figure 5)												
QEQ-6	109	$4.50^{+2.46}_{-2.24}$	$-7.41^{+1.35}_{-1.31}$	$2.90^{+0.63}_{-0.54}$	$-4.30^{+0.12}_{-0.12}$	$12.8^{+0.7}_{-0.7} \%$	$4.95^{+2.37}_{-2.30}$	$-4.80^{+2.30}_{-2.32}$	$0.11^{+0.05}_{-0.03}$	$-0.95^{+0.13}_{-0.10}$	N/A	N/A
QEQ-7	123	$5.16^{+2.20}_{-2.26}$	$-7.34^{+1.16}_{-1.18}$	$7.95^{+0.94}_{-1.07}$	$-4.17^{+0.06}_{-0.07}$	$11.6^{+0.4}_{-0.4} \%$	$4.47^{+2.26}_{-2.05}$	$-5.25^{+2.21}_{-2.14}$	$0.13^{+0.04}_{-0.03}$	$-0.69^{+0.16}_{-0.10}$	N/A	N/A
QEQ-8	165	$3.92^{+2.27}_{-2.01}$	$-7.52^{+1.08}_{-1.05}$	$1.39^{+0.32}_{-0.21}$	$-4.55^{+0.09}_{-0.06}$	$23.9^{+0.5}_{-0.6} \%$	$5.13^{+2.24}_{-2.27}$	$-4.86^{+2.26}_{-2.29}$	$4.59^{+2.23}_{-2.18}$	$-5.70^{+2.22}_{-2.09}$	$-4.7^{+0.1}_{-0.1}$	$7.25^{+0.81}_{-0.81}$
QEQ-9	169	$3.74^{+2.07}_{-1.90}$	$-7.35^{+1.09}_{-1.12}$	$1.70^{+0.34}_{-0.20}$	$-4.19^{+0.07}_{-0.05}$	$11.1^{+0.2}_{-0.3} \%$	$5.09^{+2.22}_{-2.23}$	$-5.55^{+2.12}_{-2.06}$	$5.26^{+2.15}_{-2.11}$	$-4.69^{+2.17}_{-2.33}$	$-4.9^{+0.4}_{-0.4}$	$0.95^{+0.19}_{-0.17}$
QEQ-11	532	$9.55^{+0.20}_{-0.21}$	$-0.03^{+0.01}_{-0.02}$	$4.58^{+1.99}_{-1.99}$	$-5.24^{+1.87}_{-1.94}$	$28.3^{+0.4}_{-0.4} \%$	$1.38^{+0.07}_{-0.06}$	$-0.70^{+0.10}_{-0.09}$	$6.15^{+1.86}_{-2.10}$	$-3.85^{+1.80}_{-1.93}$	N/A	N/A
QEQ-12	586	$1.80^{+0.02}_{-0.02}$	$-5.43^{+0.06}_{-0.06}$	$9.89^{+0.05}_{-0.07}$	$-0.66^{+0.11}_{-0.10}$	$41.0^{+0.5}_{-0.5} \%$	$4.98^{+2.18}_{-2.15}$	$-5.83^{+2.14}_{-1.91}$	$5.44^{+2.05}_{-2.08}$	$-5.49^{+2.16}_{-2.12}$	$-4.6^{+0.0}_{-0.0}$	$7.42^{+0.80}_{-0.98}$
QEQ-13	589	$0.99^{+0.09}_{-0.06}$	$-0.89^{+0.08}_{-0.07}$	$5.13^{+2.18}_{-2.17}$	$-4.80^{+2.23}_{-2.26}$	$19.7^{+0.7}_{-0.5} \%$	$9.43^{+0.31}_{-0.41}$	$-1.12^{+0.08}_{-0.07}$	$9.22^{+0.40}_{-0.52}$	$-0.50^{+0.14}_{-0.14}$	N/A	N/A
QEQ-18	907	$4.50^{+0.34}_{-0.36}$	$-0.07^{+0.03}_{-0.04}$	$6.36^{+1.79}_{-2.17}$	$-5.15^{+2.21}_{-2.17}$	$35.9^{+0.5}_{-0.5} \%$	$5.23^{+2.20}_{-2.23}$	$-5.15^{+2.33}_{-2.25}$	$0.35^{+0.13}_{-0.11}$	$-0.92^{+0.43}_{-0.48}$	$-4.9^{+0.1}_{-0.1}$	$3.55^{+0.15}_{-0.15}$
Scheme (a): Homogeneous Atmosphere (Figure 5)												
QEQ-14	610	$0.08^{+0.00}_{-0.00}$	$-4.48^{+0.01}_{-0.01}$	$6.26^{+0.11}_{-0.11}$	$-0.10^{+0.04}_{-0.05}$	100 %	N/A	N/A	N/A	N/A	N/A	N/A
QEQ-15	622	$1.30^{+0.11}_{-0.14}$	$-0.10^{+0.04}_{-0.05}$	$0.88^{+0.05}_{-0.05}$	$-0.36^{+0.06}_{-0.05}$	100 %	N/A	N/A	N/A	N/A	N/A	N/A
QEQ-16	693	$0.14^{+0.00}_{-0.00}$	$-2.47^{+0.01}_{-0.01}$	$5.78^{+2.44}_{-2.81}$	$-6.06^{+2.27}_{-2.21}$	100 %	N/A	N/A	N/A	N/A	N/A	N/A
QEQ-17	753	$4.99^{+0.58}_{-0.46}$	$-1.82^{+0.09}_{-0.07}$	$1.57^{+0.04}_{-0.04}$	$-2.13^{+0.03}_{-0.03}$	100 %	N/A	N/A	N/A	N/A	N/A	N/A
QEQ-19	963	$0.09^{+0.00}_{-0.00}$	$-3.03^{+0.02}_{-0.01}$	$4.26^{+0.12}_{-0.12}$	$-0.44^{+0.21}_{-0.21}$	100 %	N/A	N/A	N/A	N/A	N/A	N/A
QEQ-20	984	$0.04^{+0.00}_{-0.00}$	$-2.90^{+0.01}_{-0.01}$	$4.14^{+0.15}_{-0.29}$	$-0.11^{+0.06}_{-0.08}$	100 %	N/A	N/A	N/A	N/A	N/A	N/A
QEQ-22	2468	N/A	N/A	N/A	N/A	100 %	N/A	N/A	N/A	N/A	N/A	N/A
QEQ-24	4753	N/A	N/A	N/A	N/A	100 %	N/A	N/A	N/A	N/A	N/A	N/A
Scheme (c): Hot Spots (Figure 5)												
QEQ-21	1601	N/A	N/A	N/A	N/A	$28.5^{+0.4}_{-0.4} \%$	N/A	N/A	N/A	N/A	N/A	N/A
QEQ-23	3766	N/A	N/A	N/A	N/A	$42.0^{+16.5}_{-1.4} \%$	N/A	N/A	N/A	N/A	N/A	N/A

<sup>a</sup>For schemes with patchy clouds or a combination of patchy clouds and hot spots, the column 1 represents the thin-cloud patches and the column 2 represents the thick-cloud regions; the parameter  $\xi_{\text{thin}}$  describes the coverage of thin-cloud patches. In the hot-spot scheme, column 1 represents the atmospheric column with an overall hotter thermal structure (i.e., hot spots), while the column 2 represents the cold spots; the parameter  $\xi_{\text{thin}}$  describes the coverage of hot spots.

and label other, less favored models as QEQ- $x$ , where  $x$  denotes their ranks by BIC values. A larger  $x$  corresponds to a higher  $\Delta\text{BIC}$  and a less preferred model. We compare the observations with the fitted model spectra of QEQ-1 in Figure 6 and present the posterior distributions of key retrieved parameters in Figure 7.<sup>6</sup>

In the next section (Section 7), we provide a detailed discussion of these retrieval results, with a particular focus on the most preferred retrieval model, QEQ-1. In Section 7.1, we discuss the inhomogeneous atmosphere of 2MASS 1207 b, as consistently indicated by QEQ-1 and several other moderately preferred retrieval runs, and compare these findings with atmospheric properties of Jupiter. In Section 7.2, we explore unique spectral features of 2MASS 1207 b that have not been fully explained in previous studies. These features include weak CO absorption over 4.4–5.2  $\mu\text{m}$  and the absence of 3.3  $\mu\text{m}$  CH<sub>4</sub> absorption, which we demonstrate can be understood within the context of 2MASS 1207 b’s inhomogeneous atmosphere, as revealed by our retrieval analyses. Section 7.3 discusses that the presence of disequilibrium chemistry in the atmosphere of 2MASS 1207 b cannot be constrained via CH<sub>4</sub> quenching as commonly performed for colder L, T, and Y dwarfs, given this object’s hot and CO-dominant atmosphere. We further place the results of QEQ-1 in the context of 2MASS 1207 b’s observed photometric variabilities in Section 7.4, and discuss the atmospheric [M/H] and C/O of this planetary-mass companion based on all retrieval runs in Section 7.5. Finally, we comment on the results of retrievals with various atmospheric assumptions in Section 7.6,

## 7. DISCUSSION

### 7.1. The Jupiter-like Inhomogeneous Atmosphere of 2MASS 1207 b: 91% thick clouds with 9% thin-cloud patches

Figure 6 presents the fitted model spectra of QEQ-1, the most favored model for interpreting the JWST/NIRSpec spectrum of 2MASS 1207 b in our retrieval analyses. As summarized in Table 3, this model corresponds to the patchy cloud scheme illustrated in Figure 5 (b), incorporated with evolution-based priors for surface gravity, radius, and mass. QEQ-1 yields an effective temperature of  $T_{\text{eff}} = 1174_{-3}^{+4}$  K, a surface gravity of  $\log(g) = 3.62_{-0.02}^{+0.03}$  dex, a radius of  $R = 1.399_{-0.010}^{+0.008} R_{\text{Jup}}$ , a solar-like atmospheric metallicity of  $[M/H] = -0.05 \pm 0.03$  dex, and an atmospheric C/O ratio of  $0.440 \pm 0.012$  (see Section 7.5 for further discussions of atmospheric compositions).

Notably, QEQ-1 suggests that the atmosphere of 2MASS 1207 b contains patchy forsterite and iron clouds with a significant contrast in cloud coverage between two atmospheric columns (Tables 3–4) that share the same thermal structure, detailed as below:

- **Thin-cloud patches (~9% coverage).** About 9% of the atmosphere has thin iron clouds with a mass fraction of  $\log(X_{0,\text{Fe}}) = -4.53_{-0.08}^{+0.14}$  at the base pressure and an intermediate sedimentation efficiency of  $f_{\text{sed}} = 4.5_{-0.6}^{+0.7}$ . The forsterite cloud content is significantly lower, with a mass fraction of  $\log(X_{0,\text{Mg}_2\text{SiO}_4}) = -7.8 \pm 1.1$  at the base pressure. As shown in Figure 6, the emergent spectrum from these thin-cloud patches resembles that of a young L dwarf with a triangular *H*-band shape (e.g., [Looper et al. 2007](#); [Allers & Liu 2013](#)) which aligns with the retrieved low surface gravity of  $\log(g) = 3.62_{-0.02}^{+0.02}$  dex. As shown in Figure 8, the contribution function of this atmospheric column spans pressures from  $10^{-2}$  bar to 1 bar, peaking at around 0.2 bar, meaning that the corresponding photosphere has a brightness temperature of 1600–1700 K.
- **Thick-cloud regions (~91% coverage).** The remaining 91% atmosphere is dominated by vertically extended Mg<sub>2</sub>SiO<sub>4</sub> and iron clouds, with high mass fractions at the base pressures and low sedimentation efficiencies. The significant cloud opacity results in a contribution function distributed in the upper atmosphere, spanning pressures from  $2 \times 10^{-4}$  bar to  $2 \times 10^{-2}$  bar, meaning that the corresponding photosphere has a brightness temperature of 1100–1200 K (Figure 8). This leads to a blackbody-like emergent spectrum with flux peaking at  $\sim 2.5 \mu\text{m}$  (Figure 6).

Interestingly, the combination of thin-cloud patches with L-dwarf-like spectra and thick-cloud regions with blackbody-like spectra, as suggested by QEQ-1, is consistently supported by nearly all QEQ retrievals that include clouds and inhomogeneous atmospheres. In particular, when a gray cloud layer is incorporated into one of the atmospheric columns, the retrieved models indicate that the thick-cloud regions are characterized by a high-altitude gray cloud layer at low pressures around  $10^{-5}$  bar (QEQ-4, 5, 8, 9, 12, 18). Additionally, retrieval runs with the seven lowest BIC values (QEQ-1 to QEQ-7) indicate scenarios where 87%–91% of 2MASS 1207 b’s atmosphere is covered by thick clouds, with 9%–13% covered by thin-cloud patches (Tables 3–4). These findings align with the results of [Apai et al. \(2013\)](#), who suggested that the variability of brown dwarfs near the L/T transition is better explained by inhomogeneous atmospheres with a mixture of thin-cloud and thick-cloud patches rather than by a simple combination of clouds and purely cloud-free holes.

<sup>6</sup> The best-fit model spectra and the fitted T-P profiles of all individual retrieval runs, as well as the QEQ-1 parameter posteriors, are accessible through this Zenodo repository, <https://doi.org/10.5281/zenodo.15654303>

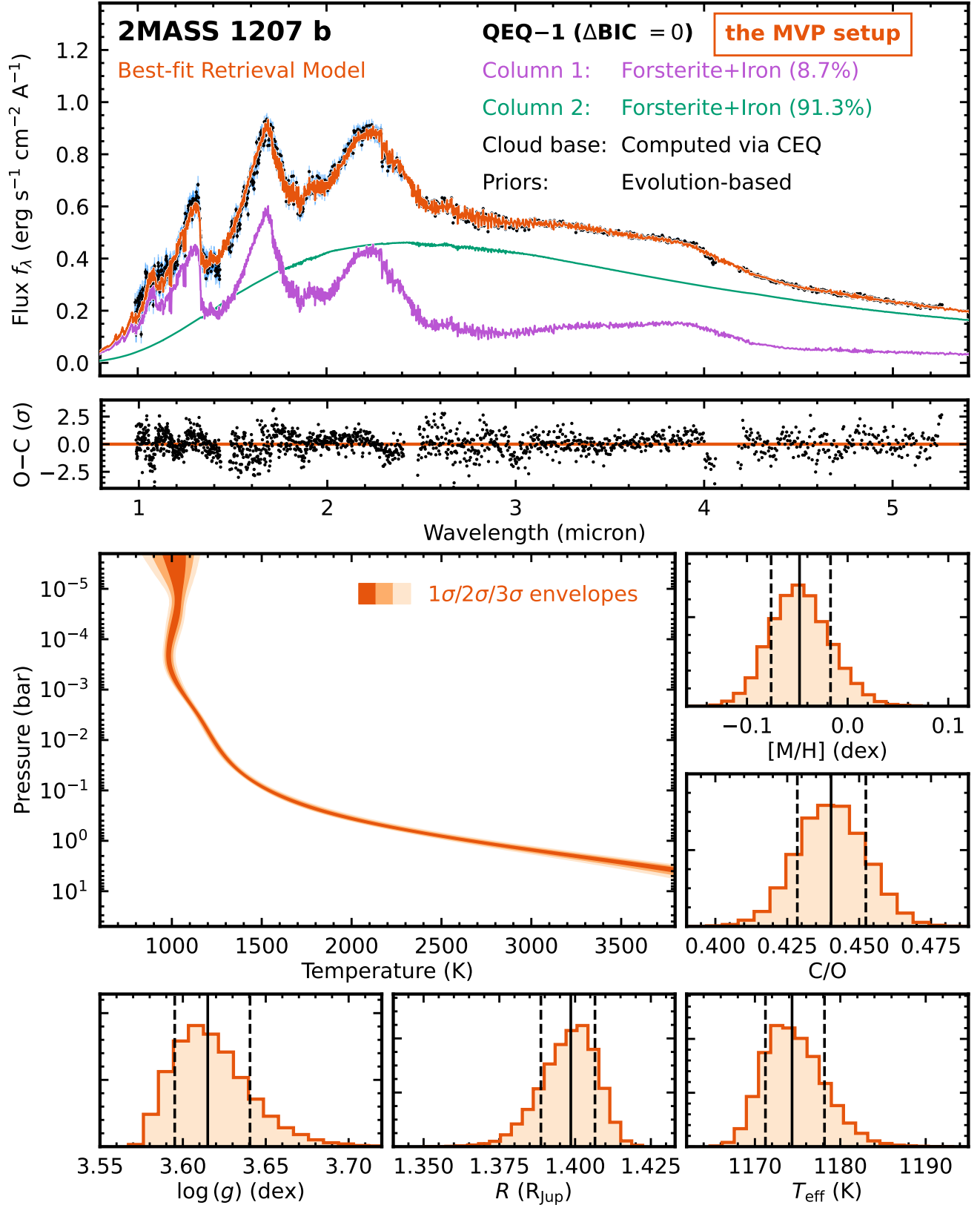


**Figure 6.** Results of our most preferred retrieval setup, QEQ-1 (see Tables 3–4 and discussions in Section 7.1), which has the lowest BIC value. The top panel compares the observed JWST/NIRSpec spectrum of 2MASS 1207 b (black circles) with the best-fit spectrum from QEQ-1 (orange). The emergent spectra from each atmospheric column are plotted in purple and green, with fluxes scaled by their corresponding coverage fractions. The blue error bars ( $\sigma$ ) represent the total error budget, where  $\sigma = \sqrt{\sigma_{\text{obs}}^2 + b_{\text{chunk}}^2}$ , with  $\sigma_{\text{obs}}$  as the observed flux uncertainty and  $b_{\text{chunk}}$  as the fitted hyper-parameter (explained in Section 5.5). The second panel from the top shows the residual spectrum between the observed and best-fit spectra, scaled by  $\sigma$ . The middle-left panel presents the confidence intervals for the retrieved T-P profiles. The remaining panels present the posteriors of key parameters, with median values and confidence intervals summarized in Table 3.

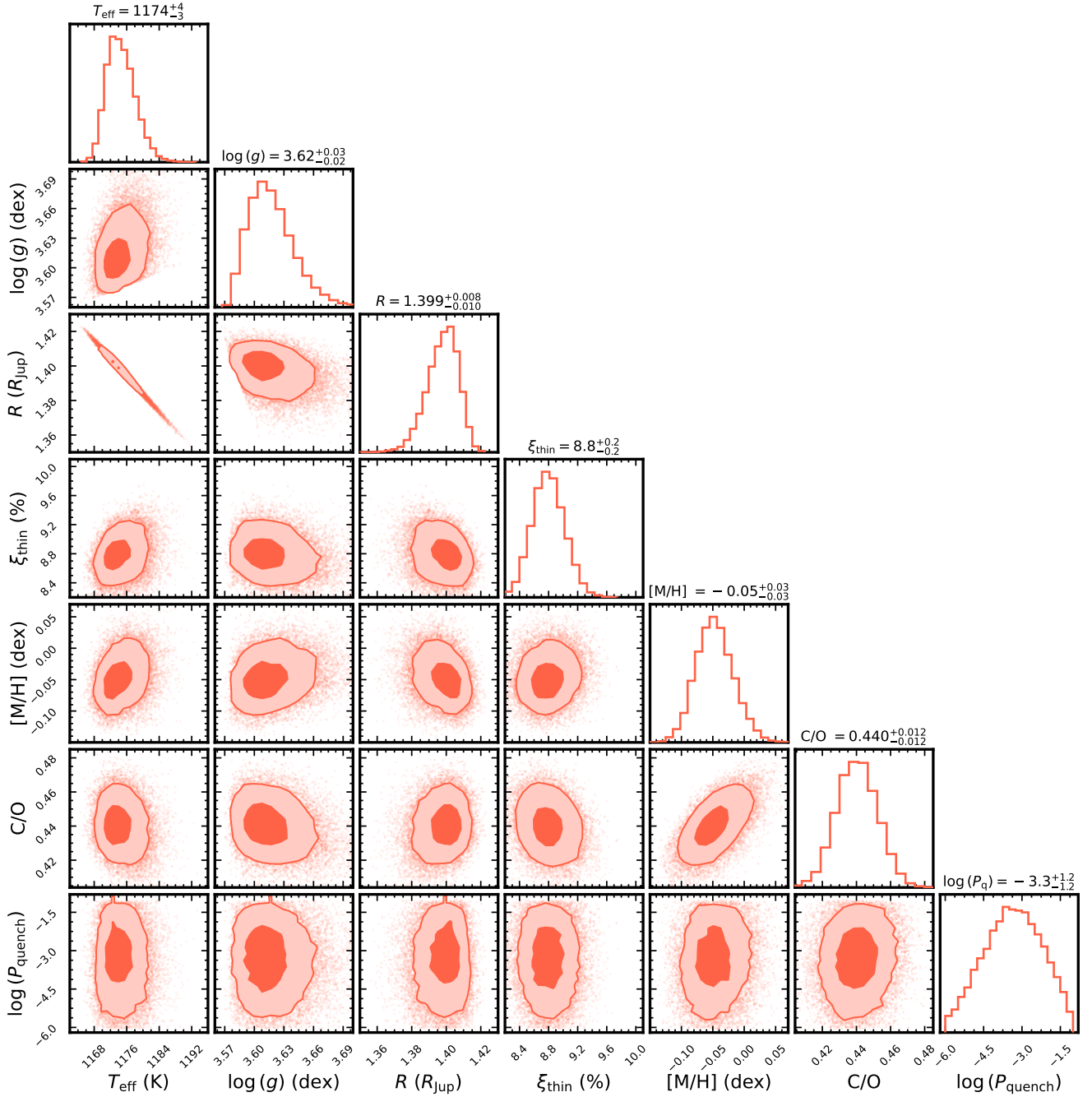


**Figure 7.** Corner plot for the inferred parameters of 2MASS 1207 b based on the most preferred retrieval setup, QE<sub>Q</sub>-1. The  $1\sigma$  and  $2\sigma$  confidence intervals are highlighted for each parameter.

The inhomogeneous atmosphere of 2MASS 1207 b is analogous to that of Jupiter, which exhibits a banded structure of zones and belts (e.g., Pirraglia et al. 1981; Belton et al. 1996; Hockey 1999; Fletcher et al. 2020, 2021). Zones are cloudy regions that strongly reflect sunlight, while belts are thin-cloud regions that appear darker in reflected light. Although these dark belts occupy only about 1% of Jupiter’s atmosphere (e.g., Westphal 1969; Orton et al. 1996), their ther-

mal emission dominates Jupiter’s spectrum near  $5\ \mu\text{m}$ .<sup>7</sup> Our QE<sub>Q</sub>-1 retrieval suggests that 2MASS 1207 b has thin-cloud

<sup>7</sup> These dark regions, often referred to as “ $5\text{-}\mu\text{m}$  hot spots” in the literature, are relatively cloud-free areas that probe deeper, hotter atmospheric layers. This concept of hot spots aligns with the scheme (b) “patchy clouds” in our atmospheric inhomogeneity framework (Section 5.4 and Figure 5) and differs from the scheme (c) “cloud-free hot spots” in our framework; the latter involves two cloud-free columns with different T-P profiles.

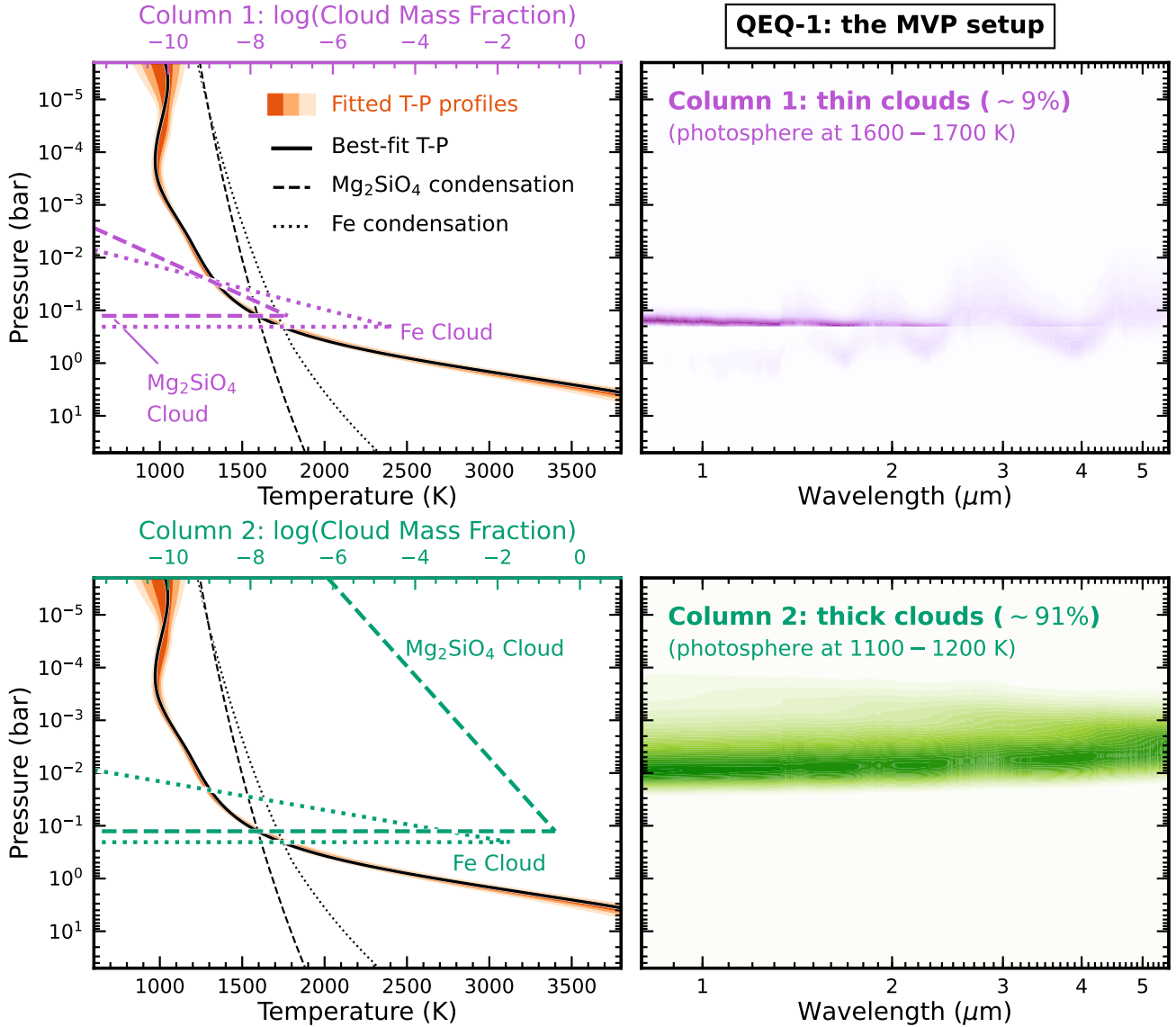


**Figure 8.** *Top Left:* Retrieved T-P profiles from the QE-1 setup, with  $1\sigma/2\sigma/3\sigma$  confidence intervals shown in orange. The solid black line represents the best-fit T-P profile. Condensation curves of  $\text{Mg}_2\text{SiO}_4$  and Fe, calculated using the maximum-likelihood  $[\text{M}/\text{H}]$  and  $\text{C}/\text{O}$  values, are shown by dashed and dotted lines, respectively. The best-fit cloud mass fraction profiles for the first column (thin-cloud patches covering about 9% of 2MASS 1207 b’s atmosphere) are plotted in purple, with values indicated on the upper x-axis. *Top right:* Maximum-likelihood contribution function of the thin-cloud patches. *Bottom:* These two panels show the best-fit cloud content and contribution function for the second column (thick-cloud regions covering about 91% of the atmosphere), following the same format as the top two panels.

patches covering 9% of the atmosphere, with photospheric temperatures of 1600–1700 K, and thick-cloud regions covering 91%, with slightly lower photospheric temperatures of 1100–1200 K. These features resemble Jupiter’s belts and zones, respectively. As shown in Figure 6, the thin-cloud patches produce much brighter or comparable fluxes than the thick-cloud regions at wavelengths below  $2.3 \mu\text{m}$ . Consequently, the near-infrared spectral features of 2MASS 1207 b in  $Y$ ,  $J$ , and  $H$  bands predominantly arise from these thin-

cloud patches, while this object’s unusually red spectral slope is attributed to the thick clouds.

The thick clouds and potential high-altitude gray cloud content of 2MASS 1207 b, as suggested by our retrievals, may be contributed by this object’s ongoing accretion (Luhman et al. 2023; Marleau et al. 2024; Manjavacas et al. 2024) of dust and gas from the circumstellar disk of 2MASS 1207 A (e.g., Ricci et al. 2017) which has an estimated dust mass of  $\sim 0.1 M_{\oplus}$  (e.g., Mohanty et al. 2013; Ricci et al. 2017). Ad-

ditionally, 2MASS 1207 b may host its own disk, though if present, it likely has a low dust mass below  $1 M_{\text{moon}}$  (Ricci et al. 2017). Similar to events that have influenced Jupiter — such as the impacts of Comet Shoemaker-Levy 9 (e.g., Hammel et al. 1995) — such processes may also influence the atmospheric evolution of 2MASS 1207 b. Follow-up studies similar to Madurowicz et al. (2023) would be valuable in assessing whether accretion activity can match the observed cloud properties of 2MASS 1207 b, as well as the present-day atmospheric compositions of both 2MASS 1207 A and b. Furthermore, future retrieval studies that incorporate both NIRSpec and MIRI spectra of 2MASS 1207 b will be crucial for more precisely constraining the type and amount of silicate clouds in its atmosphere and also the presence and properties of this object’s circumsecondary disk, which, if present, could contribute to the flux at MIRI wavelengths (Luhman et al. 2023).

### 7.2. Weak CO and Absent CH<sub>4</sub> absorption: Net Effects of Patchy Thick Clouds and a Hot Thermal Structure

The JWST/NIRSpec spectrum of 2MASS 1207 b offers unprecedented insights into this object’s atmosphere, surpassing previous ground-based near-infrared ( $1 - 2.5 \mu\text{m}$ ) spectroscopy (e.g., Chauvin et al. 2004; Mohanty et al. 2007; Patience et al. 2010), and revealing peculiar features that remain unexplained (Luhman et al. 2023; Manjavacas et al. 2024). Notably, the  $2.5 - 5.0 \mu\text{m}$  spectrum of 2MASS 1207 b differs significantly from that of VHS J125601.92–125723.9 b (VHS 1256 b; Gauza et al. 2015; Miles et al. 2023), despite similarities in their  $1 - 2.5 \mu\text{m}$  spectra (Figure 9; see also Figure 6 of Luhman et al. 2023). Specifically, 2MASS 1207 b exhibits much weaker CO absorption in the  $4.4 - 5.2 \mu\text{m}$  compared to VHS 1256 b. Also, the prominent  $3.3 \mu\text{m}$  CH<sub>4</sub> absorption seen in VHS 1256 b is absent in 2MASS 1207 b’s NIRSpec spectrum.

These unique features of 2MASS 1207 b have not been explained by forward modeling efforts. When fitting the ATMO and BT-Settl grid models (Allard et al. 2003, 2012; Tremblin et al. 2015, 2017; Petrus et al. 2024) to 2MASS 1207 b’s NIRSpec spectrum, both Luhman et al. (2023) and Manjavacas et al. (2024) found that these models overpredict the strengths of CH<sub>4</sub> and CO absorption compared to the observations. As both studies acknowledged, disequilibrium chemistry can weaken CH<sub>4</sub> absorption but typically strengthens CO absorption, which conflicts with the observed weak CO features. Luhman et al. (2023) suggested that the weaker CO absorption in 2MASS 1207 b compared to its slightly older counterpart, VHS 1256 b ( $\sim 140$  Myr; Dupuy et al. 2023), indicates that certain atmospheric property, such as thermal structure and cloud thickness, may vary with age. Similarly, Manjavacas et al. (2024) attributed the unique

spectral features of 2MASS 1207 b to its lower surface gravity (or younger age) relative to VHS 1256 b. However, detailed and quantitative explanations for the distinctive CO and CH<sub>4</sub> features of 2MASS 1207 b remain needed.

As detailed in the following subsections, our retrieval analysis shows that the weak CO absorption observed in 2MASS1207b can be attributed to its patchy clouds (Section 7.2.1). Furthermore, the absence of CH<sub>4</sub> absorption is consistent with this object’s relatively hot atmospheric thermal structure (Section 7.2.2).

#### 7.2.1. Weak CO absorption due to patchy cloud veiling effects

As discussed in Section 7.1, the atmosphere of 2MASS 1207 b is characterized by thick-cloud regions and thin-cloud patches. While the thick clouds produce a nearly featureless blackbody-like spectrum, the emergent flux from the thin-cloud patches exhibits prominent absorption features of H<sub>2</sub>O, CO, Na I, K I, FeH, and VO (Figure 6). As shown in Figure 9, the  $2.5 - 5.0 \mu\text{m}$  spectrum from the thin-cloud patches of 2MASS 1207 b closely resembles that of VHS 1256 b, with similar H<sub>2</sub>O and CO absorption bands. However, these absorption features are diluted in the combined emergent spectrum due to (1) the limited 9% coverage of thin clouds and (2) the blackbody-like thermal emission from the thick clouds, which is 2–5 times brighter than the fluxes from thin-cloud patches across  $2.5 - 5.0 \mu\text{m}$  (Figure 6). As a result, the observed weak CO absorption in 2MASS 1207 b is primarily a result of veiling by the patchy thick clouds that dominate its atmosphere.

#### 7.2.2. Absent CH<sub>4</sub> absorption due to the hot atmospheric thermal structure

The absence of  $3.3 \mu\text{m}$  CH<sub>4</sub> absorption in 2MASS1207b cannot be explained by cloud veiling effects, as discussed in Section 7.2.1, because this feature is not predicted by our retrieved spectrum from either thin-cloud patches or thick-cloud regions. Instead, we attribute the lack of CH<sub>4</sub> absorption to this object’s relatively hot atmospheric thermal structure.

In Figure 10, we compare the retrieved T-P profile with a critical curve corresponding to an equilibrium situation where the volume mixing ratios of CH<sub>4</sub> and CO are equal. This curve,  $\log(P) = 5.05 - 5807.5/T + 0.5 \times [M/H]$ , was derived by Fortney et al. (2020). Deviations from this curve lead to either a decrease in CH<sub>4</sub> abundance at higher temperatures and lower pressures, or a decrease in CO abundance at lower temperatures and higher pressures. Objects with thermal structures hotter than this CO–CH<sub>4</sub> transition curve tend to exhibit weak or absent  $3.3 \mu\text{m}$  CH<sub>4</sub> absorption, while cooler objects display stronger CH<sub>4</sub> absorption. We demonstrate this effect in Figures 11–12 using the Sonora Diamondback atmospheric models (Morley et al. 2024).

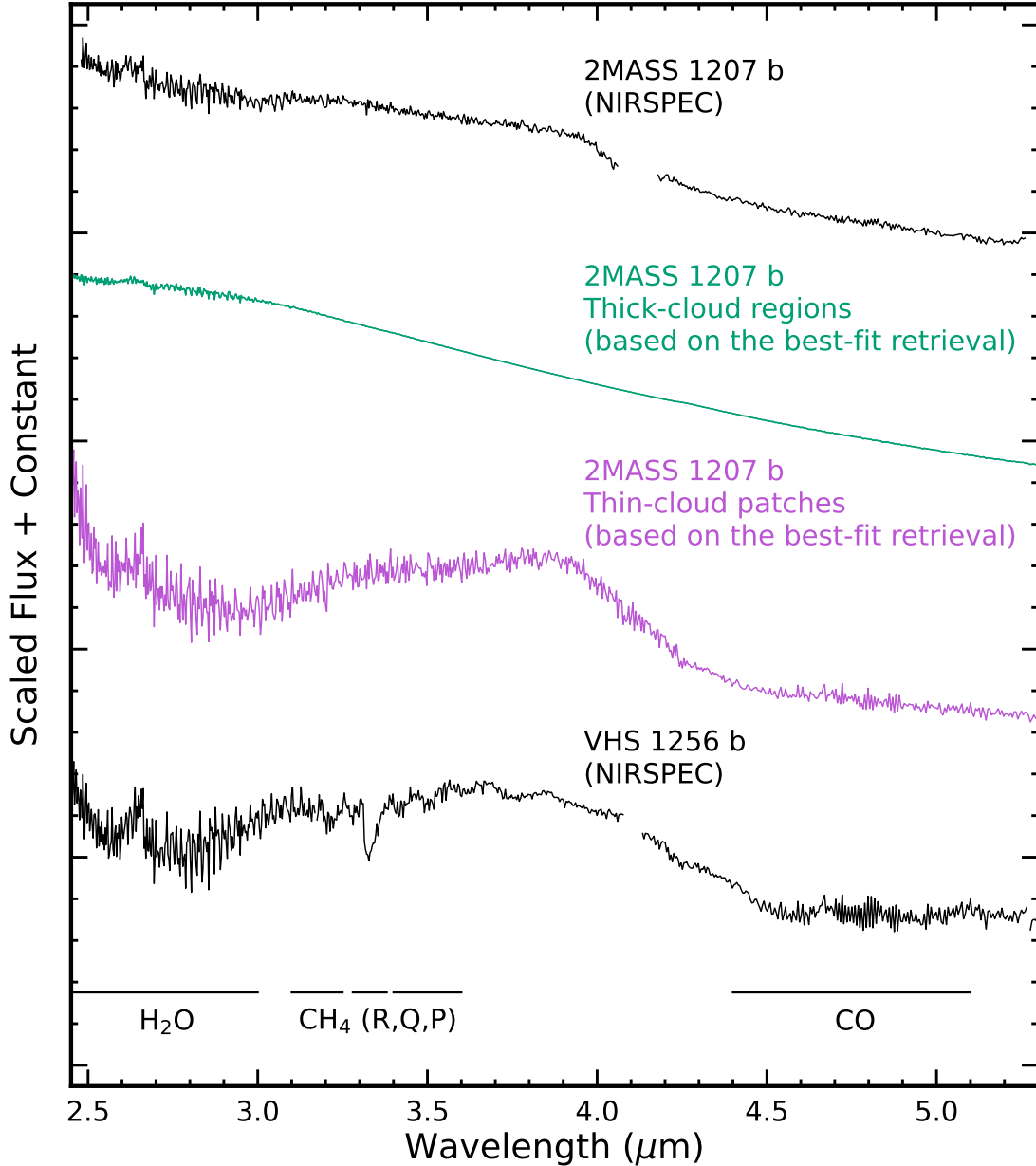


**Figure 9.** The top three spectra show the observed JWST/NIRSpec data of 2MASS 1207 b (black), as well as the best-fit retrieval model spectra emerging from the thick-cloud regions (green) and thin-cloud patches (purple) based on the  $\text{QEQ-1}$  setup. The JWST/NIRSpec spectrum of VHS 1256 b (Miles et al. 2023) is shown at the bottom. All spectra are plotted at a spectral resolution of  $R = 1000$ . Key molecular absorption features are labeled.

The onset of  $\text{CH}_4$  absorption occurs when an object’s 3 – 4  $\mu\text{m}$  photosphere cools sufficiently to approach the  $\text{CH}_4$ –CO transition curve. Our analysis reveals that this “ $\text{CH}_4$  onset” depends on several physical parameters, including  $T_{\text{eff}}$ ,  $[M/H]$ ,  $f_{\text{sed}}$ , and  $\log(g)$ , as summarized below:

- Effective temperature. As shown in Figure 11,  $\text{CH}_4$  absorption begins at  $T_{\text{eff}} \approx 1600$  K for objects with  $\log(g) = 4.5$  dex,  $[M/H] = 0$  dex, and  $f_{\text{sed}} = 2$ . This critical  $T_{\text{eff}}$  corresponds to a spectral type of  $\sim\text{L4}$  (e.g.,

Filippazzo et al. 2015), consistent with the findings of Noll et al. (2000), who observed  $\text{CH}_4$  absorption in L5 and L7 dwarfs but not in an L3 dwarf with a hotter effective temperature .

- Metallicity. As shown in Figure 11, higher metallicity shifts the photosphere to lower pressures, moving it farther from the CO– $\text{CH}_4$  transition curve. For objects with  $T_{\text{eff}} = 1400$  K,  $\log(g) = 4.5$  dex, and  $f_{\text{sed}} = 2$ , the strength of the 3.3  $\mu\text{m}$   $\text{CH}_4$  absorption increases

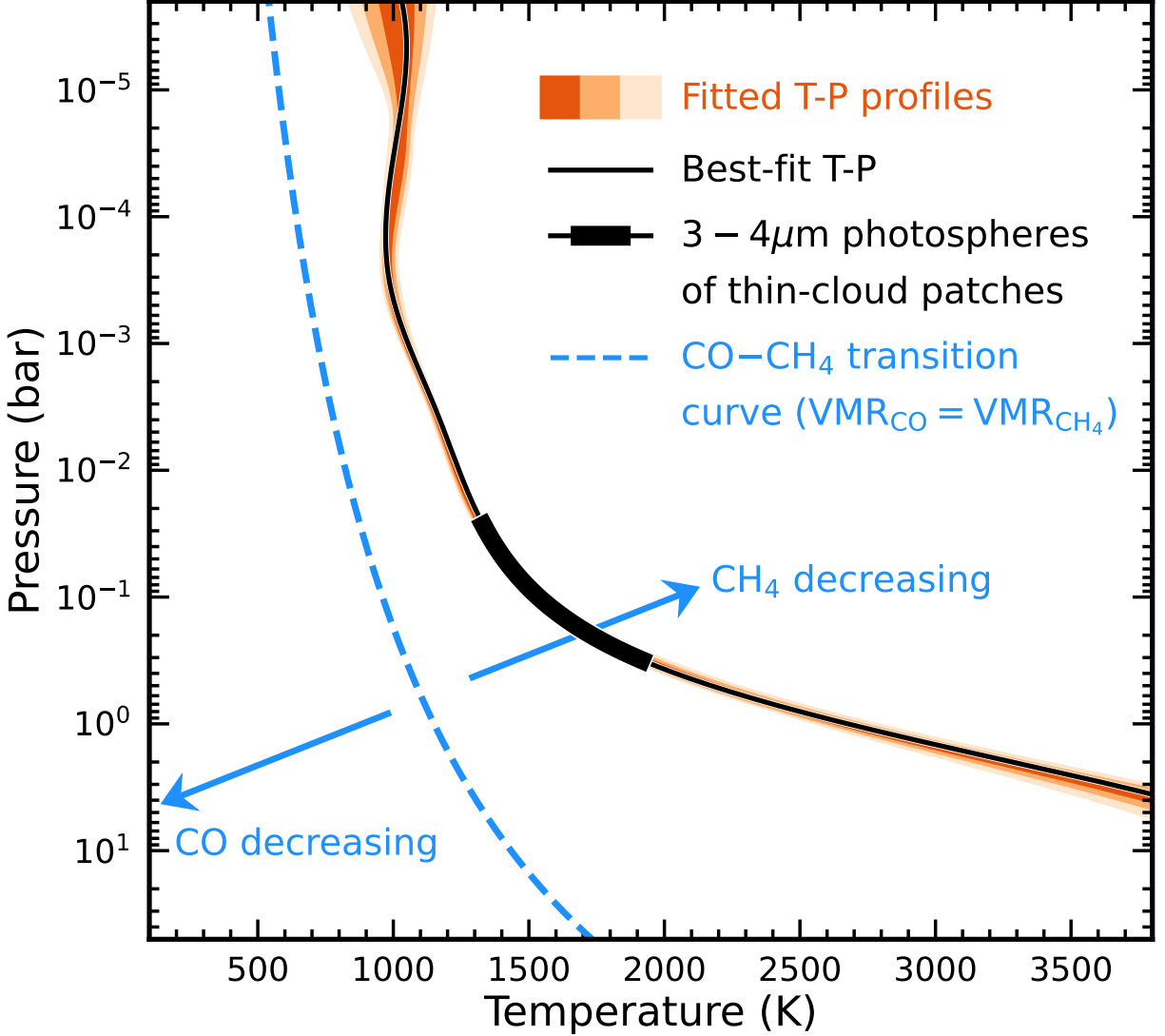


**Figure 10.** Retrieved T-P profiles from the QEQ-1 setup, with  $1\sigma$ ,  $2\sigma$ , and  $3\sigma$  confidence intervals shown in orange. The best-fit T-P profile is indicated by the solid black line, with the  $3-4\ \mu\text{m}$  photosphere of thin-cloud patches highlighted by a thicker line. The CO-CH<sub>4</sub> transition curve for solar metallicity, from (Fortney et al. 2020), is overlaid as a dashed blue line; along this line, the CO and CH<sub>4</sub> have equal volume mixing ratios. A thermal structure with hotter temperatures and/or lower pressures than this transition curve would have a decreased CH<sub>4</sub> abundance, while a cooler and/or higher-pressure thermal structure would have a decreased CO abundance.

as  $[M/H]$  decreases from  $+0.5$  dex to  $-0.5$  dex (Figure 11). This trend suggests that CH<sub>4</sub> onset occurs at a  $[M/H]$  slightly above  $+0.5$  dex for this particular parameter set.

- Sedimentation efficiency. Figure 12 shows that more cloudy atmospheres (e.g.,  $f_{\text{sed}} = 1$ ) have  $3-4\ \mu\text{m}$  photospheres farther from the CO-CH<sub>4</sub> transition curve compared to less cloudy objects (e.g.,  $f_{\text{sed}} = 8$ ). For  $T_{\text{eff}} = 1400$  K,  $\log(g) = 4.5$  dex, and  $[M/H] = 0$  dex, the CH<sub>4</sub> onset occurs at  $f_{\text{sed}} \sim 2$ .
- Surface gravity. The relationship between CH<sub>4</sub> onset and  $\log(g)$  is nonlinear. As shown in Figure 12, for

$T_{\text{eff}} = 1200$  K,  $[M/H] = 0$  dex, and  $f_{\text{sed}} = 1$ , objects with  $\log(g) = 3.5$  dex show similar CH<sub>4</sub> absorption strength to those with  $\log(g) = 5.5$  dex, as their  $3-4\ \mu\text{m}$  photospheres are similarly distant from the CO-CH<sub>4</sub> transition curve. However, these models exhibit weaker CH<sub>4</sub> absorption at  $3.3\ \mu\text{m}$  compared to those with  $\log(g) = 4.0-4.5$  dex, whose T-P profiles closely approach the CO-CH<sub>4</sub> transition curve.

In summary, the onset of CH<sub>4</sub> absorption is governed by parameters that significantly alter an object's thermal structure. The presence of vertical mixing (e.g., Zahnle & Marley 2014)

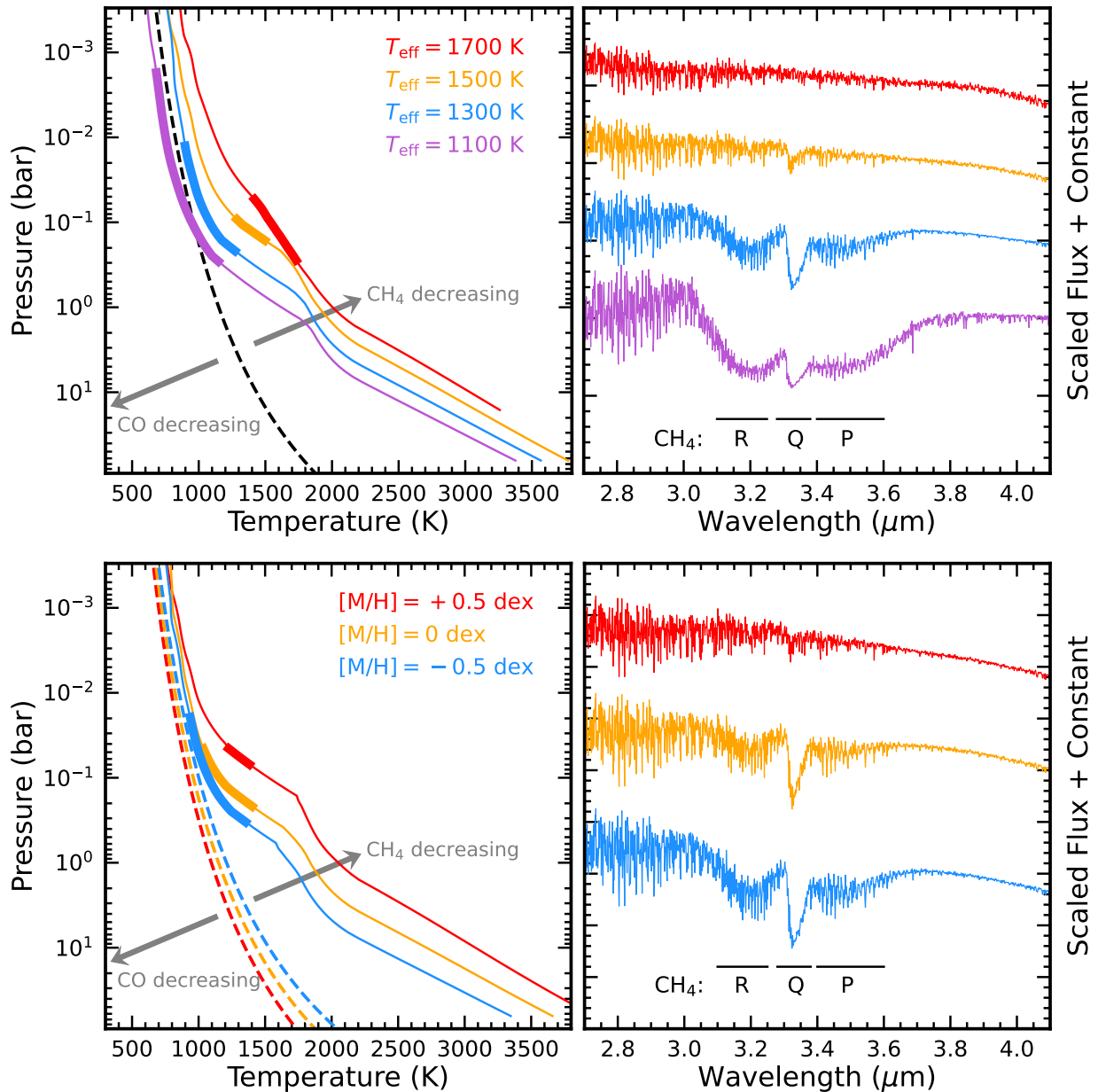


**Figure 11.** *Top:* The left panel shows T-P profiles from the *Sonora Diamondback* models with varying effective temperatures:  $T_{\text{eff}} = 1700$  K (red), 1500 K (orange), 1300 K (blue), and 1100 K (purple). All models have  $\log(g) = 4.5$  dex,  $[M/H] = 0$  dex, and  $f_{\text{sed}} = 2$ . The  $3 - 4 \mu\text{m}$  photosphere of each model is highlighted with a thick line. The CO–CH<sub>4</sub> transition curve (see Figure 10) is shown as a dashed line. The right panel presents the corresponding spectra, with CH<sub>4</sub> absorption features (R, Q, and P branches) labeled. *Bottom:* These two panels follow the same format as the top panels but present the T-P profiles and spectra for models with different  $[M/H]$  values: +0.5 dex (red), 0 dex (orange), and –0.5 dex (blue). All models have  $T_{\text{eff}} = 1400$  K,  $\log(g) = 4.5$  dex, and  $f_{\text{sed}} = 2$ .

and any variations in the atmospheric adiabatic index (e.g., Tremblin et al. 2016), would also impact the CH<sub>4</sub> onset.

For 2MASS 1207 b, our retrieved atmospheric thermal structure is hotter than the CO–CH<sub>4</sub> transition curve at a given pressure layer (Figure 10), explaining the observed absence of CH<sub>4</sub> absorption features.

### 7.3. Unconstrained Carbon-Chemistry Quench Pressure

In fifteen out of twenty-four QEQ retrieval runs, including the thirteen with the lowest BIC values (QEQ-1 to QEQ-12), the inferred carbon-chemistry quench pressure has a median value around  $\log(P_{\text{quench}}/1 \text{ bar}) \approx -3.8$  dex with large uncertainties of  $\approx 1.0$  dex (Table 3 and Figure 7). This quench pressure is associated with disequilibrium chemistry (Section 5.2.3), which occurs when the timescale for vertical

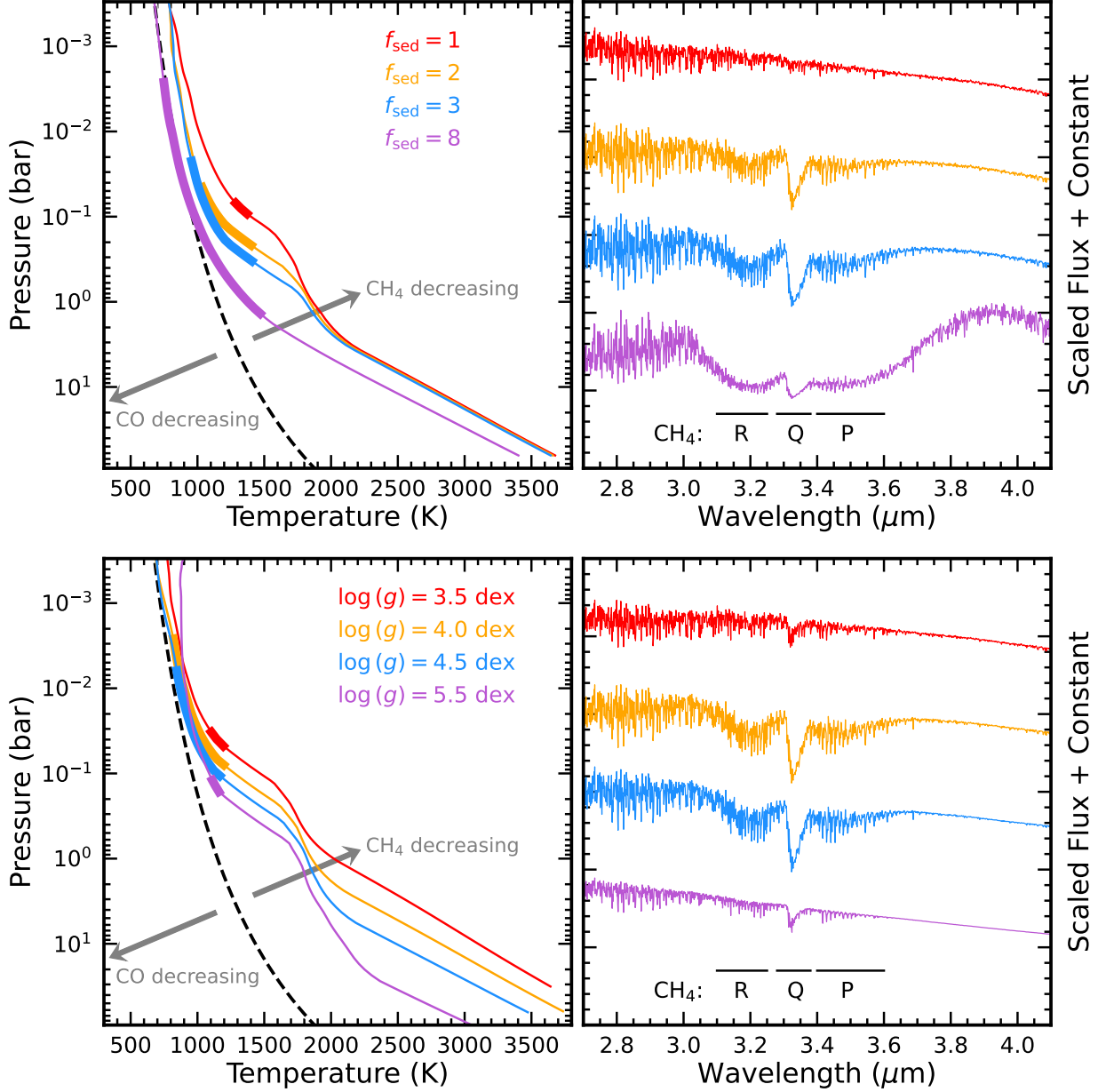


**Figure 12.** The top two panels present T-P profiles and corresponding spectra from the Sonora Diamondback models with varying  $f_{\text{sed}}$  values of 1 (red), 2 (orange), 3 (blue), and 8 (purple). All models have  $T_{\text{eff}} = 1400$  K,  $\log(g) = 4.5$  dex, and  $[M/H] = 0$  dex. The bottom two panels show models with varying  $\log(g)$  of 3.5 dex (red), 4.0 dex (orange), 4.5 dex (blue), and 5.5 dex, all with  $T_{\text{eff}} = 1200$  K,  $[M/H] = 0$  dex, and  $f_{\text{sed}} = 1$ . These panels follow the same format as Figure 11.

mixing in the atmosphere is shorter than that of chemical reactions such as  $\text{CO} \rightarrow \text{CH}_4$  (e.g., Prinn & Barshay 1977; Zahnle & Marley 2014). Strong vertical mixing can result in an overabundance of CO relative to  $\text{CH}_4$ , often leading to a carbon-chemistry quench pressure that is larger than photospheric pressures (e.g., Mollière et al. 2020; Zhang et al. 2023; Nasedkin et al. 2024b).

However, for 2MASS1207b, the retrieved low quench pressure of  $\log(P_{\text{quench}}/1 \text{ bar}) \approx -3.8$  dex should not be in-

terpreted as evidence for the absence of disequilibrium chemistry in its atmosphere. This quench pressure corresponds to atmospheric layers at higher altitudes and lower pressures than the photospheric regions of 2MASS1207b across  $1 - 5 \mu\text{m}$  (Figure 8). Therefore, the carbon-chemistry quench pressure is unconstrained by the observed JWST/NIRSpec spectrum and holds little physical meaning in this context.

As discussed in Section 7.2.2, the atmospheric thermal structure of 2MASS 1207 b is hotter than the CO- $\text{CH}_4$  tran-

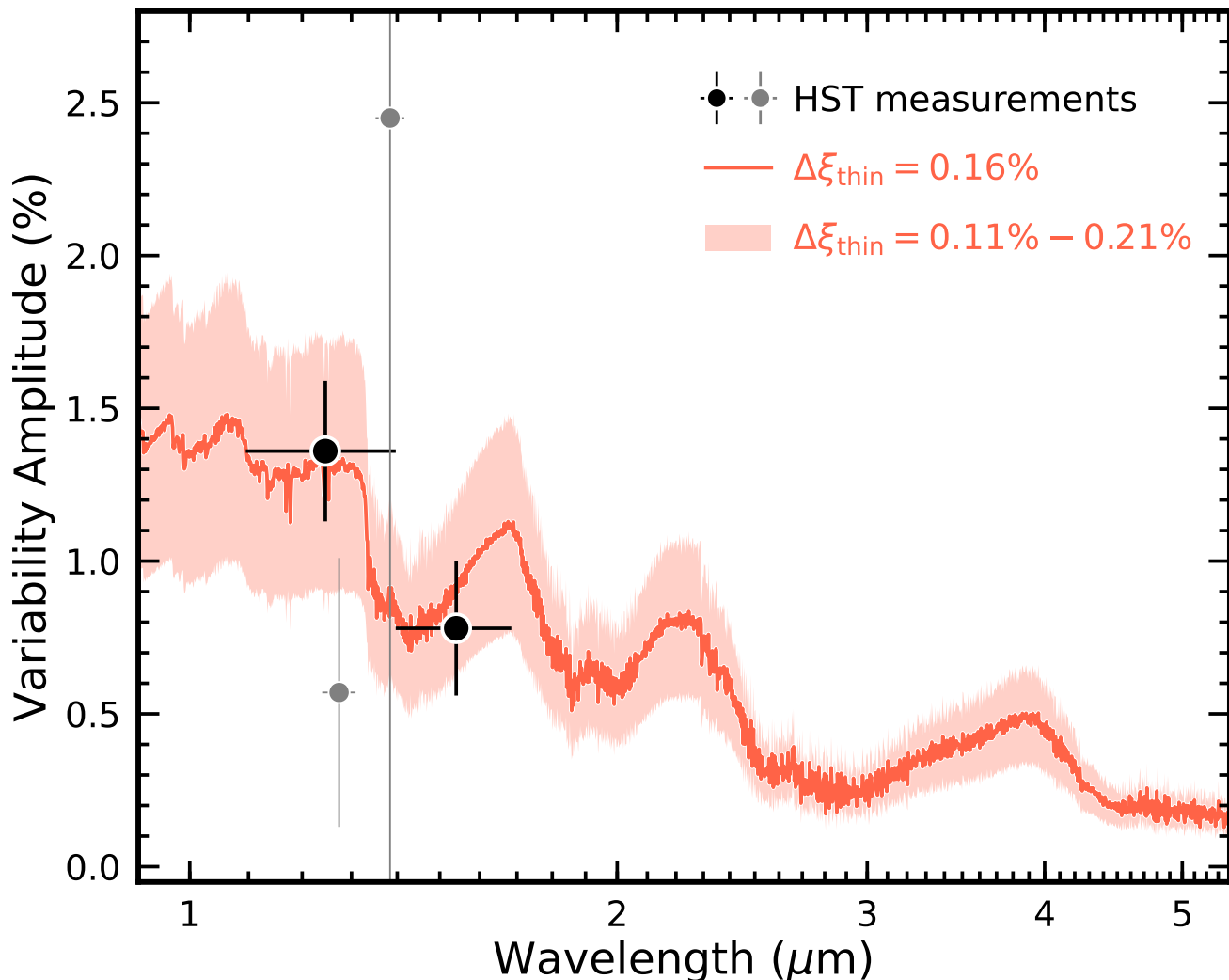


**Figure 13.** The variability amplitude as a function of wavelength predicted by our preferred retrieval setup,  $\text{QEQ-1}$ . The solid red line represents the variability amplitude when the fraction of thin-cloud patches changes by  $\Delta\xi_{\text{coll}} = 0.16\%$  (solid red line) from the maximum-likelihood value. The red-shaded region indicates the range of variability amplitudes when  $\Delta\xi_{\text{coll}} = 0.11\% - 0.21\%$ . Black and grey circles with error bars represent the measured variability amplitudes from Zhou et al. (2016), with grey circles corresponding to measurements from Zhou et al. (2019), which are affected by systematics.

sition curve at a given pressure layer, leading to a naturally CO-dominated and  $\text{CH}_4$ -deficient atmosphere, regardless of whether chemical equilibrium or disequilibrium conditions are present. Consequently, the potential effects of disequilibrium chemistry in the particular atmosphere of 2MASS 1207 b cannot be meaningfully constrained using carbon-chemistry quench pressures. This is in contrast to the colder L, T, and Y dwarfs, where the  $\text{CH}_4$  abundances in the upper atmospheres differ significantly between chemical equilibrium and disequilibrium conditions, enabling tighter constraints on the carbon-chemistry quench pressure.

#### 7.4. Matching the Observed Variability Amplitudes with Retrieved Atmospheric Properties

The atmospheric variability of 2MASS 1207 b has been previously detected. Using the HST Wide Field Camera 3, Zhou et al. (2016) reported rotationally modulated variability amplitudes of  $1.36\% \pm 0.23\%$  in the F125W filter (centered around  $1.25 \mu\text{m}$ ) and  $0.78\% \pm 0.22\%$  in the F160W filter (centered around  $1.54 \mu\text{m}$ ). Additionally, Zhou et al. (2019) obtained light curves in the F127M ( $\approx 1.27 \mu\text{m}$ ) and F139M ( $\approx 1.38 \mu\text{m}$ ) filters, which have 4–5 times narrower bandpasses compared to F125W and F160W. They measured variability amplitudes of  $0.57\% \pm 0.44\%$  and  $2.45\% \pm 2.67\%$  in F127M and F139M, respectively, though these measurements were notably influenced by strong systematics (see their Section 4.3).

We investigate whether the rotationally modulated variability amplitudes of 2MASS 1207 b are consistent with our most favored retrieval model, QEQ-1 (see, e.g., [Lew et al. 2020](#) and [Vos et al. 2023](#), for similar analyses of other objects). In this analysis, we assume the variability signal arises from geometric asymmetries in the coverage of thin-cloud patches and thick-cloud regions. Since the observed spectrum corresponds to the hemisphere of the atmosphere facing the observers, such asymmetries would lead to variations in the fraction of thin-cloud patches,  $\xi_{\text{thin}}$ , as the object rotates.

Starting with the maximum-likelihood value of  $\xi_{\text{thin}}^* = 8.65\%$  from QEQ-1, we introduce an increment  $\Delta\xi_{\text{thin}}$  to simulate the rotational modulations of the cloud coverage and compute a modified emergent spectrum ( $F_{\lambda,\text{tuned}}^*$ ), allowing for a comparison with the original, unmodified best-fit spectrum ( $F_{\lambda}^*$ ).

$$\begin{aligned} F_{\lambda}^* &= \xi_{\text{thin}}^* \times F_{\lambda,\text{thin}}^* + (1 - \xi_{\text{thin}}^*) \times F_{\lambda,\text{thick}}^* \\ F_{\lambda,\text{tuned}}^* &= (\xi_{\text{thin}}^* + \Delta\xi_{\text{thin}}) \times F_{\lambda,\text{thin}}^* \\ &\quad + [1 - (\xi_{\text{thin}}^* + \Delta\xi_{\text{thin}})] \times F_{\lambda,\text{thick}}^* \end{aligned} \quad (5)$$

where  $F_{\lambda,\text{thin}}^*$  and  $F_{\lambda,\text{thick}}^*$  represent the maximum-likelihood spectra from the thin-cloud and thick-cloud patches, respectively. Since thin-cloud patches probe deeper and hotter layers, they produce higher fluxes. i.e.,  $F_{\lambda,\text{thin}}^* > F_{\lambda,\text{thick}}^*$ .<sup>8</sup> Comparing  $F_{\lambda}^*$  and  $F_{\lambda,\text{tuned}}^*$  provides a measure of the variability amplitude as a function of wavelength,  $A_{\lambda}$ , as follows:

$$\begin{aligned} A_{\lambda} &= \frac{\text{abs}(F_{\lambda,\text{tuned}}^* - F_{\lambda}^*)}{F_{\lambda}^*} \\ &= \frac{\Delta\xi_{\text{thin}} \times (F_{\lambda,\text{thin}}^* - F_{\lambda,\text{thick}}^*)}{\xi_{\text{thin}}^* \times F_{\lambda,\text{thin}}^* + (1 - \xi_{\text{thin}}^*) \times F_{\lambda,\text{thick}}^*} \end{aligned} \quad (6)$$

The increment  $\Delta\xi_{\text{thin}}$  represents the asymmetry in atmospheric brightness distribution as the object rotates.

In [Figure 13](#), we show that small changes in the thin-cloud fraction, specifically  $\Delta\xi_{\text{thin}} = 0.11\% - 0.21\%$ , reproduce the near-infrared photometric variability amplitudes observed during the particular epochs studied by [Zhou et al. \(2016\)](#). These small  $\Delta\xi_{\text{thin}}$  values also yield variability amplitudes broadly consistent with the measurements by [Zhou et al. \(2019\)](#) using narrower filters, despite the large uncertainties and systematics affecting these data.

Our derived small values of  $\Delta\xi_{\text{thin}}$  suggest that the line-of-sight distribution of patchy clouds remains nearly symmetric

<sup>8</sup> We note that the conclusion of  $F_{\lambda,\text{thin}}^* > F_{\lambda,\text{thick}}^*$  does not conflict with [Figure 6](#). While the figure shows that the emergent spectra from thin-cloud patches,  $\xi_{\text{thin}}^* \times F_{\lambda,\text{thin}}^*$ , are not consistently brighter than those from thick-cloud regions,  $(1 - \xi_{\text{thin}}^*) \times F_{\lambda,\text{thick}}^*$ , across the 1–5  $\mu\text{m}$  range, this result arises from the scaling factors ( $\xi_{\text{thin}}^*$  and  $1 - \xi_{\text{thin}}^*$ ) applied to the corresponding contributions, rather than the intrinsic brightness ( $F_{\lambda,\text{thin}}^*$  and  $F_{\lambda,\text{thick}}^*$ ) of the atmospheric components themselves.

as 2MASS 1207 b rotates during the particular HST monitoring by [Zhou et al. \(2016\)](#). This can partially result from this object’s spin axis inclination, which remains unknown. Observational and theoretical studies have suggested that objects with nearly edge-on viewing angles ( $i = 90^\circ$ ) tend to exhibit higher variability amplitudes than those with lower inclinations (e.g., [Vos et al. 2017](#); [Tan & Showman 2021](#); [Fuda & Apai 2024](#)). Directly measuring the inclination of 2MASS 1207 b via high-resolution spectroscopy is thus useful to understanding its role in this object’s observed variability signals. Additionally, the atmospheric brightness distribution may evolve over multiple rotation periods, as observed in other brown dwarfs and planetary-mass companions (e.g., [Yang et al. 2016](#); [Apai et al. 2017](#); [Zhou et al. 2022](#); [Biller et al. 2024](#)) and as predicted by three-dimensional general circulation models (e.g., [Tan & Showman 2021](#); [Lee et al. 2024](#)). A deeper understanding of 2MASS 1207 b’s top-of-atmosphere inhomogeneity would benefit from dedicated variability monitoring observations (e.g., JWST GO program 3181).

### 7.5. Atmospheric Composition

[Figure 14](#) shows the atmospheric metallicity and carbon-to-oxygen ratio of 2MASS 1207 b, derived from multiple retrieval runs. While these values exhibit significant scatter across retrievals with high  $\Delta\text{BIC}$ , they converge to near-solar compositions in runs with lower  $\Delta\text{BIC}$  values. This trend is also observed in other key retrieved parameters, including the fraction of thin-cloud patches ( $\xi_{\text{thin}}$ ), effective temperatures, surface gravities, and radii ([Figures 14–15](#)). Our extensive retrieval analysis indicates the sensitivity of inferred atmospheric compositions to retrieval assumptions. For instance, cloud-free retrieval runs (QEQ-21 to QEQ-24) yield high  $[\text{M}/\text{H}]$  values of 0.8–2.0 dex and very low  $\text{C}/\text{O}$  values near 0.1. In contrast, the statistically preferred retrievals (e.g., QEQ-1 to QEQ-7), which account for patchy clouds, derive solar-like  $[\text{M}/\text{H}]$  and  $\text{C}/\text{O}$  values for 2MASS 1207 b (see below). These striking differences indicate that relying on a single retrieval setup risks biasing the inferred  $[\text{M}/\text{H}]$ ,  $\text{C}/\text{O}$ , and other physical parameters, potentially distorting our understanding of the system’s formation and evolution history.

Focusing on retrieval runs with the seven lowest BIC values (QEQ-1 to QEQ-7), the inferred  $[\text{M}/\text{H}]$  of 2MASS 1207 b ranges from  $-0.12$  to  $+0.10$  dex, and  $\text{C}/\text{O}$  from 0.44 to 0.52 ([Table 3](#)). These retrievals incorporate models of atmospheric inhomogeneity, such as patchy clouds or a combination of patchy clouds and hot spots ([Figure 5](#)), and explore various assumptions about cloud composition and parameter priors. Despite these differences in model assumptions, their consistent results support the robustness of the near-solar  $[\text{M}/\text{H}]$  and  $\text{C}/\text{O}$  values. Specifically, the most favored retrieval setup, QEQ-1, yields a  $[\text{M}/\text{H}] = -0.05 \pm$

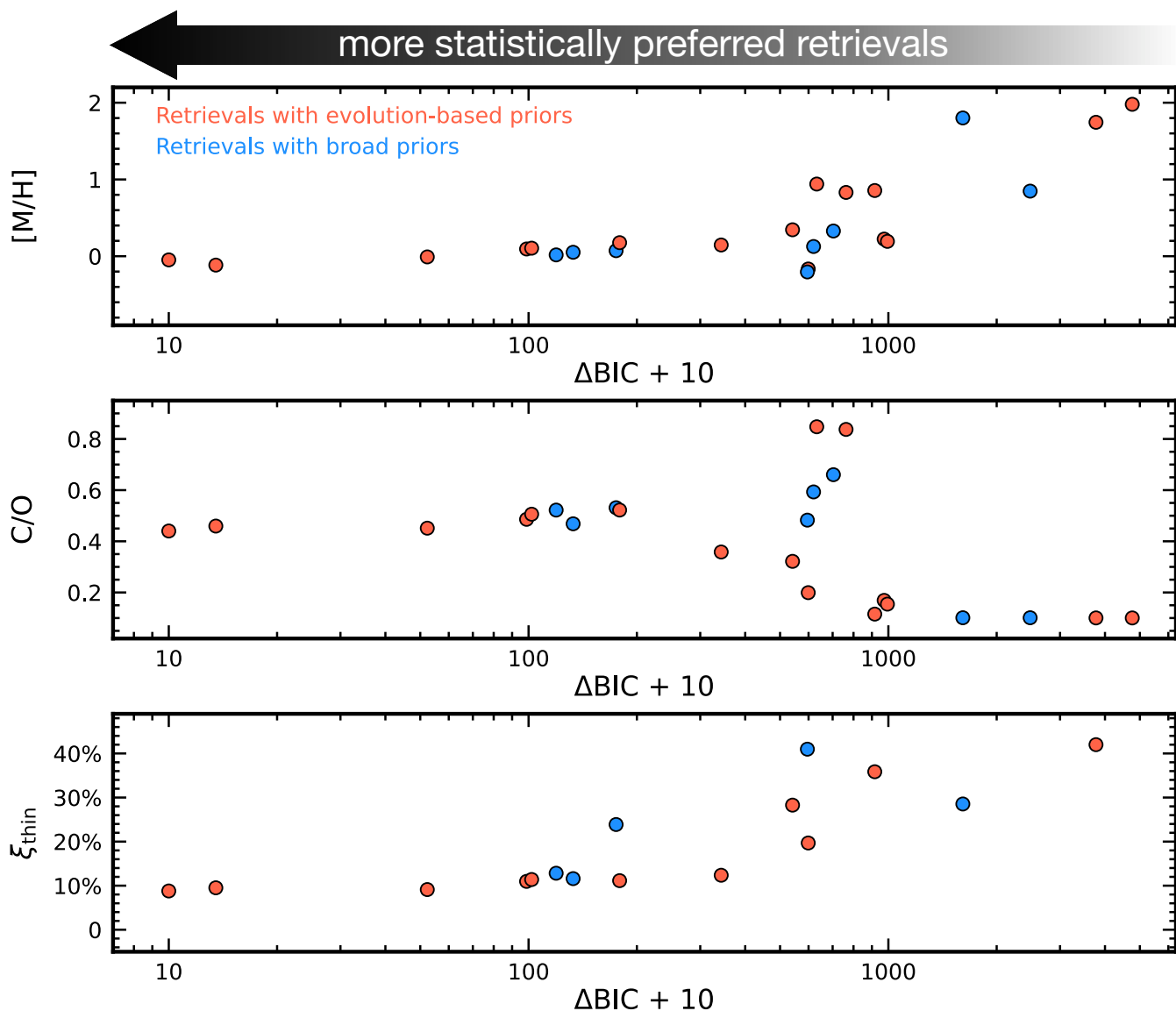


**Figure 14.** The atmospheric metallicity (top), carbon-to-oxygen ratio (middle), and  $\xi_{\text{thin}}$  (bottom) inferred from all QEQ retrieval setups. The parameter  $\xi_{\text{thin}}$  is only defined in inhomogeneous atmospheric models. For schemes with patchy clouds or a combination of patchy clouds and hot spots,  $\xi_{\text{thin}}$  represents the fraction of thin-cloud patches; for the hot-spot scheme, it describes the fraction of the column with a hotter thermal structure (i.e., hot spots; Section 5.4). Retrievals with evolution-based priors for surface gravity, radius, and mass are shown in orange, while those with broad parameter priors are shown in blue.

0.03 dex and a  $C/O$  of  $0.440 \pm 0.012$ .<sup>9</sup> As a member of the TW Hydrae association, 2MASS 1207 b’s near-solar  $[M/H]$

<sup>9</sup> The inferred atmospheric compositions of 2MASS 1207 b — and more broadly, those of exoplanets and brown dwarfs — are derived from disk-integrated spectra, which average out potential three-dimensional spatial variations in atmospheric abundances. Studies of Jupiter suggested that certain gas abundances retrieved from disk-integrated spectra can differ from those of localized regions (e.g., Gapp et al. 2024; Irwin et al. 2025). Comparing the globally and locally inferred atmospheric properties of solar-system planets, such as Jupiter, provides crucial context for interpreting exoplanet and brown dwarf atmospheres and remains a key topic of ongoing research.

is consistent with stellar members of other nearby young moving groups (e.g., Santos et al. 2008; Ammler-von Eiff & Guenther 2009; Viana Almeida et al. 2009; D’Orazi et al. 2011; Biazzo et al. 2011, 2012a, 2017).

To further investigate the formation and evolution history of the 2MASS 1207 A+b system, it is essential to compare the atmospheric compositions of 2MASS 1207 b with its primary, 2MASS 1207 A. Previous studies suggest that 2MASS 1207 b likely formed through gravitational instability in a collapsing molecular cloud rather than through core accretion (e.g., Lodato et al. 2005; Gizis et al. 2005; Chau-

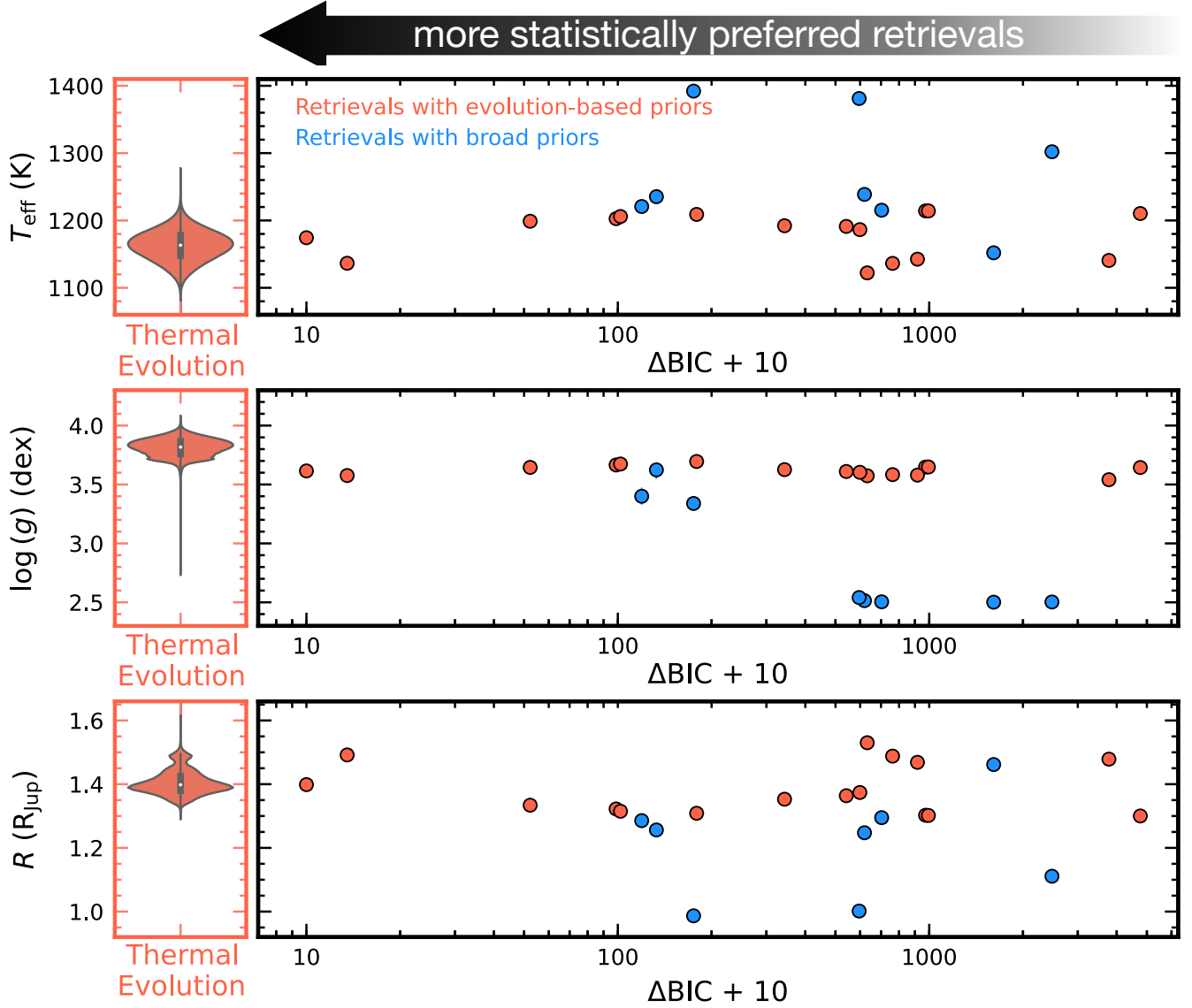


**Figure 15.** The left column presents violin plots for the effective temperature, surface gravity, and radius of 2MASS 1207 b, as determined from thermal evolution models. These plots are based on the concatenated chains of parameters inferred from various evolution models (see Section 4.2). The right column presents the  $T_{\text{eff}}$ ,  $\log(g)$ , and  $R$  values from all QEQ retrieval setups, following the same format as Figure 14.

vin et al. 2005; Boss 2006; Stamatellos & Whitworth 2009), given that the companion-to-host mass ratio of this system ( $\sim 0.2$ ; see Section 2.3) is much higher than the majority of exoplanet-host systems (e.g., Figure 3 of Zhang et al. 2021b). Gravitational instability could result in similar atmospheric compositions for both components, as observed in members of binary systems and stellar clusters (e.g., Santos et al. 2008; Biazzo et al. 2012b; Hawkins et al. 2020; Nelson et al. 2021), although interactions between 2MASS 1207 b and its environment, such as planetesimal accretion or orbital migration within the disk surrounding 2MASS 1207 A (e.g., Helled et al. 2006; Helled & Bodenheimer 2010; Helled & Schubert 2009; Boley & Durisen 2010; Schneider & Bitsch 2021; Mol-

lière et al. 2022), may have altered their relative abundances. Measuring and comparing the present-day atmospheric compositions of 2MASS 1207 A and b will provide insights into the presence and impacts of these post-formation processes.

### 7.6. Comments on the Variations in Retrieval Setups

In this section, we discuss the results of retrievals that use different assumptions from the QEQ-1 setup to provide additional insights into the atmospheric properties of 2MASS1207b.

#### 7.6.1. Retrievals with Cloud-free Atmospheres

Figure 16 presents the retrieval results of QEQ-22, which assumes a homogeneous, cloud-free atmosphere with broad

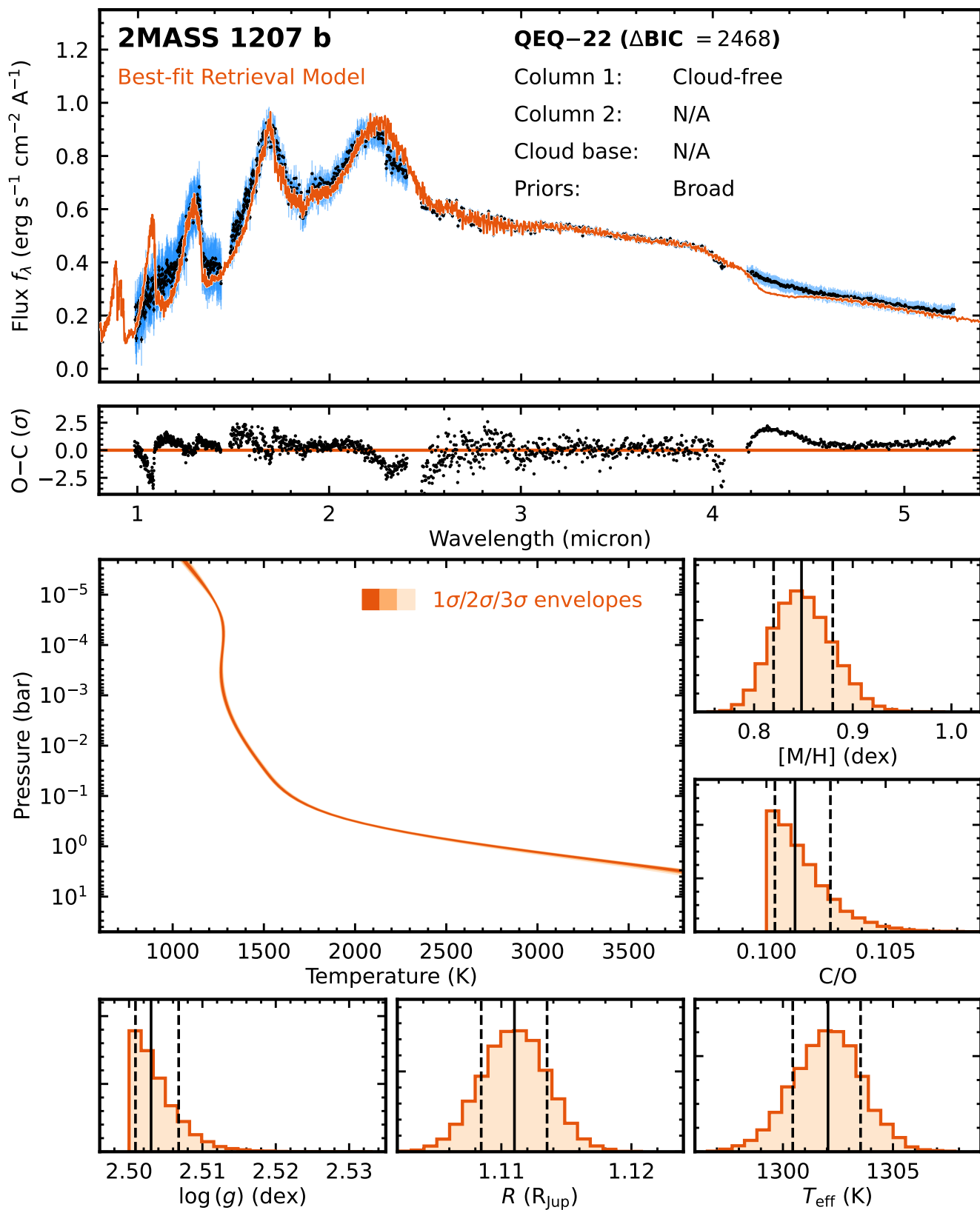


**Figure 16.** Retrieval results for QEQ-22, which assumes a homogeneous cloud-free atmosphere with broad priors for  $\log g$ ,  $R$ , and  $M$  (see Section 7.6.1). These panels follow the same format as Figure 6.

priors for  $\log(g)$ ,  $R$ , and  $M$ . This setup corresponds to a simplified scenario under scheme (a) in our atmospheric inhomogeneity framework (Section 5.4). Significant discrepancies are evident between data and fitted models in the  $Y$  band, the blue wing of the  $H$  band, the flux peak of the  $K$  band, and around  $4.3 \mu\text{m}$ . Moreover, the retrieved values for  $T_{\text{eff}}$ ,  $\log(g)$ , and  $R$  (Table 3) deviate significantly from the inferred parameters based on thermal evolution models (Table 1).

A more sophisticated cloud-free model that incorporates hot and cold spots, such as QEQ-21, provides a better, though still inadequate, fit to the observations (Figure 17). This model corresponds to the scheme (c) in our atmospheric inhomogeneity framework (Section 5.4) and combines two T-P profiles with consistent temperatures and temperature gradients at  $P \geq 10$  bar (Section 5.4.3). However, as shown in Figure 17, the retrieved T-P profiles show temperature contrasts of up to  $\sim 800$  K at pressures between  $\sim 10^{-5}$  bar and  $\sim 1$  bar, along with an upper-atmosphere thermal inversion in cold spots. It is challenging to justify how such large temperature differences between the two atmospheric columns could remain stable over time, especially given that 2MASS 1207 b is not tidally locked nor exposed to intense external radiation from 2MASS 1207 A.

Thus, within our retrieval frameworks, the JWST/NIRSpec spectrum of 2MASS 1207 b cannot be fully explained by cloud-free models. This conclusion aligns with the findings of Luhman et al. (2023), who showed that cloud-free ATMO2020 models — assuming one-dimensional homogeneous atmosphere with adjusted adiabatic indices — cannot reproduce all the observed spectral features of 2MASS 1207 b.

### 7.6.2. Retrievals with Homogeneous Cloudy Atmospheres

Figure 18 presents the retrieval results of QEQ-20, which assumes a homogeneous atmosphere with  $\text{MgSiO}_3$  and Fe clouds with base pressures determined from equilibrium chemistry. Evolution-based priors are used for  $\log(g)$ ,  $R$ , and  $M$ . While this cloudy model significantly improves the fit to the JWST/NIRSPEC spectrum of 2MASS 1207 b compared to cloud-free retrievals (Section 7.6.1), notable systematic discrepancies between the data and models remain. Specifically, the retrieved model spectrum shows (1) fainter fluxes near the peaks of  $J$ ,  $H$ , and  $K$  bands, (2) inconsistent depths of the  $K$  I doublet near  $1.25 \mu\text{m}$ , (3) mismatched shapes in the blue wing of  $H$  band and the red wing of the  $K$  band, and (4) overall fainter fluxes between  $3.7$  and  $4.0 \mu\text{m}$ .

The retrieved iron cloud in this model has an unusually high mass fraction at its base pressure, with  $\log(X_{0,\text{Fe}}) \approx -0.11$ . The enstatite cloud is vertically extended, with a very low sedimentation efficiency of  $f_{\text{sed},\text{MgSiO}_3} \approx 0.04$  and a large mass fraction of  $\log(X_{0,\text{MgSiO}_3}) \sim -2.90$  at its base pressure. These parameters suggest that both cloud species contribute

significantly to the atmospheric opacity, helping to explain the red spectral slope of 2MASS 1207 b but failing to reproduce detailed spectral features.

To refine the fit, we adjust the QEQ-20 setup by treating the base pressures of the enstatite and iron clouds as free parameters, resulting in the QEQ-15 retrieval (Figure 19). This modification yields improved agreement with the observations but still shows discrepancies. Specifically, this model predicts slightly brighter fluxes in  $1.1 - 1.3 \mu\text{m}$ , fainter fluxes in  $3.7 - 4.0 \mu\text{m}$ , and a weak  $3.3 \mu\text{m}$   $\text{CH}_4$  feature that is not observed. The retrieved base pressures for iron and enstatite clouds are  $\log(P_{\text{base,Fe}}/1 \text{ bar}) \approx -1.48$  and  $\log(P_{\text{base,Fe}}/1 \text{ bar}) \approx -4.7$ , respectively. These pressures indicate that the cloud layers are located at higher altitudes and lower pressures than predicted by chemical equilibrium models.

The systematic mismatches between data and models observed in QEQ-20 and QEQ-13 are consistent across other retrievals assuming homogeneous cloudy atmospheres. These findings highlight the value of inhomogeneous atmospheric models for explaining the spectrum of 2MASS1207b.

### 7.6.3. Retrievals with a Combination of Patchy Clouds and Hot Spots

Figure 20 presents the retrieval results for QEQ-13, which assumes a combination of patchy forsterite and iron clouds along with hot spots. Evolution-based priors are used for  $\log(g)$ ,  $R$ , and  $M$ . This model corresponds to scheme (d) in our atmospheric inhomogeneity framework (Section 5.4) and significantly improves the spectral fits compared to cloud-free models (Section 7.6.1) and homogeneous cloudy models (Section 7.6.2).

QEQ-13 suggests that thin-cloud patches cover  $\sim 20\%$  of 2MASS 1207 b's atmosphere. These regions contain vertically extended  $\text{Mg}_2\text{SiO}_4$  clouds with  $f_{\text{sed},\text{Mg}_2\text{SiO}_4} \approx 1$ , combined with low Fe cloud content, resulting in an emergent spectrum resembling that of an L dwarf. The remaining  $80\%$  of the atmosphere are thick-cloud regions with vertically compact ( $f_{\text{sed}} > 9$ ) but significantly abundant  $\text{Mg}_2\text{SiO}_4$  and Fe clouds, producing a blackbody-like spectrum. These properties align with the results from the most favored retrieval model, QEQ-1 (Section 7.1).

We further adjust the QEQ-13 setup by incorporating a gray cloud layer into the second atmospheric column, leading to the QEQ-9 model (Figure 21). This adjustment improves the data-model consistencies further. QEQ-9 suggests that thin-cloud patches cover  $\sim 11\%$  of 2MASS 1207 b's atmosphere and produce an L-dwarf-like spectrum, while the remaining  $89\%$  thick-cloud regions have low  $\text{Mg}_2\text{SiO}_4$  and Fe cloud content, combined with a high-opacity gray cloud layer located at  $\sim 10^{-5}$  bar. The gray cloud dominates the opacity, resulting in a blackbody-like emergent spectrum. The T-P profiles between the two atmospheric columns are consistent

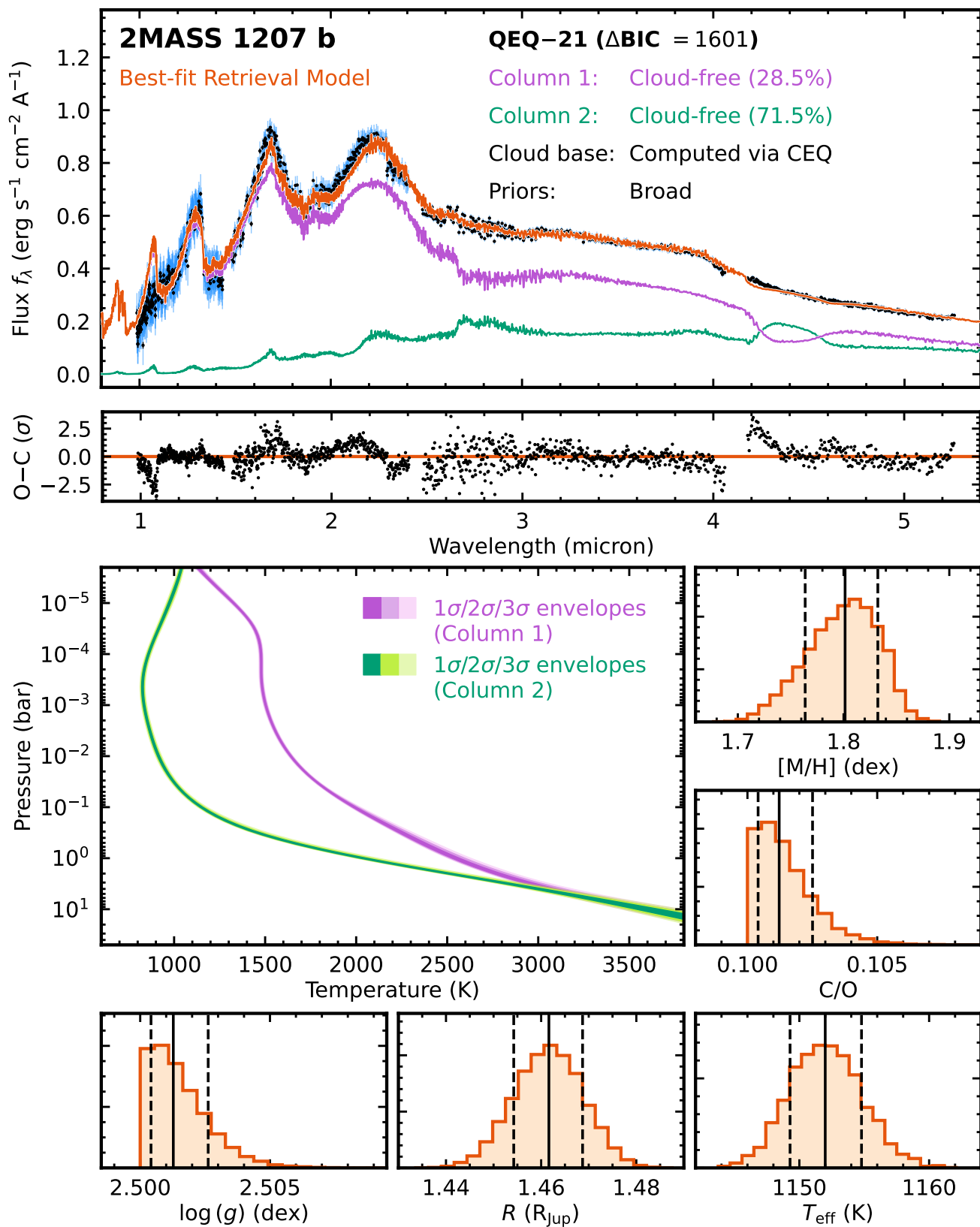


**Figure 17.** Retrieval results for QEQ-21, which assumes an inhomogeneous atmosphere with cloud-free hot/cold spots, along with broad priors for  $\log g$ ,  $R$ , and  $M$  (see Section 7.6.1). The middle left panel presents the retrieved T-P profiles from individual atmospheric columns. These panels follow the same format as Figure 6.

in this model, justifying the adequacy of a single T-P profile, as used in QEQ-1, to describe the NIRSpec spectrum of 2MASS 1207 b.

The combination of thin-cloud patches with L-dwarf-like spectra and thick-cloud regions with blackbody-like spectra, as seen in QEQ-13 and QEQ-9, is consistently supported by other retrievals that incorporate patchy clouds and hot/cold spots. These findings strongly corroborate the atmospheric scenario inferred by QEQ-1, emphasizing the critical role of inhomogeneous atmospheres in explaining the observations of 2MASS1207b.

## 8. SUMMARY

2MASS 1207 b is the first planetary-mass companion discovered by direct imaging (Chauvin et al. 2004, 2005). We have studied the atmospheric properties of this remarkable object based on its JWST/NIRSpec spectrum and atmospheric retrievals, with the main findings summarized below.

- We contextualized the physical parameters of 2MASS 1207 b using several thermal evolution models based on its bolometric luminosity and age. These evolution-based properties — including  $T_{\text{eff}} = 1163_{-23}^{+23}$  K,  $\log(g) = 3.82_{-0.07}^{+0.09}$  dex,  $R = 1.40_{-0.04}^{+0.03}$   $R_{\text{Jup}}$ , and  $M = 5.2_{-0.7}^{+0.6}$   $M_{\text{Jup}}$  — provide key physics-driven priors for our atmospheric retrieval analyses.
- We have performed extensive atmospheric retrieval analyses of 2MASS 1207 b’s JWST NIRSpec spectrum using a newly developed atmospheric inhomogeneity framework. This framework enables the characterization of self-luminous exoplanets, brown dwarfs, and low-mass stars under four atmospheric schemes: (1) homogeneous atmospheres, (2) patchy clouds, (3) cloud-free hot spots, and (4) a combination of patchy clouds and hot spots. The latter three schemes are particularly suited for objects exhibiting atmospheric variabilities, such as 2MASS 1207 b.
- We have conducted 24 retrieval runs with variations in atmospheric inhomogeneity, parameter priors, and cloud properties. The most statistically preferred retrieval model, QEQ-1, corresponds to the patchy cloud scheme. This retrieval model incorporates evolution-based priors for key physical parameters and yields an  $T_{\text{eff}} = 1174_{-3}^{+4}$  K, a surface gravity of  $\log(g) = 3.62_{-0.02}^{+0.03}$  dex, and a radius of  $R = 1.399_{-0.010}^{+0.008}$   $R_{\text{Jup}}$ .
- The QEQ-1 retrieval model suggests that  $\sim 9\%$  of 2MASS 1207 b’s atmosphere is covered by thin-cloud patches with Fe clouds and a lower  $\text{Mg}_2\text{SiO}_4$  cloud content, producing L-dwarf-like emergent spectra. The remaining 91% of the atmosphere consists of thick-cloud regions with vertically extended  $\text{Mg}_2\text{SiO}_4$  and Fe clouds, resulting in blackbody-like spectra with fluxes peaking at  $\sim 2.5 \mu\text{m}$ . This scenario is consistently supported by other retrieval runs that incorporate clouds and inhomogeneous atmospheres. Furthermore, when a gray cloud layer is incorporated into one of the atmospheric columns, the retrieved models indicate that the thick-cloud regions are characterized by a high-altitude gray cloud layer at low pressures around  $10^{-5}$  bar.
- The inhomogeneous atmosphere of 2MASS 1207 b is analogous to that of Jupiter, which exhibits a banded structure of belts and zones. Our retrievals indicate that 2MASS 1207 b has thin-cloud patches, with photospheric temperatures of 1600–1700 K and thick-cloud regions with slightly cooler photospheric temperatures of 1100–1200 K, resembling Jupiter’s belts and zones, respectively.
- The thick clouds and potentially high-altitude gray cloud content of 2MASS 1207 b, as suggested by our retrieval analyses, may be contributed by this object’s ongoing accretion of dust and gas. Extreme events such as the impact of Comet Shoemaker-Levy 9 on Jupiter may also influence the evolution of 2MASS 1207 b. Follow-up studies are needed to investigate the potential occurrence and impact of such processes.
- The previously noted but unexplained unique spectral features of 2MASS 1207 b can now be understood through our retrieved atmospheric properties. The weak CO absorption over 4.4–5.2  $\mu\text{m}$  likely arises from veiling effects caused by patchy thick clouds. The blackbody-like featureless spectra from the thick-cloud regions dilute the contributions from the thin-cloud patches, which exhibit prominent CO absorption and share a spectral morphology similar to VHS 1256 b.
- The absence of 3.3  $\mu\text{m}$   $\text{CH}_4$  absorption in 2MASS 1207 b can be explained by this object’s relatively hot atmospheric thermal structure, which leads to a CO-dominant,  $\text{CH}_4$ -deficient atmosphere. As a result, the potential effects of disequilibrium chemistry in the particular atmosphere of 2MASS 1207 b cannot be meaningfully constrained using carbon-chemistry quench pressures. This contrasts with colder L, T, and Y dwarfs, where  $\text{CH}_4$  abundances in the upper atmospheres differ significantly between chemical equilibrium and disequilibrium conditions, enabling tighter constraints on the carbon-chemistry quench pressure.
- The retrieved atmospheric models can match the observed rotationally modulated variabilities of 2MASS 1207 b. Based on QEQ-1, small perturbations in the thin-cloud coverage ( $\xi_{\text{thin}}$ ) from its

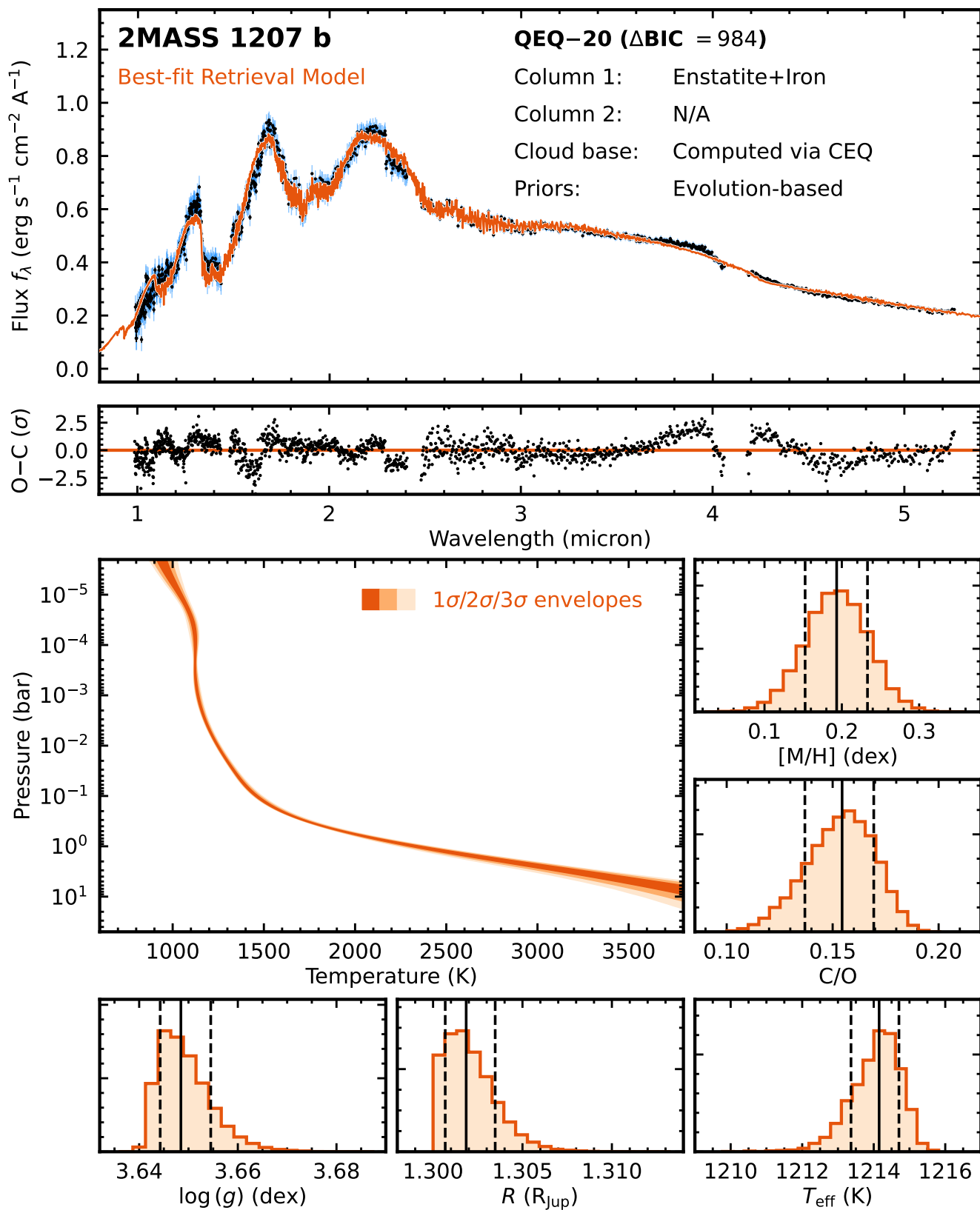


**Figure 18.** Retrieval results for QEQ-20, which assumes a homogeneous atmosphere with enstatite and iron clouds, with their base pressured determined from equilibrium chemistry (see Section 7.6.3). Evolution-based priors are adopted for  $\log g$ ,  $R$ , and  $M$ . These panels follow the same format as Figure 6.

maximum-likelihood value by increments of  $\Delta\xi_{\text{thin}} = 0.11\% - 0.21\%$  reproduce the variability amplitudes observed in broadband HST/WFC3 filters.

- Our analysis reveals that the inferred atmospheric properties of 2MASS1207b are sensitive to assumptions in retrieval models. Atmospheric properties such as  $[M/H]$  and  $C/O$  show significant scatter across retrieval runs with high BICs but converge to consistent values among the statically preferred models. Cloud-free retrieval runs yield high  $[M/H]$  values of 0.8–2.0 dex and very low  $C/O$  values near 0.1. In contrast, statistically preferred retrieval runs consistently suggest that 2MASS 1207 b has near-solar compositions that line up with those of stellar members in nearby young moving groups. The most preferred retrieval model (QEQ-1) derives  $[M/H] = -0.05 \pm 0.03$  dex and  $C/O = 0.440 \pm 0.012$  for 2MASS 1207 b. These findings underscore the importance of exploring diverse assumptions in retrievals to avoid biased interpretations of atmospheres, formation pathways, and evolution histories.

Beyond these findings specific to 2MASS 1207 b, we have developed several new methodologies for atmospheric studies of self-luminous exoplanets, brown dwarfs, and low-mass stars:

- A new spectroscopy-based bolometric correction approach designed to mitigate modeling systematics in bolometric luminosity estimates (Section 4.1 and Appendix A).
- An expanded grid of chemical equilibrium abundances<sup>10</sup> for `petitRADTRANS`, which extends the temperature range and incorporates additional atomic and molecular species (Section 5.2.2).
- An atmospheric retrieval framework for characterizing both homogeneous and inhomogeneous atmospheres (Section 5.4), as summarized above.

Future observational studies of 2MASS 1207 b, such as JWST MIRI spectroscopy (GTO program 1270) and time-series NIRSpec spectroscopy (GO program 3181), will provide new insights into this remarkable planetary-mass companion. In particular, follow-up atmospheric retrieval analyses of combined NIRSpec and MIRI data for 2MASS 1207 b

should account for both its inhomogeneous atmosphere and the possible presence of its circumsecondary disk, which, if present, could contribute to the flux at MIRI wavelengths. Additionally, detailed atmospheric studies of its host, 2MASS 1207 A, will offer a crucial context for understanding formation pathways and the evolutionary history of this planetary system.

We thank the anonymous referee for suggestions that improved the manuscript. Z.Z. thanks Gaël Chauvin, Gabriel-Dominique Marleau, and Elena Manjavacas for helpful comments and thanks Andy Skemer and Xi Zhang for discussions during the early stages of this work. Z.Z. acknowledges the support of the NASA Hubble Fellowship grant HST-HF2-51522.001-A awarded by the Space Telescope Science Institute, which is operated by the Association of Universities for Research in Astronomy, Inc., for NASA, under contract NAS5-26555. We acknowledge the use of the lux supercomputer at UC Santa Cruz, funded by NSF MRI grant AST 1828315. This work has made use of data from the European Space Agency (ESA) mission Gaia (<https://www.cosmos.esa.int/gaia>), processed by the Gaia Data Processing and Analysis Consortium (DPAC, <https://www.cosmos.esa.int/web/gaia/dpac/consortium>). Funding for the DPAC has been provided by national institutions, in particular, the institutions participating in the Gaia Multilateral Agreement. The data presented in this article were obtained from the Mikulski Archive for Space Telescopes (MAST) at the Space Telescope Science Institute. The specific observations analyzed can be accessed via DOI: 10.17909/jzze-5611.

Z.Z. warmly acknowledges the love and support of his wife, Yanxia Li, and the arrival of our daughter, Allison Muzi Zhang, whose presence has brought immense joy and inspiration during the completion of this work.

*Facilities:* JWST (NIRSpec)

*Software:* `petitRADTRANS` (Mollière et al. 2019; Nasedkin et al. 2024a), `easyCHEM` (Mollière et al. 2017; Lei & Mollière 2024), `MultiNest` (Feroz & Hobson 2008; Feroz et al. 2009, 2019), `PyMultiNest` (Buchner et al. 2014), `corner.py` (Foreman-Mackey 2016), `astropy` (Astropy Collaboration et al. 2013, 2018), `ipython` (Pérez & Granger 2007), `numpy` (Oliphant 2006), `scipy` (Jones et al. 2001), `matplotlib` (Hunter 2007).

## APPENDIX

<sup>10</sup> <https://doi.org/10.5281/zenodo.15654694>

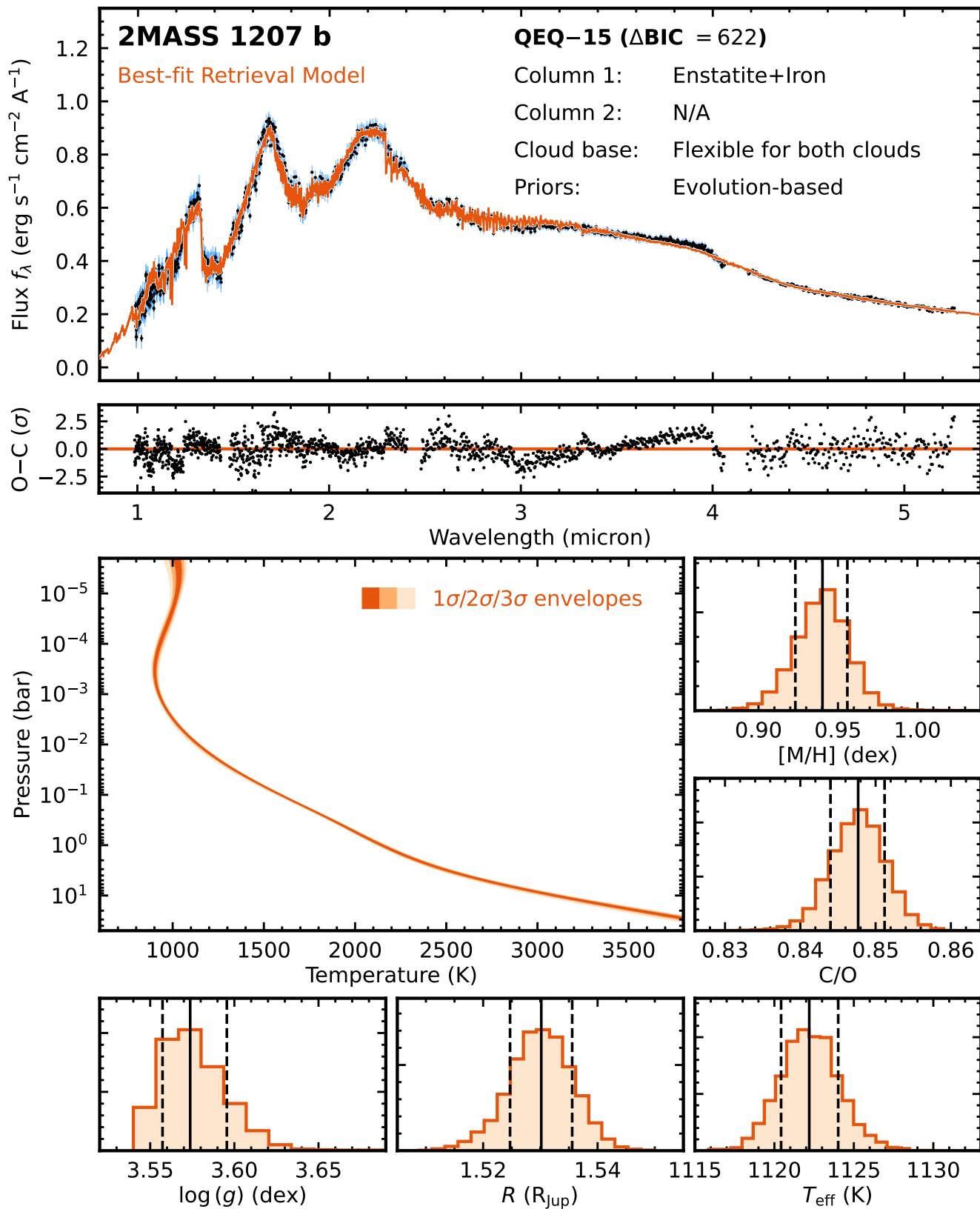


**Figure 19.** Retrieval results for QEQ-15, which resembles the QEQ-20 setup (Figure 18) but allows the cloud base pressures to vary as free parameters (see discussions in Section 7.6.3). Evolution-based priors are adopted for  $\log g$ ,  $R$ , and  $M$ . These panels follow the same format as Figure 6.

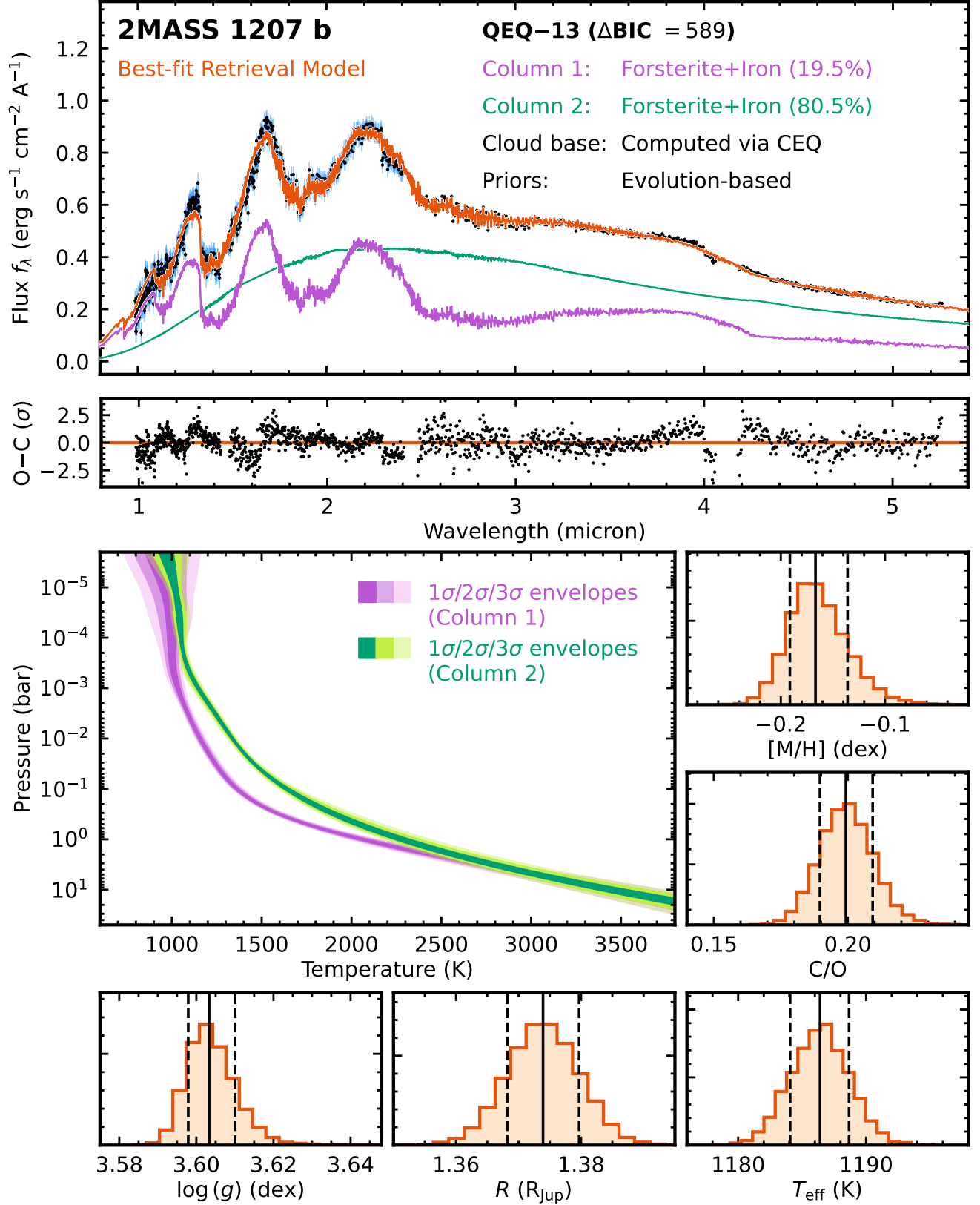


**Figure 20.** Retrieval results for QEQ-13, which assumes an inhomogeneous atmosphere with patchy forsterite and iron clouds with hot spots (see discussions in Section 7.6.3). Evolution-based priors are adopted for  $\log g$ ,  $R$ , and  $M$ . These panels follow the same format as Figure 6.

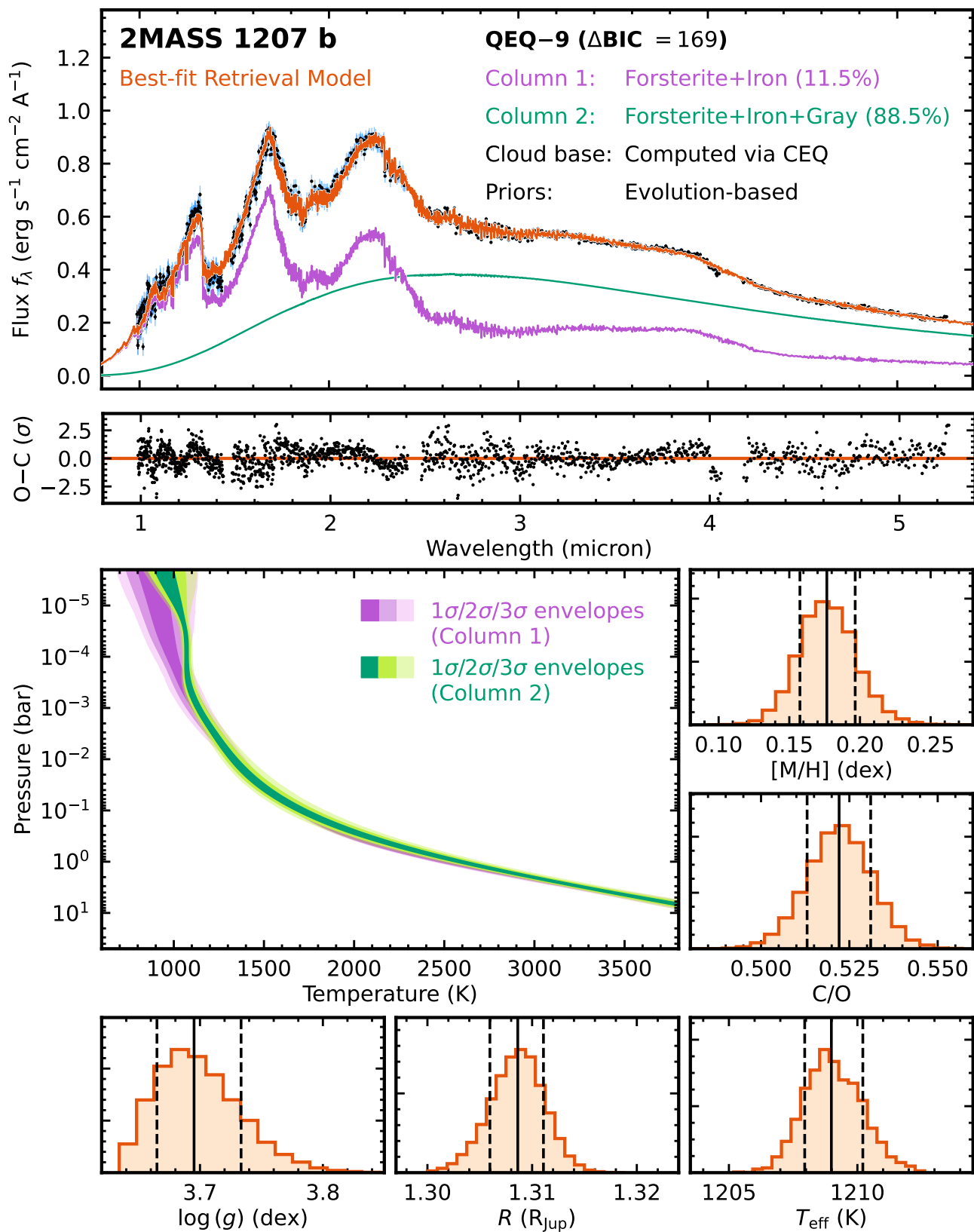


**Figure 21.** Retrieval results for QE9-9, which resembles the QE9-13 setup (Figure 20) but adds a gray cloud component to the second atmospheric column (see discussions in Section 7.6.3). Evolution-based priors are adopted for  $\log g$ ,  $R$ , and  $M$ . These panels follow the same format as Figure 6.

## A. A NEW SPECTROSCOPY-BASED BOLOMETRIC CORRECTION WITH MITIGATED MODELING SYSTEMATICS

### A.1. An Overview of Bolometric Luminosity Measurements

Bolometric luminosity is a critical physical property for understanding the thermal evolution and atmospheric energy budget of exoplanets, brown dwarfs, and stars. However, directly measuring  $L_{\text{bol}}$  is challenging due to the limited wavelength coverage of typical spectroscopic observations. To address this, several methods have been commonly adopted to estimate the bolometric luminosities of self-luminous exoplanets and brown dwarfs by extrapolating their observed spectrophotometry to cover the full wavelength range.

For objects with spectrophotometry spanning wavelengths typically broader than  $1 \mu\text{m}$ , atmospheric model spectra that best match the observations are often used for extrapolation (e.g., Mann et al. 2013; Filippazzo et al. 2015; Zhang et al. 2021c,d; Luhman et al. 2023). However, this spectral-fitting approach may be excessive if the primary goal is only to derive  $L_{\text{bol}}$  or if an  $L_{\text{bol}}$  value is required beforehand to inform spectral fits (e.g., Zhang et al. 2023; see also Section 4). Moreover, rigorous spectral fitting typically involves accounting for model grid interpolation uncertainties (e.g., Czekala et al. 2015; Gully-Santiago et al. 2017; Zhang et al. 2021c,d) and employing complex covariance matrices for likelihood evaluations, which are unnecessary when the objective is limited to  $L_{\text{bol}}$  estimation.

These studies also often rely on a single grid of model atmospheres, which can introduce systematics arising from the specific assumptions inherent in the chosen models, potentially leading to model-dependent biases and underestimated uncertainties in the inferred  $L_{\text{bol}}$  values. For example, Zhang et al. (2025) used fourteen different grids of atmospheric models to estimate the bolometric luminosities of the T/Y planetary-mass companion COCONUTS-2b. While their uncertainties in individual  $L_{\text{bol}}$  estimates were small (0.004 – 0.01 dex), Zhang et al. (2025) found a significant scatter of  $\approx 0.5$  dex among these estimates, driven by the vastly different assumptions within the models. Eliminating such modeling systematics is nearly impossible in exoplanet and brown dwarf studies. Directly observing a substantial portion of a given object’s SED across broad wavelengths — enabled by the combination of JWST NIRSpec and MIRI — provides a robust approach to reducing the modeling systematics to the level of or below measurement uncertainties (e.g., Beiler et al. 2024). However, for the majority of objects lacking such data, it is essential to combine multiple grids of atmospheric models to mitigate systematics and derive  $L_{\text{bol}}$  estimates with more conservative uncertainties (see Appendix A.2).

As an alternative approach for estimating  $L_{\text{bol}}$ , when observed spectrophotometry extends to longer wavelengths near or beyond the  $L$  and  $M$  bands, a Rayleigh-Jeans tail is often appended to the longest-wavelength flux to approximate the full SED (e.g., Leggett et al. 2001; Golimowski et al. 2004; Cushing et al. 2006; Zhang et al. 2020, 2022; Beiler et al. 2024). This method is significantly less complex than spectral fitting. However, when the observed spectrophotometry does not extend beyond the  $M$  band, these objects’ mid-infrared features such as  $\text{CH}_4$ ,  $\text{CO}$ , and silicate cloud absorption features can introduce significant deviations from the Rayleigh-Jeans approximation (e.g., Golimowski et al. 2004).

Additionally, for objects lacking spectroscopic data, bolometric corrections (BCs) are traditionally employed to estimate  $L_{\text{bol}}$  from broadband photometry, provided the objects’ distances are known. BCs are generally derived using empirical polynomials based on spectral types or single-band absolute magnitudes, calibrated using spectroscopic samples with bolometric luminosities estimated via the methods described above (e.g., Filippazzo et al. 2015; Dupuy & Liu 2017; Sanghi et al. 2023). This approach is technically straightforward to implement. While the bolometric luminosities estimated using BCs share some limitations with spectral fitting and the Rayleigh-Jeans approximation, the intrinsic scatter within large samples tends to increase the uncertainties of the estimated  $L_{\text{bol}}$ , helping to mitigate systematics associated with atmospheric models and Rayleigh-Jeans tails. However, these empirical polynomials are not well-established for objects with very young ages ( $\lesssim 100$  Myr) or extreme metallicities (e.g.,  $|[\text{M}/\text{H}]| > 0.5$  dex) due to the limited number of known objects in these parameter spaces.

Motivated by the challenges associated with existing methods for bolometric luminosity estimation, we propose a new approach with mitigated modeling systematics, tailored for objects with observed spectrophotometry. This approach is presented in the next section.

### A.2. A New Bolometric Correction Approach with Mitigated Modeling Systematics

Here, we present a new approach to determining the bolometric luminosities using the observed spectra of self-luminous exoplanets, brown dwarfs, and low-mass stars. Specifically, we define  $\text{specBC}_{\lambda\lambda}$  as the difference between the bolometric luminosity,  $\log(L_{\text{bol}}/L_{\odot})$ , and the integrated spectral luminosity over a narrower wavelength range ( $\lambda\lambda$ ),  $\log(L_{\lambda\lambda}/L_{\odot})$ , as follows,

$$\begin{aligned} \text{specBC}_{\lambda\lambda} &\equiv \log(L_{\text{bol}}/L_{\odot}) - \log(L_{\lambda\lambda}/L_{\odot}) \\ &\equiv \log(L_{\text{bol}}/L_{\odot}) - \log\left(4\pi d^2 \int_{\lambda\lambda} f_{\lambda} d\lambda / L_{\odot}\right) \end{aligned} \quad (\text{A1})$$

**Table 5.** Atmospheric Models and Parameter Space Investigated in Appendix A.2

Atmospheric Models	Parameters						Assumptions	
	$T_{\text{eff}}$ (K)	$\log(g)$ (dex)	[M/H] (dex)	C/O	Cloud Param.	$\log(K_{\text{zz}})$ (dex)	Clouds?	Chem. Eq?
ATMO2020	[400, 3000]	[2.5, 5.5]	0	0.55	–	multiple <sup>a</sup>	Cloudless	CEQ + NEQ
Sonora Diamondback	[900, 2400]	[3.5, 5.5]	[−0.5, +0.5]	0.458	$f_{\text{sed}} \in [1, 2, 3, 4, 8, \text{nc}]$	–	Cloudy	CEQ
Exo-REM	[400, 2000]	[3.0, 5.0]	[−0.5, +1.0]	[0.1, 0.8]	microphysics <sup>b</sup>	profiles <sup>b</sup>	Cloudy	CEQ + NEQ
SPHINX	[2000, 4000]	[4.0, 5.5]	[−1.0, +1.0]	[0.3, 0.9]	–	–	Cloudless	CEQ
BT-Settl	[1800, 4000]	[3.0, 5.5]	[−1.0, +0.5]	0.55	microphysics	–	Cloudy	CEQ

<sup>a</sup>The  $K_{\text{zz}}$  varies with the surface gravity in the ATMO2020 chemical disequilibrium models (see Figure 1 of Phillips et al. 2020).

<sup>b</sup>The Exo-REM models incorporate iron and silicate clouds. Also, the  $K_{\text{zz}}$  values are computed as a function of pressures (see Section 2.2.2 of Charnay et al. 2018).

For a given object with an observed spectrum ( $f_{\lambda}$ ) and a known distance ( $d$ ), once its corresponding  $\text{specBC}_{\lambda\lambda}$  is estimated, the bolometric luminosity can be derived as:

$$\log(L_{\text{bol}}/L_{\odot}) = \log\left(4\pi d^2 \int_{\lambda\lambda} f_{\lambda} d\lambda / L_{\odot}\right) + \text{specBC}_{\lambda\lambda} \quad (\text{A2})$$

For the rest of this section, we explain how to estimate  $\text{specBC}_{\lambda\lambda}$  for a given object. First, we present pre-calculated  $\text{specBC}_{\lambda\lambda}$  values over a wide parameter space. These  $\text{specBC}_{\lambda\lambda}$  values are computed using multiple grids of atmospheric models, including

- (1) ATMO2020 (Phillips et al. 2020),
- (2) Sonora Diamondback (Morley et al. 2024),
- (3) Exo-REM (Baudino et al. 2015; Charnay et al. 2018; Blain et al. 2021),
- (4) SPHINX (Iyer et al. 2023), and
- (5) BT-Settl (Allard et al. 2003, 2011, 2012, 2013)

The parameter space and key assumptions of these model grids are summarized in Table 5.

For each synthetic spectrum ( $F_{\lambda}$ ) in each of the above atmospheric model grids, we calculate the  $\text{specBC}_{\lambda\lambda} = \log(L_{\text{bol}}/L_{\lambda\lambda}) = \log[(\int_{\text{bol}} F_{\lambda} d\lambda) / (\int_{\lambda\lambda} F_{\lambda} d\lambda)]$ , where  $(\int_{\text{bol}} F_{\lambda} d\lambda)$  is the bolometric model flux integrated over the full wavelength range (up to 250  $\mu\text{m}$ ). For SPHINX models, which only extend to 20  $\mu\text{m}$ , we approximate the bolometric flux using  $\sigma_{\text{SB}} T_{\text{eff}}^4$ , where  $\sigma_{\text{SB}}$  is the Stefan-Boltzmann constant and  $T_{\text{eff}}$  is the effective temperature of the corresponding model spectrum. The term,  $(\int_{\lambda\lambda} F_{\lambda} d\lambda)$ , represents the integrated model flux over a pre-defined wavelength range. In this work, we explore three ranges based on the wavelength coverage of modern spectrographs:

- $\lambda\lambda = 1\text{--}2.4 \mu\text{m}$ , covered by ground-based near-infrared spectrographs, e.g., IRTF/SpeX (Rayner et al. 2003), Gemini-N/GNIRS (Elias et al. 2006), Gemini-S/FLAMINGOS-2 (Eikenberry et al. 2004, 2008), Magellan/FIRE (Simcoe et al. 2013), VLT/X-shooter (Vernet et al. 2011).
- $\lambda\lambda = 1\text{--}5 \mu\text{m}$ , covered by, e.g., JWST/NIRSpec (Jakobsen et al. 2022; Böker et al. 2023).
- $\lambda\lambda = 6\text{--}13 \mu\text{m}$ , covered by, e.g., JWST/MIRI (Rieke et al. 2015; Wright et al. 2023).

For JWST NIRSpec (0.6–5.3  $\mu\text{m}$ ) and MIRI (4.9–27.9  $\mu\text{m}$ ) spectrographs, we adopt slightly narrower wavelength ranges than their full wavelength sensitivities. This approach enhances the applicability of our methods across various observing modes while minimizing potential calibration uncertainties near detector edges.

Figure 22 summarizes our computed  $\text{specBC}_{\lambda\lambda}$  as a function of effective temperature for each atmospheric model grid. At a given  $T_{\text{eff}}$ , the value and errorbar of  $\text{specBC}_{\lambda\lambda}(T_{\text{eff}})$  represent the mean and the standard deviation of the computed bolometric

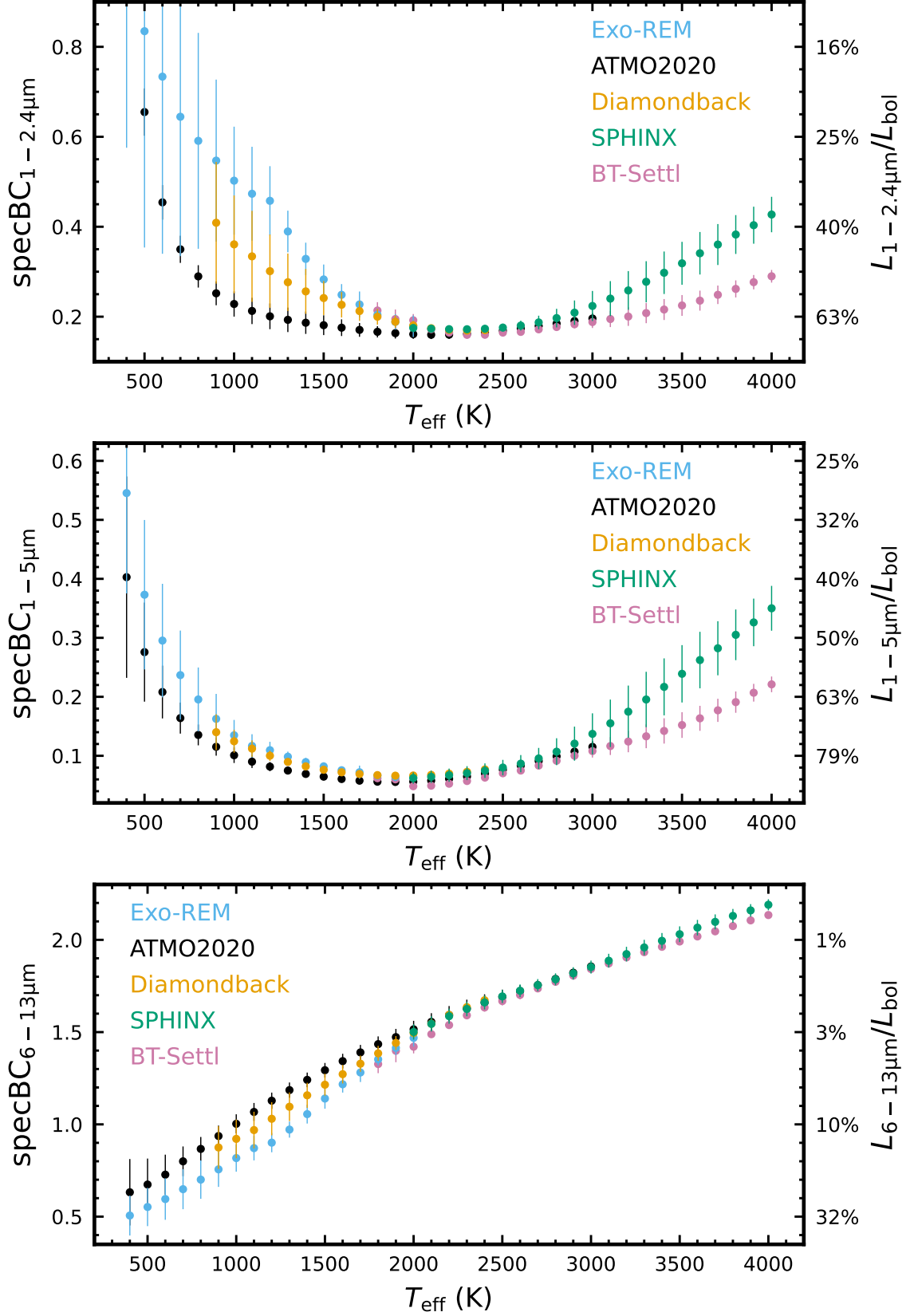


**Figure 22.** The bolometric correction ( $\text{specBC}_{\lambda\lambda}$ ; defined by Equation A1) for wavelength ranges of  $\lambda\lambda = 1 - 2.4 \mu\text{m}$  (top),  $1 - 5 \mu\text{m}$  (middle), and  $6 - 13 \mu\text{m}$  (bottom), calculated using multiple grids of atmospheric models. The y-axis on the right presents the ratio between the integrated spectral luminosity over  $\lambda\lambda$  and the bolometric luminosity,  $L_{\lambda\lambda}/L_{\text{bol}} = 10^{-\text{specBC}_{\lambda\lambda}}$ . These plotted values are summarized in Tables 6, 7, and 8.

correction for all model spectra with the same  $T_{\text{eff}}$  but varying  $\log(g)$ ,  $[M/H]$ ,  $C/O$ , and cloud properties. The pre-computed  $\text{specBC}_{\lambda\lambda}$  for each  $\lambda\lambda$  and model grid are provided in Tables 6, 7, and 8.

With these pre-computed  $\text{specBC}_{\lambda\lambda}$  values, one can estimate the bolometric correction term for a given object by computing the mean and standard deviation of the  $\text{specBC}_{\lambda\lambda}$  values over a customized  $\{T_{\text{eff}}, \log(g), [M/H], \text{CO}\}$  parameter space relevant to the object (see Section 4.1) and then compute the bolometric luminosity via Equation A2.

The bolometric correction approach presented in this work is applicable for objects with  $T_{\text{eff}}$  from 400 K to 4000 K,  $\log(g)$ . Our analysis also shows that the bolometric correction is highly model-dependent, except for objects with specific  $T_{\text{eff}}$  ranges. For objects with 1–2.4  $\mu\text{m}$  spectra, various model grids yield consistent  $\text{specBC}_{1-2.4\mu\text{m}}$  over  $T_{\text{eff}} = 1900 - 3200$  K; for objects with 1–5  $\mu\text{m}$  spectra, various model grids yield consistent  $\text{specBC}_{1-5\mu\text{m}}$  for  $T_{\text{eff}} = 900 - 3200$  K. Outside these  $T_{\text{eff}}$  ranges, the systematic differences between model grids are much larger than the scatter within each model grid. In this situation, we recommend incorporating a large uncertainty in  $\text{specBC}_{\lambda\lambda}$  to account for the modeling systematics.

**Table 6.** Spectroscopy-based bolometric correction for  $\lambda\lambda = 1 - 2.4 \mu\text{m}$ , i.e.,  $\text{specBC}_{1-2.4\mu\text{m}} = \log(L_{\text{bol}}/L_{\odot}) - \log(L_{1-2.4\mu\text{m}}/L_{\odot})$ 

$T_{\text{eff}}$ (K)	Exo-REM		Diamondback		ATMO2020		BT-Settl		SPHINX	
	Value (dex)	$N_{\text{model}}$								
400	1.169 ± 0.593	293	...	...	1.132 ± 0.085	21	...	...	...	...
500	0.835 ± 0.481	283	...	...	0.655 ± 0.053	20	...	...	...	...
600	0.734 ± 0.394	294	...	...	0.454 ± 0.038	21	...	...	...	...
700	0.645 ± 0.310	289	...	...	0.350 ± 0.030	20	...	...	...	...
800	0.591 ± 0.240	289	...	...	0.290 ± 0.025	21	...	...	...	...
900	0.547 ± 0.180	294	0.409 ± 0.135	90	0.252 ± 0.027	21	...	...	...	...
1000	0.502 ± 0.120	292	0.361 ± 0.109	90	0.228 ± 0.028	21	...	...	...	...
1100	0.473 ± 0.104	287	0.334 ± 0.101	90	0.213 ± 0.029	20	...	...	...	...
1200	0.458 ± 0.077	290	0.301 ± 0.081	90	0.201 ± 0.029	21	...	...	...	...
1300	0.389 ± 0.046	290	0.277 ± 0.064	90	0.193 ± 0.027	21	...	...	...	...
1400	0.329 ± 0.036	285	0.256 ± 0.050	90	0.187 ± 0.025	21	...	...	...	...
1500	0.283 ± 0.033	284	0.241 ± 0.038	90	0.181 ± 0.022	21	...	...	...	...
1600	0.249 ± 0.024	293	0.226 ± 0.028	90	0.176 ± 0.019	21	...	...	...	...
1700	0.227 ± 0.029	290	0.212 ± 0.022	90	0.171 ± 0.015	21	...	...	...	...
1800	0.204 ± 0.014	291	0.200 ± 0.018	90	0.166 ± 0.013	21	0.214 ± 0.018	25	...	...
1900	0.188 ± 0.017	294	0.189 ± 0.014	90	0.163 ± 0.012	7	0.195 ± 0.021	25	...	...
2000	0.179 ± 0.024	294	0.180 ± 0.010	90	0.161 ± 0.010	7	0.192 ± 0.014	30	0.175 ± 0.006	252
2100	...	...	0.174 ± 0.008	90	0.160 ± 0.010	7	0.172 ± 0.003	30	0.173 ± 0.005	252
2200	...	...	0.171 ± 0.006	90	0.160 ± 0.009	7	0.165 ± 0.003	30	0.172 ± 0.005	252
2300	...	...	0.169 ± 0.004	90	0.162 ± 0.009	7	0.160 ± 0.004	30	0.172 ± 0.006	252
2400	...	...	0.170 ± 0.003	90	0.165 ± 0.009	7	0.160 ± 0.005	30	0.173 ± 0.007	252
2500	...	...	...	...	0.169 ± 0.008	7	0.165 ± 0.006	30	0.176 ± 0.009	252
2600	...	...	...	...	0.174 ± 0.007	7	0.166 ± 0.006	18	0.180 ± 0.011	252
2700	...	...	...	...	0.179 ± 0.005	7	0.172 ± 0.005	18	0.187 ± 0.015	252
2800	...	...	...	...	0.185 ± 0.005	7	0.177 ± 0.006	18	0.197 ± 0.021	251
2900	...	...	...	...	0.190 ± 0.008	7	0.183 ± 0.009	18	0.209 ± 0.027	252
3000	...	...	...	...	0.196 ± 0.012	7	0.188 ± 0.013	18	0.224 ± 0.033	250
3100	...	...	...	...	...	...	0.195 ± 0.018	18	0.240 ± 0.039	252
3200	...	...	...	...	...	...	0.200 ± 0.021	18	0.258 ± 0.043	252
3300	...	...	...	...	...	...	0.208 ± 0.022	18	0.278 ± 0.046	252
3400	...	...	...	...	...	...	0.216 ± 0.023	18	0.298 ± 0.047	251
3500	...	...	...	...	...	...	0.225 ± 0.023	18	0.319 ± 0.048	246
3600	...	...	...	...	...	...	0.236 ± 0.022	18	0.341 ± 0.047	237
3700	...	...	...	...	...	...	0.249 ± 0.021	18	0.360 ± 0.046	245
3800	...	...	...	...	...	...	0.262 ± 0.019	18	0.383 ± 0.043	241
3900	...	...	...	...	...	...	0.277 ± 0.016	18	0.403 ± 0.041	247
4000	...	...	...	...	...	...	0.290 ± 0.014	18	0.427 ± 0.039	248

**Table 7.** Spectroscopy-based bolometric correction for  $\lambda\lambda = 1 - 5 \mu\text{m}$ , i.e.,  $\text{specBC}_{1-5\mu\text{m}} = \log(L_{\text{bol}}/L_{\odot}) - \log(L_{1-5\mu\text{m}}/L_{\odot})$ 

$T_{\text{eff}}$ (K)	Exo-REM		Diamondback		ATMO2020		BT-Settl		SPHINX	
	Value (dex)	$N_{\text{model}}$								
400	0.545 ± 0.170	293	...	...	0.403 ± 0.171	21	...	...	...	...
500	0.373 ± 0.127	283	...	...	0.276 ± 0.084	20	...	...	...	...
600	0.295 ± 0.096	294	...	...	0.208 ± 0.045	21	...	...	...	...
700	0.237 ± 0.075	289	...	...	0.164 ± 0.026	20	...	...	...	...
800	0.196 ± 0.054	289	...	...	0.135 ± 0.018	21	...	...	...	...
900	0.163 ± 0.042	294	0.140 ± 0.030	90	0.115 ± 0.015	21	...	...	...	...
1000	0.135 ± 0.026	292	0.125 ± 0.019	90	0.101 ± 0.013	21	...	...	...	...
1100	0.117 ± 0.020	287	0.112 ± 0.014	90	0.090 ± 0.011	20	...	...	...	...
1200	0.110 ± 0.014	290	0.100 ± 0.009	90	0.082 ± 0.008	21	...	...	...	...
1300	0.098 ± 0.009	290	0.090 ± 0.006	90	0.075 ± 0.005	21	...	...	...	...
1400	0.089 ± 0.007	285	0.082 ± 0.004	90	0.069 ± 0.003	21	...	...	...	...
1500	0.082 ± 0.007	284	0.076 ± 0.004	90	0.065 ± 0.002	21	...	...	...	...
1600	0.076 ± 0.006	293	0.072 ± 0.003	90	0.061 ± 0.001	21	...	...	...	...
1700	0.072 ± 0.011	290	0.069 ± 0.003	90	0.058 ± 0.001	21	...	...	...	...
1800	0.067 ± 0.007	291	0.067 ± 0.003	90	0.056 ± 0.001	21	0.062 ± 0.003	25	...	...
1900	0.064 ± 0.007	294	0.066 ± 0.003	90	0.056 ± 0.001	7	0.060 ± 0.003	25	...	...
2000	0.063 ± 0.008	294	0.067 ± 0.003	90	0.056 ± 0.000	7	0.048 ± 0.001	30	0.062 ± 0.010	252
2100	...	...	0.068 ± 0.003	90	0.058 ± 0.000	7	0.049 ± 0.002	30	0.064 ± 0.010	252
2200	...	...	0.070 ± 0.003	90	0.061 ± 0.000	7	0.053 ± 0.002	30	0.067 ± 0.011	252
2300	...	...	0.073 ± 0.004	90	0.065 ± 0.000	7	0.057 ± 0.001	30	0.071 ± 0.012	252
2400	...	...	0.077 ± 0.004	90	0.070 ± 0.001	7	0.063 ± 0.001	30	0.075 ± 0.012	252
2500	...	...	...	...	0.076 ± 0.001	7	0.070 ± 0.001	30	0.080 ± 0.013	252
2600	...	...	...	...	0.083 ± 0.001	7	0.075 ± 0.002	18	0.087 ± 0.015	252
2700	...	...	...	...	0.091 ± 0.002	7	0.083 ± 0.003	18	0.096 ± 0.018	252
2800	...	...	...	...	0.099 ± 0.004	7	0.092 ± 0.005	18	0.107 ± 0.023	251
2900	...	...	...	...	0.107 ± 0.007	7	0.100 ± 0.007	18	0.121 ± 0.029	252
3000	...	...	...	...	0.115 ± 0.010	7	0.108 ± 0.011	18	0.137 ± 0.035	250
3100	...	...	...	...	...	...	0.117 ± 0.015	18	0.155 ± 0.040	252
3200	...	...	...	...	...	...	0.124 ± 0.018	18	0.175 ± 0.044	252
3300	...	...	...	...	...	...	0.133 ± 0.020	18	0.195 ± 0.047	252
3400	...	...	...	...	...	...	0.142 ± 0.021	18	0.217 ± 0.048	251
3500	...	...	...	...	...	...	0.152 ± 0.022	18	0.239 ± 0.049	246
3600	...	...	...	...	...	...	0.164 ± 0.021	18	0.262 ± 0.048	237
3700	...	...	...	...	...	...	0.177 ± 0.020	18	0.282 ± 0.046	245
3800	...	...	...	...	...	...	0.191 ± 0.018	18	0.305 ± 0.043	241
3900	...	...	...	...	...	...	0.207 ± 0.015	18	0.326 ± 0.040	247
4000	...	...	...	...	...	...	0.221 ± 0.013	18	0.350 ± 0.038	248

**Table 8.** Spectroscopy-based bolometric correction for  $\lambda\lambda = 6 - 13 \mu\text{m}$ , i.e.,  $\text{specBC}_{6-13\mu\text{m}} = \log(L_{\text{bol}}/L_{\odot}) - \log(L_{6-13\mu\text{m}}/L_{\odot})$ 

$T_{\text{eff}}$ (K)	Exo-REM		Diamondback		ATMO2020		BT-Settl		SPHINX	
	Value (dex)	$N_{\text{model}}$								
400	$0.506 \pm 0.108$	293	...	...	$0.632 \pm 0.180$	21	...	...	...	...
500	$0.552 \pm 0.104$	283	...	...	$0.674 \pm 0.141$	20	...	...	...	...
600	$0.595 \pm 0.112$	294	...	...	$0.728 \pm 0.108$	21	...	...	...	...
700	$0.649 \pm 0.108$	289	...	...	$0.800 \pm 0.081$	20	...	...	...	...
800	$0.701 \pm 0.104$	289	...	...	$0.867 \pm 0.065$	21	...	...	...	...
900	$0.756 \pm 0.095$	294	$0.875 \pm 0.116$	90	$0.937 \pm 0.056$	21	...	...	...	...
1000	$0.817 \pm 0.074$	292	$0.921 \pm 0.105$	90	$1.003 \pm 0.052$	21	...	...	...	...
1100	$0.871 \pm 0.066$	287	$0.969 \pm 0.099$	90	$1.067 \pm 0.049$	20	...	...	...	...
1200	$0.901 \pm 0.052$	290	$1.030 \pm 0.090$	90	$1.128 \pm 0.044$	21	...	...	...	...
1300	$0.972 \pm 0.044$	290	$1.095 \pm 0.078$	90	$1.186 \pm 0.041$	21	...	...	...	...
1400	$1.056 \pm 0.051$	285	$1.157 \pm 0.068$	90	$1.241 \pm 0.040$	21	...	...	...	...
1500	$1.140 \pm 0.055$	284	$1.215 \pm 0.060$	90	$1.294 \pm 0.039$	21	...	...	...	...
1600	$1.217 \pm 0.045$	293	$1.272 \pm 0.050$	90	$1.343 \pm 0.040$	21	...	...	...	...
1700	$1.281 \pm 0.052$	290	$1.329 \pm 0.044$	90	$1.390 \pm 0.041$	21	...	...	...	...
1800	$1.352 \pm 0.033$	291	$1.385 \pm 0.040$	90	$1.435 \pm 0.042$	21	$1.327 \pm 0.049$	25	...	...
1900	$1.415 \pm 0.039$	294	$1.441 \pm 0.037$	90	$1.473 \pm 0.045$	7	$1.399 \pm 0.062$	25	...	...
2000	$1.469 \pm 0.047$	294	$1.495 \pm 0.031$	90	$1.515 \pm 0.046$	7	$1.421 \pm 0.036$	30	$1.501 \pm 0.041$	252
2100	...	...	$1.546 \pm 0.028$	90	$1.556 \pm 0.047$	7	$1.489 \pm 0.017$	30	$1.545 \pm 0.041$	252
2200	...	...	$1.593 \pm 0.027$	90	$1.593 \pm 0.048$	7	$1.538 \pm 0.010$	30	$1.586 \pm 0.041$	252
2300	...	...	$1.635 \pm 0.026$	90	$1.628 \pm 0.048$	7	$1.591 \pm 0.018$	30	$1.626 \pm 0.039$	252
2400	...	...	$1.673 \pm 0.027$	90	$1.660 \pm 0.045$	7	$1.634 \pm 0.022$	30	$1.661 \pm 0.038$	252
2500	...	...	...	...	$1.691 \pm 0.039$	7	$1.668 \pm 0.024$	30	$1.693 \pm 0.036$	252
2600	...	...	...	...	$1.722 \pm 0.033$	7	$1.702 \pm 0.023$	18	$1.724 \pm 0.034$	252
2700	...	...	...	...	$1.755 \pm 0.026$	7	$1.737 \pm 0.019$	18	$1.754 \pm 0.033$	252
2800	...	...	...	...	$1.788 \pm 0.019$	7	$1.773 \pm 0.015$	18	$1.786 \pm 0.032$	251
2900	...	...	...	...	$1.822 \pm 0.014$	7	$1.806 \pm 0.011$	18	$1.818 \pm 0.033$	252
3000	...	...	...	...	$1.856 \pm 0.010$	7	$1.842 \pm 0.007$	18	$1.852 \pm 0.035$	250
3100	...	...	...	...	...	...	$1.872 \pm 0.007$	18	$1.887 \pm 0.037$	252
3200	...	...	...	...	...	...	$1.905 \pm 0.005$	18	$1.923 \pm 0.040$	252
3300	...	...	...	...	...	...	$1.933 \pm 0.006$	18	$1.959 \pm 0.041$	252
3400	...	...	...	...	...	...	$1.962 \pm 0.006$	18	$1.995 \pm 0.042$	251
3500	...	...	...	...	...	...	$1.991 \pm 0.006$	18	$2.031 \pm 0.043$	246
3600	...	...	...	...	...	...	$2.019 \pm 0.006$	18	$2.066 \pm 0.042$	237
3700	...	...	...	...	...	...	$2.046 \pm 0.006$	18	$2.097 \pm 0.040$	245
3800	...	...	...	...	...	...	$2.075 \pm 0.005$	18	$2.130 \pm 0.038$	241
3900	...	...	...	...	...	...	$2.106 \pm 0.006$	18	$2.160 \pm 0.034$	247
4000	...	...	...	...	...	...	$2.134 \pm 0.005$	18	$2.190 \pm 0.030$	248

## REFERENCES

- Ackerman, A. S., & Marley, M. S. 2001, *ApJ*, 556, 872, doi: [10.1086/321540](https://doi.org/10.1086/321540)
- Allard, F., Guillot, T., Ludwig, H.-G., et al. 2003, in *Brown Dwarfs*, ed. E. Martín, Vol. 211, 325
- Allard, F., Hauschildt, P. H., Alexander, D. R., & Starrfield, S. 1997, *ARA&A*, 35, 137, doi: [10.1146/annurev.astro.35.1.137](https://doi.org/10.1146/annurev.astro.35.1.137)
- Allard, F., Homeier, D., & Freytag, B. 2011, in *Astronomical Society of the Pacific Conference Series*, Vol. 448, 16th Cambridge Workshop on Cool Stars, Stellar Systems, and the Sun, ed. C. Johns-Krull, M. K. Browning, & A. A. West, 91, doi: [10.48550/arXiv.1011.5405](https://doi.org/10.48550/arXiv.1011.5405)
- Allard, F., Homeier, D., & Freytag, B. 2012, *Philosophical Transactions of the Royal Society of London Series A*, 370, 2765, doi: [10.1098/rsta.2011.0269](https://doi.org/10.1098/rsta.2011.0269)
- Allard, F., Homeier, D., Freytag, B., Schaffenberger, W., & Rajpurohit, A. S. 2013, *Memorie della Societa Astronomica Italiana Supplementi*, 24, 128, doi: [10.48550/arXiv.1302.6559](https://doi.org/10.48550/arXiv.1302.6559)
- Allard, N. F., Spiegelman, F., & Kielkopf, J. F. 2016, *A&A*, 589, A21, doi: [10.1051/0004-6361/201628270](https://doi.org/10.1051/0004-6361/201628270)
- Allard, N. F., Spiegelman, F., Leininger, T., & Molliere, P. 2019, *A&A*, 628, A120, doi: [10.1051/0004-6361/201935593](https://doi.org/10.1051/0004-6361/201935593)
- Allers, K. N., & Liu, M. C. 2013, *ApJ*, 772, 79, doi: [10.1088/0004-637X/772/2/79](https://doi.org/10.1088/0004-637X/772/2/79)
- Ammler-von Eiff, M., & Guenther, E. W. 2009, *A&A*, 508, 677, doi: [10.1051/0004-6361/200912660](https://doi.org/10.1051/0004-6361/200912660)
- Aoyama, Y., Marleau, G.-D., & Hashimoto, J. 2024, *AJ*, 168, 155, doi: [10.3847/1538-3881/ad67df](https://doi.org/10.3847/1538-3881/ad67df)
- Apai, D., Radigan, J., Buenzli, E., et al. 2013, *ApJ*, 768, 121, doi: [10.1088/0004-637X/768/2/121](https://doi.org/10.1088/0004-637X/768/2/121)
- Apai, D., Karalidi, T., Marley, M. S., et al. 2017, *Science*, 357, 683, doi: [10.1126/science.aam9848](https://doi.org/10.1126/science.aam9848)
- Artigau, É., Bouchard, S., Doyon, R., & Lafrenière, D. 2009, *ApJ*, 701, 1534, doi: [10.1088/0004-637X/701/2/1534](https://doi.org/10.1088/0004-637X/701/2/1534)
- Astropy Collaboration, Robitaille, T. P., Tollerud, E. J., et al. 2013, *A&A*, 558, A33, doi: [10.1051/0004-6361/201322068](https://doi.org/10.1051/0004-6361/201322068)
- Astropy Collaboration, Price-Whelan, A. M., Sipőcz, B. M., et al. 2018, *AJ*, 156, 123, doi: [10.3847/1538-3881/aabc4f](https://doi.org/10.3847/1538-3881/aabc4f)
- Azzam, A. A. A., Tennyson, J., Yurchenko, S. N., & Naumenko, O. V. 2016, *MNRAS*, 460, 4063, doi: [10.1093/mnras/stw1133](https://doi.org/10.1093/mnras/stw1133)
- Bailer-Jones, C. A. L., Rybizki, J., Fouesneau, M., Demleitner, M., & Andrae, R. 2021, *AJ*, 161, 147, doi: [10.3847/1538-3881/abd806](https://doi.org/10.3847/1538-3881/abd806)
- Balmer, W. O., Franson, K., Chomez, A., et al. 2024, *arXiv e-prints*, arXiv:2411.05917, doi: [10.48550/arXiv.2411.05917](https://doi.org/10.48550/arXiv.2411.05917)
- Baraffe, I., Chabrier, G., Barman, T. S., Allard, F., & Hauschildt, P. H. 2003, *A&A*, 402, 701, doi: [10.1051/0004-6361:20030252](https://doi.org/10.1051/0004-6361:20030252)
- Barman, T. S., Macintosh, B., Konopacky, Q. M., & Marois, C. 2011a, *ApJL*, 735, L39, doi: [10.1088/2041-8205/735/2/L39](https://doi.org/10.1088/2041-8205/735/2/L39)
- . 2011b, *ApJ*, 733, 65, doi: [10.1088/0004-637X/733/1/65](https://doi.org/10.1088/0004-637X/733/1/65)
- Barrado, D., Mollière, P., Patapis, P., et al. 2023, *Nature*, 624, 263, doi: [10.1038/s41586-023-06813-y](https://doi.org/10.1038/s41586-023-06813-y)
- Barrado Y Navascués, D. 2006, *A&A*, 459, 511, doi: [10.1051/0004-6361:20065717](https://doi.org/10.1051/0004-6361:20065717)
- Baudino, J. L., Bézard, B., Boccaletti, A., et al. 2015, *A&A*, 582, A83, doi: [10.1051/0004-6361/201526332](https://doi.org/10.1051/0004-6361/201526332)
- Beiler, S. A., Cushing, M. C., Kirkpatrick, J. D., et al. 2024, *ApJ*, 973, 107, doi: [10.3847/1538-4357/ad6301](https://doi.org/10.3847/1538-4357/ad6301)
- Belton, M. J. S., Head, J. W., I., Ingersoll, A. P., et al. 1996, *Science*, 274, 377, doi: [10.1126/science.274.5286.377](https://doi.org/10.1126/science.274.5286.377)
- Bernath, P. F. 2020, *JQSRT*, 240, 106687, doi: [10.1016/j.jqsrt.2019.106687](https://doi.org/10.1016/j.jqsrt.2019.106687)
- Biazzo, K., Alcalá, J. M., Covino, E., et al. 2012a, *A&A*, 547, A104, doi: [10.1051/0004-6361/201219680](https://doi.org/10.1051/0004-6361/201219680)
- Biazzo, K., D'Orazi, V., Desidera, S., et al. 2012b, *MNRAS*, 427, 2905, doi: [10.1111/j.1365-2966.2012.22132.x](https://doi.org/10.1111/j.1365-2966.2012.22132.x)
- Biazzo, K., Randich, S., Palla, F., & Briceño, C. 2011, *A&A*, 530, A19, doi: [10.1051/0004-6361/201116621](https://doi.org/10.1051/0004-6361/201116621)
- Biazzo, K., Frasca, A., Alcalá, J. M., et al. 2017, *A&A*, 605, A66, doi: [10.1051/0004-6361/201730850](https://doi.org/10.1051/0004-6361/201730850)
- Billler, B. A., & Close, L. M. 2007, *ApJL*, 669, L41, doi: [10.1086/523799](https://doi.org/10.1086/523799)
- Billler, B. A., Vos, J. M., Zhou, Y., et al. 2024, *MNRAS*, 532, 2207, doi: [10.1093/mnras/stae1602](https://doi.org/10.1093/mnras/stae1602)
- Blain, D., Charnay, B., & Bézard, B. 2021, *A&A*, 646, A15, doi: [10.1051/0004-6361/202039072](https://doi.org/10.1051/0004-6361/202039072)
- Blunt, S., Nielsen, E. L., De Rosa, R. J., et al. 2017, *AJ*, 153, 229, doi: [10.3847/1538-3881/aa6930](https://doi.org/10.3847/1538-3881/aa6930)
- Böker, T., Beck, T. L., Birkmann, S. M., et al. 2023, *PASP*, 135, 038001, doi: [10.1088/1538-3873/acb846](https://doi.org/10.1088/1538-3873/acb846)
- Boley, A. C., & Durisen, R. H. 2010, *ApJ*, 724, 618, doi: [10.1088/0004-637X/724/1/618](https://doi.org/10.1088/0004-637X/724/1/618)
- Borysow, A. 2002, *A&A*, 390, 779, doi: [10.1051/0004-6361:20020555](https://doi.org/10.1051/0004-6361:20020555)
- Borysow, A., & Frommhold, L. 1989, *ApJ*, 341, 549, doi: [10.1086/167515](https://doi.org/10.1086/167515)
- Borysow, A., Frommhold, L., & Moraldi, M. 1989, *ApJ*, 336, 495, doi: [10.1086/167027](https://doi.org/10.1086/167027)
- Borysow, A., Jorgensen, U. G., & Fu, Y. 2001, *JQSRT*, 68, 235, doi: [10.1016/S0022-4073\(00\)00023-6](https://doi.org/10.1016/S0022-4073(00)00023-6)
- Borysow, J., Frommhold, L., & Birnbaum, G. 1988, *ApJ*, 326, 509, doi: [10.1086/166112](https://doi.org/10.1086/166112)
- Boss, A. P. 2006, *ApJL*, 637, L137, doi: [10.1086/500613](https://doi.org/10.1086/500613)
- Bouy, H., Martín, E. L., Cuillandre, J. C., et al. 2025, *arXiv e-prints*, arXiv:2502.16349, doi: [10.48550/arXiv.2502.16349](https://doi.org/10.48550/arXiv.2502.16349)
- Bowler, B. P., Liu, M. C., Dupuy, T. J., & Cushing, M. C. 2010, *ApJ*, 723, 850, doi: [10.1088/0004-637X/723/1/850](https://doi.org/10.1088/0004-637X/723/1/850)
- Brown-Sevilla, S. B., Maire, A. L., Mollière, P., et al. 2023, *A&A*, 673, A98, doi: [10.1051/0004-6361/202244826](https://doi.org/10.1051/0004-6361/202244826)

- Buchner, J., Georgakakis, A., Nandra, K., et al. 2014, *A&A*, 564, A125, doi: [10.1051/0004-6361/201322971](https://doi.org/10.1051/0004-6361/201322971)
- Burgasser, A. J., Marley, M. S., Ackerman, A. S., et al. 2002, *ApJL*, 571, L151, doi: [10.1086/341343](https://doi.org/10.1086/341343)
- Burgasser, A. J., & McElwain, M. W. 2006, *AJ*, 131, 1007, doi: [10.1086/499042](https://doi.org/10.1086/499042)
- Burningham, B., Marley, M. S., Line, M. R., et al. 2017, *MNRAS*, 470, 1177, doi: [10.1093/mnras/stx1246](https://doi.org/10.1093/mnras/stx1246)
- Burrows, A., Hubbard, W. B., Lunine, J. I., & Liebert, J. 2001, *Reviews of Modern Physics*, 73, 719, doi: [10.1103/RevModPhys.73.719](https://doi.org/10.1103/RevModPhys.73.719)
- Burrows, A., Marley, M., Hubbard, W. B., et al. 1997, *ApJ*, 491, 856, doi: [10.1086/305002](https://doi.org/10.1086/305002)
- Chabrier, G., Baraffe, I., Allard, F., & Hauschildt, P. 2000, *ApJ*, 542, 464, doi: [10.1086/309513](https://doi.org/10.1086/309513)
- Chabrier, G., Baraffe, I., Phillips, M., & Debras, F. 2023, *A&A*, 671, A119, doi: [10.1051/0004-6361/202243832](https://doi.org/10.1051/0004-6361/202243832)
- Chan, Y. M., & Dalgarno, A. 1965, *Proceedings of the Physical Society*, 85, 227, doi: [10.1088/0370-1328/85/2/304](https://doi.org/10.1088/0370-1328/85/2/304)
- Charnay, B., Bézard, B., Baudino, J. L., et al. 2018, *ApJ*, 854, 172, doi: [10.3847/1538-4357/aaac7d](https://doi.org/10.3847/1538-4357/aaac7d)
- Chauvin, G., Lagrange, A. M., Dumas, C., et al. 2004, *A&A*, 425, L29, doi: [10.1051/0004-6361:200400056](https://doi.org/10.1051/0004-6361:200400056)
- . 2005, *A&A*, 438, L25, doi: [10.1051/0004-6361:200500116](https://doi.org/10.1051/0004-6361:200500116)
- Coles, P. A., Yurchenko, S. N., & Tennyson, J. 2019, *MNRAS*, 490, 4638, doi: [10.1093/mnras/stz2778](https://doi.org/10.1093/mnras/stz2778)
- Currie, T., Biller, B., Lagrange, A., et al. 2023, in *Astronomical Society of the Pacific Conference Series*, Vol. 534, *Protostars and Planets VII*, ed. S. Inutsuka, Y. Aikawa, T. Muto, K. Tomida, & M. Tamura, 799, doi: [10.48550/arXiv.2205.05696](https://doi.org/10.48550/arXiv.2205.05696)
- Currie, T., Burrows, A., Itoh, Y., et al. 2011, *ApJ*, 729, 128, doi: [10.1088/0004-637X/729/2/128](https://doi.org/10.1088/0004-637X/729/2/128)
- Cushing, M. C., Roellig, T. L., Marley, M. S., et al. 2006, *ApJ*, 648, 614, doi: [10.1086/505637](https://doi.org/10.1086/505637)
- Czekala, I., Andrews, S. M., Mandel, K. S., Hogg, D. W., & Green, G. M. 2015, *ApJ*, 812, 128, doi: [10.1088/0004-637X/812/2/128](https://doi.org/10.1088/0004-637X/812/2/128)
- Dalgarno, A., & Williams, D. A. 1962, *ApJ*, 136, 690, doi: [10.1086/147428](https://doi.org/10.1086/147428)
- de Regt, S., Gandhi, S., Snellen, I. A. G., et al. 2024, *A&A*, 688, A116, doi: [10.1051/0004-6361/202348508](https://doi.org/10.1051/0004-6361/202348508)
- Dittmann, A. 2024, *The Open Journal of Astrophysics*, 7, 79, doi: [10.33232/001c.123872](https://doi.org/10.33232/001c.123872)
- Donaldson, J. K., Weinberger, A. J., Gagné, J., et al. 2016, *ApJ*, 833, 95, doi: [10.3847/1538-4357/833/1/95](https://doi.org/10.3847/1538-4357/833/1/95)
- D’Orazi, V., Biazzo, K., & Randich, S. 2011, *A&A*, 526, A103, doi: [10.1051/0004-6361/201015616](https://doi.org/10.1051/0004-6361/201015616)
- Ducourant, C., Teixeira, R., Chauvin, G., et al. 2008, *A&A*, 477, L1, doi: [10.1051/0004-6361:20078886](https://doi.org/10.1051/0004-6361:20078886)
- Dulick, M., Bauschlicher, C. W., J., Burrows, A., et al. 2003, *ApJ*, 594, 651, doi: [10.1086/376791](https://doi.org/10.1086/376791)
- Dupuy, T. J., & Liu, M. C. 2017, *ApJS*, 231, 15, doi: [10.3847/1538-4365/aa5e4c](https://doi.org/10.3847/1538-4365/aa5e4c)
- Dupuy, T. J., Liu, M. C., Evans, E. L., et al. 2023, *MNRAS*, 519, 1688, doi: [10.1093/mnras/stac3557](https://doi.org/10.1093/mnras/stac3557)
- Eikenberry, S., Elston, R., Raines, S. N., et al. 2008, in *Society of Photo-Optical Instrumentation Engineers (SPIE) Conference Series*, Vol. 7014, *Ground-based and Airborne Instrumentation for Astronomy II*, ed. I. S. McLean & M. M. Casali, 70140V, doi: [10.1117/12.788326](https://doi.org/10.1117/12.788326)
- Eikenberry, S. S., Elston, R., Raines, S. N., et al. 2004, in *Society of Photo-Optical Instrumentation Engineers (SPIE) Conference Series*, Vol. 5492, *Ground-based Instrumentation for Astronomy*, ed. A. F. M. Moorwood & M. Iye, 1196–1207, doi: [10.1117/12.549796](https://doi.org/10.1117/12.549796)
- Elias, J. H., Joyce, R. R., Liang, M., et al. 2006, in *Society of Photo-Optical Instrumentation Engineers (SPIE) Conference Series*, Vol. 6269, *Ground-based and Airborne Instrumentation for Astronomy*, ed. I. S. McLean & M. Iye, 62694C, doi: [10.1117/12.671817](https://doi.org/10.1117/12.671817)
- Feroz, F., & Hobson, M. P. 2008, *MNRAS*, 384, 449, doi: [10.1111/j.1365-2966.2007.12353.x](https://doi.org/10.1111/j.1365-2966.2007.12353.x)
- Feroz, F., Hobson, M. P., & Bridges, M. 2009, *MNRAS*, 398, 1601, doi: [10.1111/j.1365-2966.2009.14548.x](https://doi.org/10.1111/j.1365-2966.2009.14548.x)
- Feroz, F., Hobson, M. P., Cameron, E., & Pettitt, A. N. 2019, *The Open Journal of Astrophysics*, 2, 10, doi: [10.21105/astro.1306.2144](https://doi.org/10.21105/astro.1306.2144)
- Filippazzo, J. C., Rice, E. L., Faherty, J., et al. 2015, *ApJ*, 810, 158, doi: [10.1088/0004-637X/810/2/158](https://doi.org/10.1088/0004-637X/810/2/158)
- Fletcher, L. N., Kaspi, Y., Guillot, T., & Showman, A. P. 2020, *SSRv*, 216, 30, doi: [10.1007/s11214-019-0631-9](https://doi.org/10.1007/s11214-019-0631-9)
- Fletcher, L. N., Oyafuso, F. A., Allison, M., et al. 2021, *Journal of Geophysical Research (Planets)*, 126, e06858, doi: [10.1029/2021JE006858](https://doi.org/10.1029/2021JE006858)
- Foreman-Mackey, D. 2016, *The Journal of Open Source Software*, 1, 24, doi: [10.21105/joss.00024](https://doi.org/10.21105/joss.00024)
- Foreman-Mackey, D., Hogg, D. W., Lang, D., & Goodman, J. 2013, *PASP*, 125, 306, doi: [10.1086/670067](https://doi.org/10.1086/670067)
- Fortney, J. J. 2018, *arXiv e-prints*, arXiv:1804.08149, doi: [10.48550/arXiv.1804.08149](https://doi.org/10.48550/arXiv.1804.08149)
- Fortney, J. J., Visscher, C., Marley, M. S., et al. 2020, *AJ*, 160, 288, doi: [10.3847/1538-3881/abc5bd](https://doi.org/10.3847/1538-3881/abc5bd)
- France, K., Linsky, J. L., Brown, A., Froning, C. S., & Béland, S. 2010, *ApJ*, 715, 596, doi: [10.1088/0004-637X/715/1/596](https://doi.org/10.1088/0004-637X/715/1/596)
- Fuda, N., & Apai, D. 2024, *ApJL*, 975, L32, doi: [10.3847/2041-8213/ad87e9](https://doi.org/10.3847/2041-8213/ad87e9)
- Gandhi, S., de Regt, S., Snellen, I., et al. 2023, *ApJL*, 957, L36, doi: [10.3847/2041-8213/ad07e2](https://doi.org/10.3847/2041-8213/ad07e2)
- Gapp, C., Rengel, M., Hartogh, P., et al. 2024, *A&A*, 688, A10, doi: [10.1051/0004-6361/202347345](https://doi.org/10.1051/0004-6361/202347345)

- Gauza, B., Béjar, V. J. S., Pérez-Garrido, A., et al. 2015, *ApJ*, 804, 96, doi: [10.1088/0004-637X/804/2/96](https://doi.org/10.1088/0004-637X/804/2/96)
- Gizis, J. E. 2002, *ApJ*, 575, 484, doi: [10.1086/341259](https://doi.org/10.1086/341259)
- Gizis, J. E., & Bharat, R. 2004, *ApJL*, 608, L113, doi: [10.1086/422339](https://doi.org/10.1086/422339)
- Gizis, J. E., Jao, W.-C., Subasavage, J. P., & Henry, T. J. 2007, *ApJL*, 669, L45, doi: [10.1086/523271](https://doi.org/10.1086/523271)
- Gizis, J. E., Shipman, H. L., & Harvin, J. A. 2005, *ApJL*, 630, L89, doi: [10.1086/462414](https://doi.org/10.1086/462414)
- Golimowski, D. A., Leggett, S. K., Marley, M. S., et al. 2004, *AJ*, 127, 3516, doi: [10.1086/420709](https://doi.org/10.1086/420709)
- Gonzales, E. C., Burningham, B., Faherty, J. K., et al. 2020, *ApJ*, 905, 46, doi: [10.3847/1538-4357/abee2](https://doi.org/10.3847/1538-4357/abee2)
- . 2021, *ApJ*, 923, 19, doi: [10.3847/1538-4357/ac294e](https://doi.org/10.3847/1538-4357/ac294e)
- González Picos, D., Snellen, I. A. G., de Regt, S., et al. 2024, *A&A*, 689, A212, doi: [10.1051/0004-6361/202450028](https://doi.org/10.1051/0004-6361/202450028)
- GRAVITY Collaboration, Nowak, M., Lacour, S., et al. 2020, *A&A*, 633, A110, doi: [10.1051/0004-6361/201936898](https://doi.org/10.1051/0004-6361/201936898)
- Gully-Santiago, M. A., Herczeg, G. J., Czekala, I., et al. 2017, *ApJ*, 836, 200, doi: [10.3847/1538-4357/836/2/200](https://doi.org/10.3847/1538-4357/836/2/200)
- Hammel, H. B., Beebe, R. F., Ingersoll, A. P., et al. 1995, *Science*, 267, 1288, doi: [10.1126/science.7871425](https://doi.org/10.1126/science.7871425)
- Hargreaves, R. J., Gordon, I. E., Rey, M., et al. 2020, *ApJS*, 247, 55, doi: [10.3847/1538-4365/ab7a1a](https://doi.org/10.3847/1538-4365/ab7a1a)
- Harvey, P. M., Henning, T., Ménard, F., et al. 2012, *ApJL*, 744, L1, doi: [10.1088/2041-8205/744/1/L1](https://doi.org/10.1088/2041-8205/744/1/L1)
- Hawkins, K., Lucey, M., Ting, Y.-S., et al. 2020, *MNRAS*, 492, 1164, doi: [10.1093/mnras/stz3132](https://doi.org/10.1093/mnras/stz3132)
- Helled, R., & Bodenheimer, P. 2010, *Icarus*, 207, 503, doi: [10.1016/j.icarus.2009.11.023](https://doi.org/10.1016/j.icarus.2009.11.023)
- Helled, R., Podolak, M., & Kovetz, A. 2006, *Icarus*, 185, 64, doi: [10.1016/j.icarus.2006.06.011](https://doi.org/10.1016/j.icarus.2006.06.011)
- Helled, R., & Schubert, G. 2009, *ApJ*, 697, 1256, doi: [10.1088/0004-637X/697/2/1256](https://doi.org/10.1088/0004-637X/697/2/1256)
- Herczeg, G. J., Cruz, K. L., & Hillenbrand, L. A. 2009, *ApJ*, 696, 1589, doi: [10.1088/0004-637X/696/2/1589](https://doi.org/10.1088/0004-637X/696/2/1589)
- Hinkley, S., Lacour, S., Marleau, G. D., et al. 2023, *A&A*, 671, L5, doi: [10.1051/0004-6361/202244727](https://doi.org/10.1051/0004-6361/202244727)
- Hoch, K. K. W., Konopacky, Q. M., Theissen, C. A., et al. 2023, *AJ*, 166, 85, doi: [10.3847/1538-3881/ace442](https://doi.org/10.3847/1538-3881/ace442)
- Hockey, T. 1999, Galileo's planet : observing Jupiter before photography
- Hsu, C.-C., Wang, J. J., Xuan, J. W., et al. 2024a, *ApJ*, 971, 9, doi: [10.3847/1538-4357/ad58d3](https://doi.org/10.3847/1538-4357/ad58d3)
- . 2024b, arXiv e-prints, arXiv:2405.08312, doi: [10.48550/arXiv.2405.08312](https://doi.org/10.48550/arXiv.2405.08312)
- Hunter, J. D. 2007, *Computing in Science & Engineering*, 9, 90, doi: [10.1109/MCSE.2007.55](https://doi.org/10.1109/MCSE.2007.55)
- Hurt, S. A., Liu, M. C., Zhang, Z., et al. 2024, *ApJ*, 961, 121, doi: [10.3847/1538-4357/ad0b12](https://doi.org/10.3847/1538-4357/ad0b12)
- Inglis, J., Wallack, N. L., Xuan, J. W., et al. 2024, *AJ*, 167, 218, doi: [10.3847/1538-3881/ad2771](https://doi.org/10.3847/1538-3881/ad2771)
- Irwin, P. G. J., Hill, S. M., Fletcher, L. N., Alexander, C., & Rogers, J. H. 2025, *Journal of Geophysical Research (Planets)*, 130, 2024JE008622, doi: [10.1029/2024JE008622](https://doi.org/10.1029/2024JE008622)
- Iyer, A. R., Line, M. R., Muirhead, P. S., Fortney, J. J., & Gharib-Nezhad, E. 2023, *ApJ*, 944, 41, doi: [10.3847/1538-4357/acabc2](https://doi.org/10.3847/1538-4357/acabc2)
- Jäger, C., Il'in, V. B., Henning, T., et al. 2003, *JQSRT*, 79-80, 765, doi: [10.1016/S0022-4073\(02\)00301-1](https://doi.org/10.1016/S0022-4073(02)00301-1)
- Jakobsen, P., Ferruit, P., Alves de Oliveira, C., et al. 2022, *A&A*, 661, A80, doi: [10.1051/0004-6361/202142663](https://doi.org/10.1051/0004-6361/202142663)
- Jayawardhana, R., Ardila, D. R., Stelzer, B., & Haisch, Karl E., J. 2003, *AJ*, 126, 1515, doi: [10.1086/377144](https://doi.org/10.1086/377144)
- Jones, E., Oliphant, T., Peterson, P., et al. 2001, *SciPy: Open source scientific tools for Python*. <http://www.scipy.org/>
- Kammerer, J., Lacour, S., Stolker, T., et al. 2021, *A&A*, 652, A57, doi: [10.1051/0004-6361/202140749](https://doi.org/10.1051/0004-6361/202140749)
- Kass, R. E., & Raftery, A. E. 1995, *Journal of the American Statistical Association*, 90, 773, doi: [10.1080/01621459.1995.10476572](https://doi.org/10.1080/01621459.1995.10476572)
- Kirkpatrick, J. D., Gelino, C. R., Faherty, J. K., et al. 2021, *ApJS*, 253, 7, doi: [10.3847/1538-4365/abd107](https://doi.org/10.3847/1538-4365/abd107)
- Kothari, H., Cushing, M. C., Burningham, B., et al. 2024, *ApJ*, 971, 121, doi: [10.3847/1538-4357/ad583b](https://doi.org/10.3847/1538-4357/ad583b)
- Landman, R., Stolker, T., Snellen, I. A. G., et al. 2024, *A&A*, 682, A48, doi: [10.1051/0004-6361/202347846](https://doi.org/10.1051/0004-6361/202347846)
- Lee, E. K. H., Tan, X., & Tsai, S.-M. 2023, *MNRAS*, 523, 4477, doi: [10.1093/mnras/stad1715](https://doi.org/10.1093/mnras/stad1715)
- . 2024, *MNRAS*, 529, 2686, doi: [10.1093/mnras/stae537](https://doi.org/10.1093/mnras/stae537)
- Lee, J. M., Fletcher, L. N., & Irwin, P. G. J. 2012, *MNRAS*, 420, 170, doi: [10.1111/j.1365-2966.2011.20013.x](https://doi.org/10.1111/j.1365-2966.2011.20013.x)
- Lee, J.-M., Heng, K., & Irwin, P. G. J. 2013, *ApJ*, 778, 97, doi: [10.1088/0004-637X/778/2/97](https://doi.org/10.1088/0004-637X/778/2/97)
- Leggett, S. K., Allard, F., Geballe, T. R., Hauschildt, P. H., & Schweitzer, A. 2001, *ApJ*, 548, 908, doi: [10.1086/319020](https://doi.org/10.1086/319020)
- Lei, E., & Mollière, P. 2024, arXiv e-prints, arXiv:2410.21364, doi: [10.48550/arXiv.2410.21364](https://doi.org/10.48550/arXiv.2410.21364)
- Lew, B. W. P., Apai, D., Zhou, Y., et al. 2016, *ApJL*, 829, L32, doi: [10.3847/2041-8205/829/2/L32](https://doi.org/10.3847/2041-8205/829/2/L32)
- Lew, B. W. P., Apai, D., Marley, M., et al. 2020, *ApJ*, 903, 15, doi: [10.3847/1538-4357/abb81d](https://doi.org/10.3847/1538-4357/abb81d)
- Lew, B. W. P., Roellig, T., Batalha, N. E., et al. 2024, *AJ*, 167, 237, doi: [10.3847/1538-3881/ad3425](https://doi.org/10.3847/1538-3881/ad3425)
- Liddle, A. R. 2007, *MNRAS*, 377, L74, doi: [10.1111/j.1745-3933.2007.00306.x](https://doi.org/10.1111/j.1745-3933.2007.00306.x)
- Line, M. R., Teske, J., Burningham, B., Fortney, J. J., & Marley, M. S. 2015, *ApJ*, 807, 183, doi: [10.1088/0004-637X/807/2/183](https://doi.org/10.1088/0004-637X/807/2/183)
- Line, M. R., Wolf, A. S., Zhang, X., et al. 2013, *ApJ*, 775, 137, doi: [10.1088/0004-637X/775/2/137](https://doi.org/10.1088/0004-637X/775/2/137)

- Line, M. R., Marley, M. S., Liu, M. C., et al. 2017, *ApJ*, 848, 83, doi: [10.3847/1538-4357/aa7ff0](https://doi.org/10.3847/1538-4357/aa7ff0)
- Lodato, G., Delgado-Donate, E., & Clarke, C. J. 2005, *MNRAS*, 364, L91, doi: [10.1111/j.1745-3933.2005.00112.x](https://doi.org/10.1111/j.1745-3933.2005.00112.x)
- Looper, D. L., Burgasser, A. J., Kirkpatrick, J. D., & Swift, B. J. 2007, *ApJL*, 669, L97, doi: [10.1086/523812](https://doi.org/10.1086/523812)
- Luhman, K. L. 2023, *AJ*, 165, 269, doi: [10.3847/1538-3881/acf19](https://doi.org/10.3847/1538-3881/acf19)
- Luhman, K. L., Patten, B. M., Marengo, M., et al. 2007, *ApJ*, 654, 570, doi: [10.1086/509073](https://doi.org/10.1086/509073)
- Luhman, K. L., Tremblin, P., Birkmann, S. M., et al. 2023, *ApJL*, 949, L36, doi: [10.3847/2041-8213/acd635](https://doi.org/10.3847/2041-8213/acd635)
- MacDonald, R. J., & Batalha, N. E. 2023, *Research Notes of the American Astronomical Society*, 7, 54, doi: [10.3847/2515-5172/acc46a](https://doi.org/10.3847/2515-5172/acc46a)
- Macintosh, B., Graham, J. R., Barman, T., et al. 2015, *Science*, 350, 64, doi: [10.1126/science.aac5891](https://doi.org/10.1126/science.aac5891)
- Madhusudhan, N., Burrows, A., & Currie, T. 2011, *ApJ*, 737, 34, doi: [10.1088/0004-637X/737/1/34](https://doi.org/10.1088/0004-637X/737/1/34)
- Madhusudhan, N., & Seager, S. 2009, *ApJ*, 707, 24, doi: [10.1088/0004-637X/707/1/24](https://doi.org/10.1088/0004-637X/707/1/24)
- Madurowicz, A., Mukherjee, S., Batalha, N., et al. 2023, *AJ*, 165, 238, doi: [10.3847/1538-3881/acca7a](https://doi.org/10.3847/1538-3881/acca7a)
- Malo, L., Doyon, R., Lafrenière, D., et al. 2013, *ApJ*, 762, 88, doi: [10.1088/0004-637X/762/2/88](https://doi.org/10.1088/0004-637X/762/2/88)
- Mamajek, E. E. 2005, *ApJ*, 634, 1385, doi: [10.1086/468181](https://doi.org/10.1086/468181)
- Mamajek, E. E., & Meyer, M. R. 2007, *ApJL*, 668, L175, doi: [10.1086/522957](https://doi.org/10.1086/522957)
- Manjavacas, E., Tremblin, P., Birkmann, S., et al. 2024, *AJ*, 167, 168, doi: [10.3847/1538-3881/ad2938](https://doi.org/10.3847/1538-3881/ad2938)
- Mann, A. W., Gaidos, E., & Ansdell, M. 2013, *ApJ*, 779, 188, doi: [10.1088/0004-637X/779/2/188](https://doi.org/10.1088/0004-637X/779/2/188)
- Marleau, G.-D., Aoyama, Y., Hashimoto, J., & Zhou, Y. 2024, *ApJ*, 964, 70, doi: [10.3847/1538-4357/ad1ee9](https://doi.org/10.3847/1538-4357/ad1ee9)
- Marley, M. S., & Robinson, T. D. 2015, *ARA&A*, 53, 279, doi: [10.1146/annurev-astro-082214-122522](https://doi.org/10.1146/annurev-astro-082214-122522)
- Marley, M. S., Saumon, D., & Goldblatt, C. 2010, *ApJL*, 723, L117, doi: [10.1088/2041-8205/723/1/L117](https://doi.org/10.1088/2041-8205/723/1/L117)
- Marley, M. S., Saumon, D., Visscher, C., et al. 2021, *ApJ*, 920, 85, doi: [10.3847/1538-4357/ac141d](https://doi.org/10.3847/1538-4357/ac141d)
- Marois, C., Macintosh, B., Barman, T., et al. 2008, *Science*, 322, 1348, doi: [10.1126/science.1166585](https://doi.org/10.1126/science.1166585)
- Marois, C., Zuckerman, B., Konopacky, Q. M., Macintosh, B., & Barman, T. 2010, *Nature*, 468, 1080, doi: [10.1038/nature09684](https://doi.org/10.1038/nature09684)
- Martin, R. G., Lubow, S. H., Pringle, J. E., & Wyatt, M. C. 2007, *MNRAS*, 378, 1589, doi: [10.1111/j.1365-2966.2007.11906.x](https://doi.org/10.1111/j.1365-2966.2007.11906.x)
- McCarthy, A. M., Vos, J. M., Muirhead, P. S., et al. 2024, *arXiv e-prints*, arXiv:2411.16577, doi: [10.48550/arXiv.2411.16577](https://doi.org/10.48550/arXiv.2411.16577)
- McKemmish, L. K., Masseron, T., Hoeijmakers, H. J., et al. 2019, *MNRAS*, 488, 2836, doi: [10.1093/mnras/stz1818](https://doi.org/10.1093/mnras/stz1818)
- McKemmish, L. K., Yurchenko, S. N., & Tennyson, J. 2016, *MNRAS*, 463, 771, doi: [10.1093/mnras/stw1969](https://doi.org/10.1093/mnras/stw1969)
- Metchev, S. A., & Hillenbrand, L. A. 2006, *ApJ*, 651, 1166, doi: [10.1086/507836](https://doi.org/10.1086/507836)
- Miles, B. E., Biller, B. A., Patapis, P., et al. 2023, *ApJL*, 946, L6, doi: [10.3847/2041-8213/acb04a](https://doi.org/10.3847/2041-8213/acb04a)
- Miret-Roig, N., Bouy, H., Raymond, S. N., et al. 2022, *Nature Astronomy*, 6, 89, doi: [10.1038/s41550-021-01513-x](https://doi.org/10.1038/s41550-021-01513-x)
- Mohanty, S., Jayawardhana, R., & Barrado y Navascués, D. 2003, *ApJL*, 593, L109, doi: [10.1086/378315](https://doi.org/10.1086/378315)
- Mohanty, S., Jayawardhana, R., & Basri, G. 2005, *ApJ*, 626, 498, doi: [10.1086/429794](https://doi.org/10.1086/429794)
- Mohanty, S., Jayawardhana, R., Huélamo, N., & Mamajek, E. 2007, *ApJ*, 657, 1064, doi: [10.1086/510877](https://doi.org/10.1086/510877)
- Mohanty, S., Greaves, J., Mortlock, D., et al. 2013, *ApJ*, 773, 168, doi: [10.1088/0004-637X/773/2/168](https://doi.org/10.1088/0004-637X/773/2/168)
- Mollière, P., van Boekel, R., Bouwman, J., et al. 2017, *A&A*, 600, A10, doi: [10.1051/0004-6361/201629800](https://doi.org/10.1051/0004-6361/201629800)
- Mollière, P., van Boekel, R., Dullemond, C., Henning, T., & Mordasini, C. 2015, *ApJ*, 813, 47, doi: [10.1088/0004-637X/813/1/47](https://doi.org/10.1088/0004-637X/813/1/47)
- Mollière, P., Wardenier, J. P., van Boekel, R., et al. 2019, *A&A*, 627, A67, doi: [10.1051/0004-6361/201935470](https://doi.org/10.1051/0004-6361/201935470)
- Mollière, P., Stolker, T., Lacour, S., et al. 2020, *A&A*, 640, A131, doi: [10.1051/0004-6361/202038325](https://doi.org/10.1051/0004-6361/202038325)
- Mollière, P., Molyarova, T., Bitsch, B., et al. 2022, *ApJ*, 934, 74, doi: [10.3847/1538-4357/ac6a56](https://doi.org/10.3847/1538-4357/ac6a56)
- Morley, C. V., Marley, M. S., Fortney, J. J., & Lupu, R. 2014, *ApJL*, 789, L14, doi: [10.1088/2041-8205/789/1/L14](https://doi.org/10.1088/2041-8205/789/1/L14)
- Morley, C. V., Mukherjee, S., Marley, M. S., et al. 2024, *ApJ*, 975, 59, doi: [10.3847/1538-4357/ad71d5](https://doi.org/10.3847/1538-4357/ad71d5)
- Morrow, A. L., Luhman, K. L., Espaillat, C., et al. 2008, *ApJL*, 676, L143, doi: [10.1086/587462](https://doi.org/10.1086/587462)
- Mugrauer, M., & Neuhäuser, R. 2005, *Astronomische Nachrichten*, 326, 701, doi: [10.1002/asna.200510410](https://doi.org/10.1002/asna.200510410)
- Mukherjee, S., Fortney, J. J., Morley, C. V., et al. 2024, *ApJ*, 963, 73, doi: [10.3847/1538-4357/ad18c2](https://doi.org/10.3847/1538-4357/ad18c2)
- Nasedkin, E., Mollière, P., & Blain, D. 2024a, *The Journal of Open Source Software*, 9, 5875, doi: [10.21105/joss.05875](https://doi.org/10.21105/joss.05875)
- Nasedkin, E., Mollière, P., Lacour, S., et al. 2024b, *A&A*, 687, A298, doi: [10.1051/0004-6361/202449328](https://doi.org/10.1051/0004-6361/202449328)
- Nelson, T., Ting, Y.-S., Hawkins, K., et al. 2021, *ApJ*, 921, 118, doi: [10.3847/1538-4357/ac14be](https://doi.org/10.3847/1538-4357/ac14be)
- Noll, K. S., Geballe, T. R., Leggett, S. K., & Marley, M. S. 2000, *ApJL*, 541, L75, doi: [10.1086/312906](https://doi.org/10.1086/312906)
- Oliphant, T. 2006, *NumPy: A guide to NumPy*, USA: Trelgol Publishing. <http://www.numpy.org/>
- Orton, G., Ortiz, J. L., Baines, K., et al. 1996, *Science*, 272, 839, doi: [10.1126/science.272.5263.839](https://doi.org/10.1126/science.272.5263.839)

- Osten, R. A., & Jayawardhana, R. 2006, *ApJL*, 644, L67, doi: [10.1086/505328](https://doi.org/10.1086/505328)
- Palma-Bifani, P., Chauvin, G., Borja, D., et al. 2024, *A&A*, 683, A214, doi: [10.1051/0004-6361/202347653](https://doi.org/10.1051/0004-6361/202347653)
- Patience, J., King, R. R., de Rosa, R. J., & Marois, C. 2010, *A&A*, 517, A76, doi: [10.1051/0004-6361/201014173](https://doi.org/10.1051/0004-6361/201014173)
- Patience, J., King, R. R., De Rosa, R. J., et al. 2012, *A&A*, 540, A85, doi: [10.1051/0004-6361/201118058](https://doi.org/10.1051/0004-6361/201118058)
- Pearson, S. G., & McCaughrean, M. J. 2023, arXiv e-prints, arXiv:2310.01231, doi: [10.48550/arXiv.2310.01231](https://doi.org/10.48550/arXiv.2310.01231)
- Pérez, F., & Granger, B. E. 2007, *Computing in Science and Engineering*, 9, 21, doi: [10.1109/MCSE.2007.53](https://doi.org/10.1109/MCSE.2007.53)
- Petrus, S., Whiteford, N., Patapis, P., et al. 2024, *ApJL*, 966, L11, doi: [10.3847/2041-8213/ad3e7c](https://doi.org/10.3847/2041-8213/ad3e7c)
- Phillips, C. L., Faherty, J. K., Burningham, B., et al. 2024, *ApJ*, 972, 172, doi: [10.3847/1538-4357/ad5d57](https://doi.org/10.3847/1538-4357/ad5d57)
- Phillips, M. W., Tremblin, P., Baraffe, I., et al. 2020, *A&A*, 637, A38, doi: [10.1051/0004-6361/201937381](https://doi.org/10.1051/0004-6361/201937381)
- Pirraglia, J. A., Conrath, B. J., Allison, M. D., & Gierasch, P. J. 1981, *Nature*, 292, 677, doi: [10.1038/292677a0](https://doi.org/10.1038/292677a0)
- Planck Collaboration, Ade, P. A. R., Aghanim, N., et al. 2014, *A&A*, 571, A22, doi: [10.1051/0004-6361/201321569](https://doi.org/10.1051/0004-6361/201321569)
- Pollack, J. B., Hollenbach, D., Beckwith, S., et al. 1994, *ApJ*, 421, 615, doi: [10.1086/173677](https://doi.org/10.1086/173677)
- Polyansky, O. L., Kyuberis, A. A., Zobov, N. F., et al. 2018, *MNRAS*, 480, 2597, doi: [10.1093/mnras/sty1877](https://doi.org/10.1093/mnras/sty1877)
- Prinn, R. G., & Barshay, S. S. 1977, *Science*, 198, 1031, doi: [10.1126/science.198.4321.1031](https://doi.org/10.1126/science.198.4321.1031)
- Radigan, J., Lafrenière, D., Jayawardhana, R., & Artigau, E. 2014, *ApJ*, 793, 75, doi: [10.1088/0004-637X/793/2/75](https://doi.org/10.1088/0004-637X/793/2/75)
- Rayner, J. T., Toomey, D. W., Onaka, P. M., et al. 2003, *PASP*, 115, 362, doi: [10.1086/367745](https://doi.org/10.1086/367745)
- Reiners, A., Basri, G., & Christensen, U. R. 2009, *ApJ*, 697, 373, doi: [10.1088/0004-637X/697/1/373](https://doi.org/10.1088/0004-637X/697/1/373)
- Riaz, B., & Gizis, J. E. 2007, *ApJ*, 661, 354, doi: [10.1086/516565](https://doi.org/10.1086/516565)
- . 2008, *ApJ*, 681, 1584, doi: [10.1086/587547](https://doi.org/10.1086/587547)
- . 2012, *A&A*, 548, A54, doi: [10.1051/0004-6361/201219524](https://doi.org/10.1051/0004-6361/201219524)
- Riaz, B., Gizis, J. E., & Hmiel, A. 2006, *ApJL*, 639, L79, doi: [10.1086/502647](https://doi.org/10.1086/502647)
- Riaz, B., Lodato, G., Stamatellos, D., & Gizis, J. E. 2012a, *MNRAS*, 422, L6, doi: [10.1111/j.1745-3933.2012.01225.x](https://doi.org/10.1111/j.1745-3933.2012.01225.x)
- . 2012b, *MNRAS*, 424, L74, doi: [10.1111/j.1745-3933.2012.01278.x](https://doi.org/10.1111/j.1745-3933.2012.01278.x)
- Ricci, L., Cazzoletti, P., Czekala, I., et al. 2017, *AJ*, 154, 24, doi: [10.3847/1538-3881/aa78a0](https://doi.org/10.3847/1538-3881/aa78a0)
- Richard, C., Gordon, I. E., Rothman, L. S., et al. 2012, *JQSRT*, 113, 1276, doi: [10.1016/j.jqsrt.2011.11.004](https://doi.org/10.1016/j.jqsrt.2011.11.004)
- Rieke, G. H., Wright, G. S., Böker, T., et al. 2015, *PASP*, 127, 584, doi: [10.1086/682252](https://doi.org/10.1086/682252)
- Robinson, T. D., & Marley, M. S. 2014, *ApJ*, 785, 158, doi: [10.1088/0004-637X/785/2/158](https://doi.org/10.1088/0004-637X/785/2/158)
- Rothman, L. S., Gordon, I. E., Barber, R. J., et al. 2010, *JQSRT*, 111, 2139, doi: [10.1016/j.jqsrt.2010.05.001](https://doi.org/10.1016/j.jqsrt.2010.05.001)
- Rowland, M. J., Morley, C. V., Miles, B. E., et al. 2024, arXiv e-prints, arXiv:2411.14541, doi: [10.48550/arXiv.2411.14541](https://doi.org/10.48550/arXiv.2411.14541)
- Sanghi, A., Liu, M. C., Best, W. M. J., et al. 2023, *ApJ*, 959, 63, doi: [10.3847/1538-4357/acff66](https://doi.org/10.3847/1538-4357/acff66)
- Santos, N. C., Melo, C., James, D. J., et al. 2008, *A&A*, 480, 889, doi: [10.1051/0004-6361:20079083](https://doi.org/10.1051/0004-6361:20079083)
- Saumon, D., Hubbard, W. B., Burrows, A., et al. 1996, *ApJ*, 460, 993, doi: [10.1086/177027](https://doi.org/10.1086/177027)
- Saumon, D., & Marley, M. S. 2008, *ApJ*, 689, 1327, doi: [10.1086/592734](https://doi.org/10.1086/592734)
- Schneider, A. D., & Bitsch, B. 2021, *A&A*, 654, A71, doi: [10.1051/0004-6361/202039640](https://doi.org/10.1051/0004-6361/202039640)
- Scholz, A., & Jayawardhana, R. 2006, *ApJ*, 638, 1056, doi: [10.1086/498973](https://doi.org/10.1086/498973)
- Scholz, A., Jayawardhana, R., & Brandeker, A. 2005, *ApJL*, 629, L41, doi: [10.1086/444358](https://doi.org/10.1086/444358)
- Schwarz, G. 1978, *Annals of Statistics*, 6, 461
- Showman, A. P., Tan, X., & Zhang, X. 2019, *ApJ*, 883, 4, doi: [10.3847/1538-4357/ab384a](https://doi.org/10.3847/1538-4357/ab384a)
- Simcoe, R. A., Burgasser, A. J., Schechter, P. L., et al. 2013, *PASP*, 125, 270, doi: [10.1086/670241](https://doi.org/10.1086/670241)
- Skemer, A. J., Close, L. M., Szűcs, L., et al. 2011, *ApJ*, 732, 107, doi: [10.1088/0004-637X/732/2/107](https://doi.org/10.1088/0004-637X/732/2/107)
- Skemer, A. J., Marley, M. S., Hinz, P. M., et al. 2014, *ApJ*, 792, 17, doi: [10.1088/0004-637X/792/1/17](https://doi.org/10.1088/0004-637X/792/1/17)
- Song, I., Schneider, G., Zuckerman, B., et al. 2006, *ApJ*, 652, 724, doi: [10.1086/507831](https://doi.org/10.1086/507831)
- Sousa-Silva, C., Al-Refaie, A. F., Tennyson, J., & Yurchenko, S. N. 2015, *MNRAS*, 446, 2337, doi: [10.1093/mnras/stu2246](https://doi.org/10.1093/mnras/stu2246)
- Spiegel, D. S., & Burrows, A. 2012, *ApJ*, 745, 174, doi: [10.1088/0004-637X/745/2/174](https://doi.org/10.1088/0004-637X/745/2/174)
- Stamatellos, D., & Whitworth, A. P. 2009, *MNRAS*, 392, 413, doi: [10.1111/j.1365-2966.2008.14069.x](https://doi.org/10.1111/j.1365-2966.2008.14069.x)
- Stelzer, B., Scholz, A., & Jayawardhana, R. 2007, *ApJ*, 671, 842, doi: [10.1086/521431](https://doi.org/10.1086/521431)
- Sterzik, M. F., Pascucci, I., Apai, D., van der Blik, N., & Dullemond, C. P. 2004, *A&A*, 427, 245, doi: [10.1051/0004-6361:20041502](https://doi.org/10.1051/0004-6361:20041502)
- Tan, X., & Showman, A. P. 2019, *ApJ*, 874, 111, doi: [10.3847/1538-4357/ab0c07](https://doi.org/10.3847/1538-4357/ab0c07)
- . 2021, *MNRAS*, 502, 2198, doi: [10.1093/mnras/stab097](https://doi.org/10.1093/mnras/stab097)
- Teske, J. K. 2024, *ARA&A*, 62, 333, doi: [10.1146/annurev-astro-071221-053007](https://doi.org/10.1146/annurev-astro-071221-053007)
- Thorngren, D., & Fortney, J. J. 2019, *ApJL*, 874, L31, doi: [10.3847/2041-8213/ab1137](https://doi.org/10.3847/2041-8213/ab1137)

- Tremblin, P., Amundsen, D. S., Chabrier, G., et al. 2016, *ApJL*, 817, L19, doi: [10.3847/2041-8205/817/2/L19](https://doi.org/10.3847/2041-8205/817/2/L19)
- Tremblin, P., Amundsen, D. S., Mourier, P., et al. 2015, *ApJL*, 804, L17, doi: [10.1088/2041-8205/804/1/L17](https://doi.org/10.1088/2041-8205/804/1/L17)
- Tremblin, P., Phillips, M. W., Emery, A., et al. 2020, *A&A*, 643, A23, doi: [10.1051/0004-6361/202038771](https://doi.org/10.1051/0004-6361/202038771)
- Tremblin, P., Chabrier, G., Baraffe, I., et al. 2017, *ApJ*, 850, 46, doi: [10.3847/1538-4357/aa9214](https://doi.org/10.3847/1538-4357/aa9214)
- Tremblin, P., Padiou, T., Phillips, M. W., et al. 2019, *ApJ*, 876, 144, doi: [10.3847/1538-4357/ab05db](https://doi.org/10.3847/1538-4357/ab05db)
- Trotta, R., Feroz, F., Hobson, M., Roszkowski, L., & Ruiz de Austri, R. 2008, *Journal of High Energy Physics*, 2008, 024, doi: [10.1088/1126-6708/2008/12/024](https://doi.org/10.1088/1126-6708/2008/12/024)
- Venuti, L., Stelzer, B., Alcalá, J. M., et al. 2019, *A&A*, 632, A46, doi: [10.1051/0004-6361/201935745](https://doi.org/10.1051/0004-6361/201935745)
- Vernet, J., Dekker, H., D'Odorico, S., et al. 2011, *A&A*, 536, A105, doi: [10.1051/0004-6361/201117752](https://doi.org/10.1051/0004-6361/201117752)
- Viana Almeida, P., Santos, N. C., Melo, C., et al. 2009, *A&A*, 501, 965, doi: [10.1051/0004-6361/200811194](https://doi.org/10.1051/0004-6361/200811194)
- Vos, J. M., Allers, K. N., & Biller, B. A. 2017, *ApJ*, 842, 78, doi: [10.3847/1538-4357/aa73cf](https://doi.org/10.3847/1538-4357/aa73cf)
- Vos, J. M., Faherty, J. K., Gagné, J., et al. 2022, *ApJ*, 924, 68, doi: [10.3847/1538-4357/ac4502](https://doi.org/10.3847/1538-4357/ac4502)
- Vos, J. M., Burningham, B., Faherty, J. K., et al. 2023, *ApJ*, 944, 138, doi: [10.3847/1538-4357/acab58](https://doi.org/10.3847/1538-4357/acab58)
- Wang, J. 2023, *AJ*, 166, 203, doi: [10.3847/1538-3881/acfca0](https://doi.org/10.3847/1538-3881/acfca0)
- Wang, J., Wang, J. J., Ma, B., et al. 2020, *AJ*, 160, 150, doi: [10.3847/1538-3881/ababa7](https://doi.org/10.3847/1538-3881/ababa7)
- Wang, J., Kolecki, J. R., Ruffio, J.-B., et al. 2022, *AJ*, 163, 189, doi: [10.3847/1538-3881/ac56e2](https://doi.org/10.3847/1538-3881/ac56e2)
- Wang, J. J., Ruffio, J.-B., Morris, E., et al. 2021, *AJ*, 162, 148, doi: [10.3847/1538-3881/ac1349](https://doi.org/10.3847/1538-3881/ac1349)
- Ward-Duong, K., Patience, J., Follette, K., et al. 2021, *AJ*, 161, 5, doi: [10.3847/1538-3881/abc263](https://doi.org/10.3847/1538-3881/abc263)
- Welbanks, L., Madhusudhan, N., Allard, N. F., et al. 2019, *ApJL*, 887, L20, doi: [10.3847/2041-8213/ab5a89](https://doi.org/10.3847/2041-8213/ab5a89)
- Westphal, J. A. 1969, *ApJL*, 157, L63, doi: [10.1086/180386](https://doi.org/10.1086/180386)
- Whelan, E. T., Ray, T. P., Comeron, F., Bacciotti, F., & Kavanagh, P. J. 2012, *ApJ*, 761, 120, doi: [10.1088/0004-637X/761/2/120](https://doi.org/10.1088/0004-637X/761/2/120)
- Whelan, E. T., Ray, T. P., Randich, S., et al. 2007, *ApJL*, 659, L45, doi: [10.1086/516734](https://doi.org/10.1086/516734)
- Wright, G. S., Rieke, G. H., Glasse, A., et al. 2023, *PASP*, 135, 048003, doi: [10.1088/1538-3873/acbe66](https://doi.org/10.1088/1538-3873/acbe66)
- Xuan, J. W., Wang, J., Ruffio, J.-B., et al. 2022, *ApJ*, 937, 54, doi: [10.3847/1538-4357/ac8673](https://doi.org/10.3847/1538-4357/ac8673)
- Xuan, J. W., Hsu, C.-C., Finnerty, L., et al. 2024, *ApJ*, 970, 71, doi: [10.3847/1538-4357/ad4796](https://doi.org/10.3847/1538-4357/ad4796)
- Yang, H., Apai, D., Marley, M. S., et al. 2016, *ApJ*, 826, 8, doi: [10.3847/0004-637X/826/1/8](https://doi.org/10.3847/0004-637X/826/1/8)
- Yurchenko, S. N., Mellor, T. M., Freedman, R. S., & Tennyson, J. 2020, *MNRAS*, 496, 5282, doi: [10.1093/mnras/staa1874](https://doi.org/10.1093/mnras/staa1874)
- Zahnle, K. J., & Marley, M. S. 2014, *ApJ*, 797, 41, doi: [10.1088/0004-637X/797/1/41](https://doi.org/10.1088/0004-637X/797/1/41)
- Zalesky, J. A., Line, M. R., Schneider, A. C., & Patience, J. 2019, *ApJ*, 877, 24, doi: [10.3847/1538-4357/ab16db](https://doi.org/10.3847/1538-4357/ab16db)
- Zalesky, J. A., Saboi, K., Line, M. R., et al. 2022, *ApJ*, 936, 44, doi: [10.3847/1538-4357/ac786c](https://doi.org/10.3847/1538-4357/ac786c)
- Zhang, X. 2020, *Research in Astronomy and Astrophysics*, 20, 099, doi: [10.1088/1674-4527/20/7/99](https://doi.org/10.1088/1674-4527/20/7/99)
- Zhang, X., & Showman, A. P. 2014, *ApJL*, 788, L6, doi: [10.1088/2041-8205/788/1/L6](https://doi.org/10.1088/2041-8205/788/1/L6)
- Zhang, Y., Snellen, I. A. G., Bohn, A. J., et al. 2021a, *Nature*, 595, 370, doi: [10.1038/s41586-021-03616-x](https://doi.org/10.1038/s41586-021-03616-x)
- Zhang, Z., Liu, M. C., Claytor, Z. R., et al. 2021b, *ApJL*, 916, L11, doi: [10.3847/2041-8213/ac1123](https://doi.org/10.3847/2041-8213/ac1123)
- Zhang, Z., Liu, M. C., Marley, M. S., Line, M. R., & Best, W. M. J. 2021c, *ApJ*, 916, 53, doi: [10.3847/1538-4357/abf8b2](https://doi.org/10.3847/1538-4357/abf8b2)
- , 2021d, *ApJ*, 921, 95, doi: [10.3847/1538-4357/ac0af7](https://doi.org/10.3847/1538-4357/ac0af7)
- Zhang, Z., Liu, M. C., Morley, C. V., et al. 2022, *ApJ*, 935, 15, doi: [10.3847/1538-4357/ac7ce9](https://doi.org/10.3847/1538-4357/ac7ce9)
- Zhang, Z., Liu, M. C., Hermes, J. J., et al. 2020, *ApJ*, 891, 171, doi: [10.3847/1538-4357/ab765c](https://doi.org/10.3847/1538-4357/ab765c)
- Zhang, Z., Mollière, P., Hawkins, K., et al. 2023, *AJ*, 166, 198, doi: [10.3847/1538-3881/acf768](https://doi.org/10.3847/1538-3881/acf768)
- Zhang, Z., Mukherjee, S., Liu, M. C., et al. 2025, *AJ*, 169, 9, doi: [10.3847/1538-3881/ad8b2d](https://doi.org/10.3847/1538-3881/ad8b2d)
- Zhou, Y., Apai, D., Schneider, G. H., Marley, M. S., & Showman, A. P. 2016, *ApJ*, 818, 176, doi: [10.3847/0004-637X/818/2/176](https://doi.org/10.3847/0004-637X/818/2/176)
- Zhou, Y., Bowler, B. P., Apai, D., et al. 2022, *AJ*, 164, 239, doi: [10.3847/1538-3881/ac9905](https://doi.org/10.3847/1538-3881/ac9905)
- Zhou, Y., Apai, D., Lew, B. W. P., et al. 2019, *AJ*, 157, 128, doi: [10.3847/1538-3881/ab037f](https://doi.org/10.3847/1538-3881/ab037f)
- Zuckerman, B., & Song, I. 2009, *A&A*, 493, 1149, doi: [10.1051/0004-6361:200810038](https://doi.org/10.1051/0004-6361:200810038)